



Escola de Camins

Escola Tècnica Superior d'Enginyeria de Camins, Canals i Ports
UPC BARCELONATECH

TESI DE MÀSTER

Màster

Màster en Enginyeria de Camins, Canals i Ports

Títol

Virtual wind tunnel experiments using embedded
fluid-structure interaction framework.

Autor/a

ANTONIO GARCÍA LUQUE

Tutor/a

EUGENIO OÑATE

PAVEL RYZHAKOV

Departament

RMEE – Departament de Resistència de Materials i Estructures a
l'Enginyeria

CIMNE – International Center for Numerical Methods in Engineering

Intensificació

Enginyeria Computacional

Data

JULIOL 2015

VIRTUAL WIND TUNNEL EXPERIMENTS USING EMBEDDED FLUID-STRUCTURE INTERACTION FRAMEWORK

MASTER OF SCIENCE THESIS

In partial fulfilment for the degree of Master of Science in Civil Engineering
(Ingeniería de Caminos, Canales y Puertos) at
Universitat Politècnica de Catalunya

ANTONIO GARCÍA LUQUE

Advisors: E. Oñate (UPC)

P. Ryzhakov (CIMNE)

Barcelona, June 2015

Escola Tècnica Superior d'Enginyeria de Camins Canals i Ports de Barcelona. UPC

Abstract

Thin light-weight structures, such as inflatable aircraft hangars and temporary shelters, are becoming increasingly important nowadays. This type of structures can be affected by high wind pressures; also large displacements in the structure are produced. Conventional methods for studying inflatable structures do not take into account the interaction between the fluid and structure. Typically, purely computational structural dynamic simulations are performed assuming an approximate air pressure distribution. Due to the oversimplifications used in the conventional methods, the need for developing new robust and feasible approaches arises. In particular, the effects of unsteady flow cannot be represented without taking fluid-structure interaction in account.

Body-fitted mesh methods, such as Arbitrary Lagrangian-Eulerian (ALE) approach have an important reputation for simulating fluid-structures interaction problems with moving and deforming structures. However, due to the large displacements produced in the light-weight structures, strong mesh distortion occurs, making ALE approach unfeasible for the problem of interest.

The robustness of the non-body-fitted mesh approach and the nature of the problem at hand, referring to the interdependence between the structural deformation and the surrounding flow, inflatable structures call for a strong two-way coupling solution.

A strong two-way coupling algorithm using embedded framework for the solution of light-weight structures (developed at the International Center for Numerical Methods in Engineering –CIMNE- by Kratos Group), is presented in the present work.

The thesis focuses on the verification of the proposed solution strategy and the posterior application in a real case. First attempt to analyze a thin light-weight structure using a strong two-way coupling simulation is carried out in this thesis. Several algorithms of improvements for increasing the robustness of the coupling are proposed. Also, comparisons with conventional methods are discussed.

Acknowledgements

First, I would like to express my sincere gratitude to Prof. Eugenio Oñate for giving me the opportunity to take part in this challenging research project within CIMNE (International Center for Numerical Methods in Engineering).

I offer my deepest gratitude to Dr. Pavel Ryzhakov, my co-supervisor, for his constantly support, guidance and patient during this study. Thank you so much Dr. Pavel, I really appreciate your help and all I have learned during my Master's Thesis.

I am also indebted to the staff of CIMNE, especially to Jordi Cotella and Miguel Angel Celigueta for their assistance and being always keen to help me with different issues during the thesis. Also I would like to thanks the personal of GiD for their assistance in problems related to GiD.

Especially, I would like to warmly thank my girlfriend Mireia, for her unconditionally support and patient and to my family; all of them have been the ones who have held my mood swings not only during my thesis, but during all my university life.

Finally but not least, I appreciate the great moments spent with my colleges during the Master and the degree. I finish an important stage of my life where I have lived wonderful moments and met great people.

Contents

Abstract	i
Acknowledgements	ii
Contents	iii
List of Figures	vi
List of Tables	ix
Chapter 1: Introduction	1
1.1 Wind tunnel testing.....	1
1.2 Computational Fluid Dynamics.....	3
1.2.1 Computational Fluid Dynamics for wind tunnel simulations.....	4
1.3 Inflatable structures.....	6
1.3.1 Brief introduction to its history.....	6
1.3.2 Structural behaviour of inflatable structures	8
1.4 State-of-the-art in the computational modelling of inflatable structures	8
References.....	10
Chapter 2: Fluid Structure Interaction	11
2.1 Brief introduction to Fluid-structure interaction	11
2.2 Problem formulation.....	12
2.2.1 Governing equations of fluid mechanics.....	14
2.2.2 Governing equations of structural mechanics	18
2.2.3 Interface conditions.....	19
2.3 Body fitted and non-body fitted meshes	20
2.3.1 Body-fitted mesh.....	21

2.3.2	Non body-fitted mesh (NBF)	22
2.4	Fluid-structure coupling	23
	References	25
Chapter 3:	Two-way FSI coupling algorithm.....	27
3.1	Overall embedded solution	27
3.2	Model for the fluid	30
3.2.1	Spatial discretization.....	31
3.2.2	Time discretization	34
3.3	Model for the structure	34
3.3.1	Membrane element.....	35
3.3.2	Spatial discretization.....	38
3.3.3	Time discretization	42
3.4	Coupling scheme	44
3.4.1	Boundary conditions	44
3.5	Solution Algorithm.....	46
	References	47
Chapter 4:	Implementation Issues	48
4.1	Overall solution strategy	49
4.1.1	Optimal time duration of preliminary stages.....	51
4.1.2	Incremental pressure application.....	53
4.2	Final comments.....	54
Chapter 5:	Wind Tunnel Simulation.....	56
5.1	Model.....	56
5.1.1	Structural model.....	57
5.1.2	Fluid model.....	60
5.2	Wind action loads due to EN 1991-1-4: 2005 simplifications.....	64

5.2.1	Variable actions due to wind.....	64
5.2.2	Results	67
5.3	Simplified CFD.....	68
5.3.1	Results	68
5.4	Strong two-way coupling simulation	71
5.4.1	Results	71
5.5	Summary and comparison of the results	79
5.5.1	Two-way coupling VS Simplified CFD	79
5.5.2	Two-way coupling VS EN 1991-1-4:2005	80
5.6	Engineering observations	80
5.6.1	Stiffening straps	81
5.6.2	Internal pressure	84
	Summary and Conclusions.....	86
	Future works	87
	Cited Authors.....	89
	Annex I: Python Scripts.....	93
	Structural project parameters	94
	Fluid project parameters.....	96
	Two-way coupling algorithm	98
	Annex II: Tutorial.....	114

List of Figures

Figure 1.1. Classification of Wind Tunnel on basis of its Geometry as (a) CCWT and (b) OCWT.....	3
Figure 1.2. Fuji pavilion, 1970, Osaka.....	7
Figure 1.3. Inflatable airplane hangar, BuildAir.....	7
Figure 1.4. Air bridge prototype designed by BuildAir.....	8
Figure 2.1. FSI categories	12
Figure 2.2. Representation of a solid body \mathbf{B} immersed in a domain Ω_t^f , with the respective boundary, $\partial\mathbf{B}$ and $\partial\Omega$	14
Figure 2.3. Matching interface conditions for a fluid-structure interaction	20
Figure 2.4. Representation of a Body-fitted mesh (a), and a Non Body-fitted mesh (b).....	22
Figure 2.5. Interface elements. Solid cells: elements inside the black polyline. Boundary cells: elements represented in colour grey. Flow cells: elements outside black polyline and belonging to the fluid domain Ω^f	23
Figure 2.6. Two different approach for interaction between subdomains: (a) One-way coupling (b) two-way coupling.....	24
Figure 3.1. Embedded approach: movement of the Lagrangian domain and its image within the Eulerian mesh from time step tn to $tn + 1$	28
Figure 3.2. Embedded setting: real, fictitious and interface parts of the Eulerian domain ..	29
Figure 3.3. Interpolation technique for Neumann boundary conditions coupling	45
Figure 4.1. Structural dynamic response due to self-weight and constant internal pressure	49
Figure 4.2. Structural velocity response due to an inlet fluid velocity of 35m/s	50
Figure 4.3. Application of the incremental pressure technique for an inlet velocity of 10m/s	54
Figure 4.4. Overall graphic example of the different steps taking part in the algorithm solution.....	55
Figure 5.1. Geometry of the inflatable H20 hangar- (a) front elevation (b) lateral elevation (c) three-dimensional view	57

Figure 5.2. Representation of the load case	59
Figure 5.3. Convergence analysis for the structural mesh	60
Figure 5.4. Dimension relations for a wind tunnel size	61
Figure 5.5. Flow analysis of the distance downstream of the structure.....	61
Figure 5.6. Wind tunnel dimensions.....	62
Figure 5.7. Refined distance around the Lagrangian image	63
Figure 5.8. Wind tunnel mesh and size of the box.....	63
Figure 5.9. Geometric parameters and pressure distribution over cylindrical roof and domes	64
Figure 5.10. Abacus for external pressure coefficient	65
Figure 5.11. Air pressure values and areas of application.	66
Figure 5.12. Displacements obtained in the simplified method according to Eurocode 1....	67
Figure 5.13. Pressure field obtained in a CFD simulation with an inlet velocity of 35m/s..	68
Figure 5.14. Pressure distribution obtained in the CFD simulation.....	68
Figure 5.15. Time-pressure graph applied in a CSD for different inlet velocities.....	69
Figure 5.16. Displacements obtained in a CSD after application of air pressure distribution.	70
Figure 5.17. Displacement evolution due to a constant air pressure.	70
Figure 5.18. (a) Displacement on the static solution of the structure (b) Displacement produced by an inlet velocity of 10m/s (c) Displacements due to a velocity of 20 m/s (d) Displacements due to an inlet velocity of 35 m/s	72
Figure 5.19. Deformed shape of the structure due to an inlet velocity of 20m/s.....	72
Figure 5.20. Graphic representation on time of the displacements produced by different inlet velocities	73
Figure 5.21. Zoom in the two-way coupling process of Figure 5.20.....	73
Figure 5.22. Pressure configuration over the structure at time=19s. (a) v=10m/s (b) v=20 m/s (c) v=35m/s	76
Figure 5.23. Evolution on time of the air pressure applied onto the structure surface	77
Figure 5.24. Pressure solution at the strong two-way coupling stage.....	77
Figure 5.25. Tensile force in a circular element	78
Figure 5.26. Principal maximum stress due to self-weight and internal pressure	79
Figure 5.27. Principal maximum stresses due to self-weight, internal pressure and the air pressure.....	79

Figure 5.28. Stiffened structure with straps in longitudinal and transversal direction	81
Figure 5.29. Displacements and Principal Stresses due to self-weight and internal pressure	82
Figure 5.30. Displacements and Principal Stresses at time of the two-way coupling process	82
Figure 5.31. Stiffened and original structure time-displacement evolution at the two-way coupling stage	83
Figure 5.32. Displacements due to 1000Pa internal pressure (a) S-W and internal pressure (b) S-W, internal pressure and air pressure due to inlet velocity of 35m/s.....	84
Figure 5.33. Displacements due to 2000Pa internal pressure (a) S-W and internal pressure (b) S-W, internal pressure and air pressure due to inlet velocity of 35m/s.....	84
Figure 5.34 Displacements due to 3000Pa internal pressure (a) S-W and internal pressure (b) S-W, internal pressure and air pressure due to inlet velocity of 35m/s.....	84

List of Tables

Table 1-1. Estimated cost for Wind Tunnel and CFD.....	5
Table 3-1. Index map for Q array	40
Table 3-2. Solution algorithm of the coupled fluid-structure problem.....	46
Table 4-1. Scheme of the overall solution strategy in the solution of a two-way coupling interaction.....	48
Table 4-2. Pseudo-code of the implementation in the algorithm for the uncoupled time solution identification.....	52
Table 4-3. Pseudo-code of the implementation in the algorithm for the one-way coupling time identification	52
Table 4-4. Pseudo-code of the implementation of the algorithm for the incremental pressure technique.....	53
Table 5-1. Dimensions of H20 inflatable hangar	57
Table 5-2. PLASTEL 8820 properties	58
Table 5-3. Load case	58
Table 5-4. Data of different meshes for convergence analysis	59
Table 5-5. Fluid properties.....	60
Table 5-6. Data resulting from the flow analysis	61
Table 5-7. Wind tunnel dimensions.....	62
Table 5-8. Parametric properties of wind tunnel domain.....	63
Table 5-9. Geometrical parameters.....	65
Table 5-10. Parameters for wind loads calculation	66
Table 5-11. Summary of values according to EN 1991-1-4:2005 ($v_d=35\text{m/s}$)	67
Table 5-12. Analytical pressure solutions	69
Table 5-13. Summary of values according to a simplified CFD analysis	70
Table 5-14. Significant displacements and Reynolds number for different velocities	74
Table 5-15. Fluid results over time steps for an inlet velocity of 20m/s	74
Table 5-16. Significant pressures and amplitude of the pressure spectrum.....	77
Table 5-17. Summary of the results for two-way coupling and Simplified CFD solutions ...	79

Table 5-18. Summary of the results for two-way coupling and EN 1991-1-4:2005 solutions	80
Table 5-19. PLASTEL 8820 and straps properties	81
Table 5-20. Summary displacement for original and stiffened model	83
Table 5-21. Displacement comparison due to different internal pressure (cm).....	85

Chapter 1:

Introduction

1.1 Wind tunnel testing

The wind tunnel, in the context of aerodynamics, is a scaled experimental testing, or in a few cases in a real scale-one, used to assess the effects of a fluid moving past a solid object. The wind tunnels were developed towards the end of the 19th century, in the early days of the aeronautic research, with the aim to develop successful heavier-than-air flying machines and study the effects of the air into an aircraft, such as lift and drag. The success of the wind tunnel was possible due to contemplating the reversing of the usual paradigm, where it was envisioned that the same effect would be obtained if the object stood still and the air moved at speed past it, instead of the air standing still and an object moving at speed through it. In that way, it could be possible to study the flying object in action and measure the aerodynamic forces subjected on it by a stationary observer.

The quest to measure lift, drag and various aspects of aviation theory does not come from the wind tunnel testing. It originates from the very first advances in aviation, when Benjamin Robins (1707-1751), an English mathematician, developed the whirling arm apparatus. It spun by a falling weight acting on a pulley and spindle, ranging low speeds (from 3 to 6 m/s).

However, the whirling arm did not produce reliable results, it was difficult to measure the small forces exerted on the model when it was spinning at high speeds owing to centrifugal forces and the fact that the object is moving in its own wake. Furthermore, experiments, such as determination of the true relative velocities between the model and air were serious problems due to the large amount of turbulence. The first enclosed wind tunnel was designed in 1871, when Francis Herbert Wenham (1824-1908), a council of the Aeronautical

Society of Great Britain, addressed the issue by inventing, designing and operating the testing apparatus. This great achievement was rapidly extended, and after some of the experimental studies, it was discovered that wings could support substantial loads, making powered flight which seemed much more attainable than previously thought possible, owing to lift-to-drag ratios were very high.

In a classic set of experiments, the professor Osborne Reynolds (1842-1912) of the University of Manchester demonstrated that the airflow pattern over the full-scale object could be studied in a scale model if a certain flow parameter, now known as the Reynolds number (Re), were the same in both cases. The Re comprises the central scientific justification for the use of models in wind tunnels to simulate real-life phenomena, and is a basic parameter for describing all fluid-flow situations, such as turbulence or the ease of heat transfer.

However, Reynolds number is not the unique parameter to guarantee similarity between scale models. Satisfactory correspondences between the aerodynamic properties of a scaled model and a full-size object can be achieved by observing certain similarity rules. These similarity o dimensionless parameters vary according to the type of the test, but the most important conditions to satisfy are usually:

- *Geometric similarity*: All dimensions of the object must be proportionally scaled.
- *Mach number (Ma)*: The ratio of the airspeed to the speed of sound should be identical for the scaled model and the actual object.
- *Reynolds number*: The ratio of inertial forces to viscous forces should be kept.

The development of wind tunnel was crucial during the Second World War for the development of the airplane, and large wind tunnels were built. Wind tunnel testing was considered of strategic importance during the Cold War development of supersonic aircraft and missiles. Later on, the use of wind tunnels became a very useful tool for different applications, such as civil engineering to calculate the effects of wind loads in tall buildings, cable suspended bridges or any infrastructure, as well as for the automobile field to determine ways to reduce the power required to move the vehicle on roadways at a given velocity.

Nowadays, wind tunnels are well known and indispensable for its enormous amount of potential in a broad variation of applications. Consequently, there are different types of wind tunnels, and are designed for a specific purpose and speed range. One way to classify wind tunnels is based on the Speed Regime developed in test section relative to the speed of sound (Mach number 'M').

Subsonic WT ($M < 0.8$)

Transonic WT ($0.8 < M < 1.2$)

Supersonic WT ($1.2 < M < 5$)

Hypersonic WT ($M > 5$)

Also, maybe distinguished on the basis of their geometry, where wind tunnels are classified as Closed Circuit Wind Tunnel (CCWT) or Open Circuit Wind Tunnel (OCWT), see Figure 1.1. The CCWT's have a closed circuit and the air re-circulates through the test section, while OCWT's have opened both ends and draw air from the atmosphere into the test section.

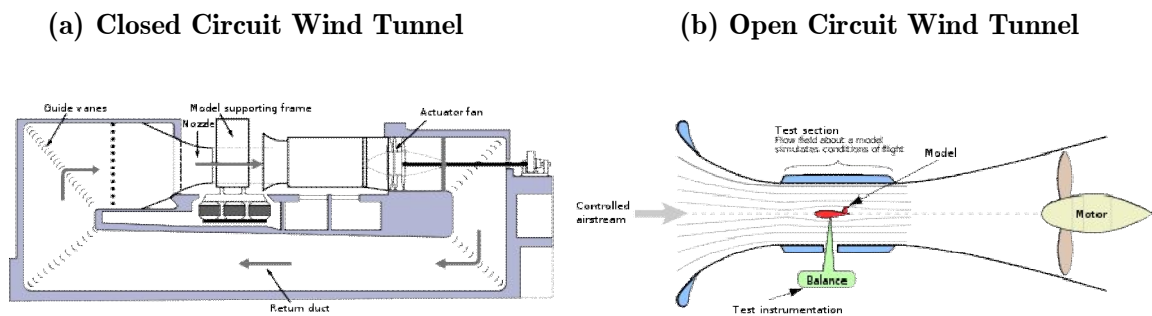


Figure 1.1. Classification of Wind Tunnel on basis of its Geometry as (a) CCWT and (b) OCWT

1.2 Computational Fluid Dynamics

Computational fluid dynamics (CFD) is the use of applied mathematics, physics and computational software to solve and analyse problems that involve fluid flows, and how those fluids affect objects as it flows past. Computational fluid dynamics is based on the

Navier-Stokes equations. These equations, which are explained more widely in section 2.2.1, describe how the velocity, pressure, temperature, and density of a moving fluid are related.

In a more inappropriate way, CFD can be seen as virtual experiments to substitute physical experiments. Computational fluid dynamics has been around since the early 20th century, and it has found its way in a broad variety of engineering fields, such as aeronautics, chemical, civil or environmental. One of the most successful applications of CFD has been in the field of wind tunnels, usually known as a Virtual Wind Tunnel (VWT), and in which this thesis is focused.

1.2.1 Computational Fluid Dynamics for wind tunnel simulations

During last years, computational fluid dynamics has significantly replaced the wind tunnels, since computers have become more powerful and the science behind CFD has lived great improvements. These advancements, both in computers and CFD have made possible to use a Desktop computer, instead being limited on mainframe computers. However, wind tunnels are sometimes used to verify the CFD computer codes.

Nowadays, everyone's main focus is to save time, material and reduce costs. This fact gives another advantage to CFD against wind tunnel, since CFD has same or lower cost and quicker turnover times to conduct the modelling in most cases, as well as wind tunnel require large expensive equipment.

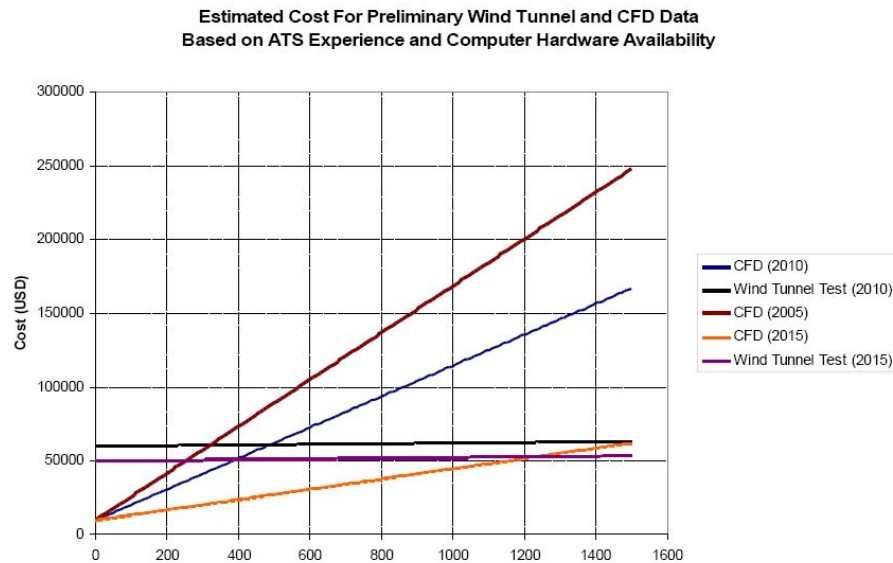


Table 1-1. Estimated cost for Wind Tunnel and CFD¹

Table 1-1 depicts the estimated costs for Wind Tunnel and Computational Fluid Dynamics in different years. As it can be observed, CFD has significantly reduced its costs during last 10 years and consequently, it has gain a great importance in its use against physical testing. It is noteworthy the lower initial cost of the CFD and how the cost notably increase per data point, while Wind Tunnel Testing behaves oppositely, it has a high initial cost with a low increment per data point.

The different parameters for estimating these costs are:

- *Computational fluid Dynamics:*
 - Software Costs
 - Basic licensing fees
 - Cost per parallel process
 - Hardware Costs
 - Cost per physical cpu core
 - Operating Cost
 - Time to solution and time per solution
 - Power Cost

¹Estimated cost for Wind Tunnel and Computational Fluid Dynamics. Data obtained from *Aeronautical Testing service, Inc. CFD and Wind Tunnel Testing: Complimentary Methods for Aircraft Design.*

- *Wind Tunnel Testing:*
 - Model Cost
 - Complexity of model
 - Quality of CAD definition
 - Time from CAD delivery to model delivery
 - Wind Tunnel Costs
 - Cost per hour of wind tunnel time
 - Cost for non-standard instrumentation
 - Operating Costs
 - Design of the model
 - Efficiency of staff
 - Efficiency of wind tunnel equipment and data reduction tools
 - Power cost

1.3 Inflatable structures

Inflatable structures, also known as pneumatic structures, are flexible membranes which are prestressed with pressurised air, and sometimes stiffened with cables to support traction against the action of external loads. Pneumatic structures are characterized by being lightweight easy to manipulate and transport.

1.3.1 Brief introduction to its history

Inflatable structures are rather recent. In 1917, Sir Frederic Lanchester lay down the first patent in pneumatic construction in Europe. Afterwards, Walter Bird and his team achieved the construction of a 15m diameter pneumatic dome, the prototype for a series of large shelters, called “radomes”, to protect radars used at the end of the World War II. Walter Bird also pioneered in the commercial application of pneumatics, such as in sport facilities, swimming pools or covers for warehouses.

The easy manipulation and transport of inflatable structures soon inspired their use in temporary and itinerant exhibitions. The use of these structures reached a peak in the EXPO’70 in Osaka, when all the pavilions in the exhibitions were built using inflatable

structures. They have been widely adopted in Japan ever since owing to the poor quality of the soil and high seismicity of the region. One of the most relevant pavilions was the *Fuji*, Figure 1.2, composed by 16 inflate arches and designed by architect Yutaka Murata.



Figure 1.2. Fuji pavilion, 1970, Osaka

Nowadays, inflatable structures have gained great importance in several other applications, in particular in aeronautics, where large inflatable airplane hangars, see Figure 1.3, are used to protect or repair aircrafts at arbitrary locations in case of emergency. Furthermore, companies such as BuildAir², are doing important researches in other uses of pneumatics structures, among others, air-bridges for emergencies in natural disasters, see Figure 1.4



Figure 1.3. Inflatable airplane hangar, BuildAir

² Buildair is an engineering and textile architecture company specialized in the design and development of large scale inflatable structures, such as Airplane aeronautical Hangars. CIMNE Tecnología SA, a company 100% owned by CIMNE, owns 5% of BUILDAIR. <http://buildair.com/en/index.htm>



Figure 1.4. Air bridge prototype designed by BuildAir

1.3.2 Structural behaviour of inflatable structures

Pneumatic structures can cover large surfaces without intermediate elements. They are manufactured with a textile structure, creating a uniform solid with membrane properties. The structure incorporates an action to the load system due to the internal pressure which is subjected onto the structural elements. The inflatable structures only resist against traction stresses. The membrane, under any load condition, must be kept tensioned, hence, the structure has to be subjected to an enough internal pressure to bear these load conditions. Typically, continuous air feeding via pressure pumps is supplied.

1.4 State-of-the-art in the computational modelling of inflatable structures

Nowadays, computational fluid dynamics is a widely developed tool for a wide range of problems. However, there exist several challenging fields requiring further development. One of these cases is the fluid-structure interaction, when light-weight solid is subjected to large displacements, as it is the case in inflatable structures due to the wind loads. Different attempts have been carried out in order to analyze these problems.

Until now, the industry market solves these problems separately. First, the pressures generated by a wind are calculated over a rigid body in a CFD model. Afterwards, the pressure distribution obtained from CFD is applied to the elastic body, representing the inflatable structures, in a traditional Computational Structural Dynamics (CSD) solver.

This method is a rough way to analyze this problem since, thin light-weight structures are subjected to large displacements and therefore, fluid has different behaviour.

Given the importance that the inflatable structures are having over the last years, the need arises to deeply study them behaviour, with the objective to analyze, asset and optimize the construction of these structures. The interdependence between the structural deformation and the surrounding flow calls for a strongly coupled solutions.

Monolithic approaches have been used to study the behaviour of FSI involving thin light-weight structures. However, the difficulty to describe the fluid in terms of displacements without using the pressure as a primary variable leads to a badly conditioned system matrices. Furthermore, the discrete equation system describing the problem is too large and therefore, high computational cost is arisen.

The aim of this project is to carry out a study of a light-weight structure of Buildair using a strong two-way coupling algorithm developed by Kratos Group, a research team of CIMNE. The algorithm allows analyzing a partitioned approach for fluid-structure interaction involving thin light-weight structures. Structure domain is embedded in the fluid domain. This type of approach relies on the independent solution of the fluid and the structural domain, hence the best available solvers for each sub-domain can be chosen. Also, partitioned approaches are cheaper than the monolithic ones. The embedded setting investigated in the present work allows avoiding the deficiencies (strong mesh distortions) experienced by the Arbitrary Lagrangian-Eulerian (ALE) methods when facing large deformation of the structure.

The successful application of the framework will be an important advance for computational methods in fluid-structure interaction problems involving thin light-weight structures subjected to large displacements. In addition, further analysis of them behaviour could be carried out, since the physical experiments in these structures are highly complicated and expensive.

References

1. Aeronautical testing Service, Inc., “CFD and Wind Tunnel Testing: Complimentary Methods for Aircraft Design”, Arlington, USA. 2010.
2. Basset Salom, Nuria, “Estructuras neumáticas”, *Class notes of Escuela Técnica Superior de Arquitectura*, Universidad Politécnica de Valencia.
3. Buildair Engineering + Architecture. www.Buildair.com
4. J.D. McAlpine, “Computational Fluid Dynamics or Wind Tunnel Modeling?”, Envirometries, Inc. Seattle, USA. 2004.
5. Jung Yun Chi1 and Ruy Marcelo de Oliveira Pauletti, “An outline of the evolution of pneumatic structures”, Faculty of Architecture and Urban Planning1, Polytechnic School. University of Sao Paulo.
6. P.B.S. Lissaman. “Low-Reynolds-Number Airfoils”, Inc. Pasadena, California. 91107
7. Vishvendra Singh, T. Et al , “Design, Analytical, Instrumentation and Flow Simulation of Sub-Sonic Open Circuit Wind Tunnel Model”. India: IJMER, Vol.4, 2014.

Chapter 2:

Fluid-Structure Interaction

2.1 Brief introduction to Fluid-structure interaction

Fluid-structure interaction (FSI) is a class of problems which describe a certain physical phenomena with mutual dependence between the fluid and structural mechanics models. The flow behaviour depends on the shape of the structure and its motion, and the motion and deformation of the structure depend on the fluid mechanics forces acting on the structure. This interaction between both systems, fluid and structure, is encountered almost everywhere in engineering, sciences and medicine. In some engineering projects, FSI plays an important role and influences the decisions in the design stage of projects of interest. Hence, reliable predictive FSI methods, which help address these problems of interest, are in high demand in research laboratories, space explorations, industry and many other contexts.

While analytical methods are used to some extent in solution of fluid-only or structure-only problems, only a handful of cases in solution of FSI problems have been solved analytically. Simplified assumptions (often, unrealistic) have been invoked to arrive at closed-form solutions of the underlying partial differential equations (PDE). The nonlinearity and time-dependent nature of FSI makes it very difficult to use analytical methods in this class of problems. On the other hand, there have been significant advances in computational FSI research during the last decades (see for instance, Tezduyar, 2003a, b [1], [2]; Michler et al., 2003 [3], 2004 [4]; van Brummelen and de Borst, 2005 [5]; Oñate et al., 2006 [6]; Ryzhakov et al., 2007 [7]; Idelsohn et al., 2008a [8],b [9]; Takizawa and Tezduyar, 2012b [10]). In the context of numerical methods, FSI involves a combination of Computation Fluid Dynamics (CFD) and Computational Structural Dynamics (CSD).

Fluid-structure interaction problems are concerned with mainly two types of interaction, *Momentum interaction* and *interaction of Energy*. Furthermore, inside the momentum interaction, the movement of the structure because of momentum exchange with the fluid can occur in two different ways (see Figure 2.1), by a local deformation of the solid body, or by a rigid body motion. This project is concerned with interaction of forces and the corresponding movement of the interface. The structure studied in this project is a flexible light-weight structure; therefore, it will be characterized by large displacements. Hence a local deformation will be necessarily analyzed.

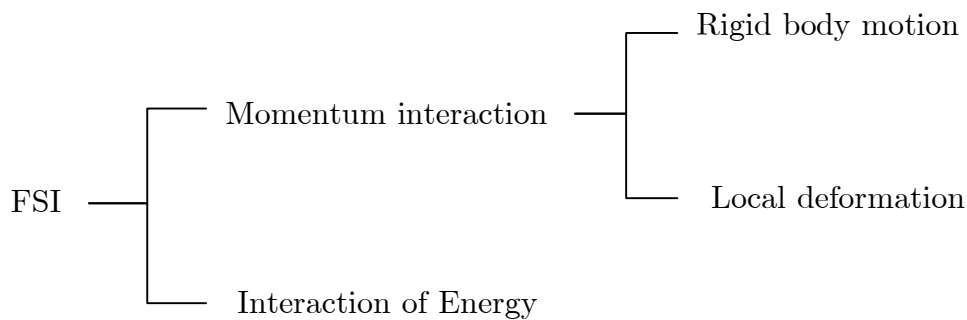


Figure 2.1. FSI categories

The development of computational FSI frameworks involved different challenges categorize into three areas: problem formulation, numerical discretization, and fluid-structure coupling. These challenges areas are explained in next sections.

2.2 Problem formulation

The **problem formulation** takes place at the continuous level, before discretization. However the chosen continuous model has implications for the numerical discretization that are most suitable for the case at hand. The situation for a FSI problem is more complicated than for a single-field mechanics problem, such as a fluid-only or structure-only problem, where it consists of with a set of governing differential equations in the problem domain and a set of boundary conditions at the domain boundary. In FSI, the sets of differential equations and boundary conditions associated to the fluid and structure domains must be satisfied simultaneously and respect the interface between both domains. The domains must not

overlap, and the two systems must be coupled at the fluid-structure interface, which requires a set of physically meaningful interface conditions. These coupling conditions are the compatibility of the kinematics and tractions at the fluid-structure interface.

Conservation laws can be expressed in two alternative ways. The first one considers the motion of all matter passing through a *fixed spatial location*. This description is generally used in Fluid Mechanics, where one is interested in properties, such as velocity, pressure, temperature, and so on, of the matter that instantly occupies the fixed spatial location. This description is known as the *Eulerian description*. The second description, known as *Lagrangian description*, focuses the attention on a *set of fixed material particles*, irrespective of their spatial locations. This alternative is commonly used in Solid Mechanics, and one has interest in the relative displacements of these particles and the stress caused by external forces and temperature.

In the following the mathematical models which describe the behaviour of FSI problems is presented.

Let us consider a solid body \mathbf{B} which is “embedded” inside a fluid domain Ω^f with external boundaries $\partial\Omega$ of the domain and $\partial\mathbf{B}$ boundary of \mathbf{B} (see Figure 2.2). A mathematical model for this FSI problem involves:

- governing equations for the fluid domain $\Omega^f(\mathbf{t}) \in \mathbb{R}^3$
- governing structural dynamic equations for the solid domain $\mathbf{B}(\mathbf{t}) \in \mathbb{R}^3$
- transmission conditions at the fluid-structure interface $\partial\mathbf{B}(\mathbf{t})$
- Dirichlet and Neumann boundary conditions at the remaining structural and fluid domain boundaries
- Initial conditions ($t=0$) for the fluid and structural state vectors

Herein, the fluid and structural problems will be described separately and then the interaction modelling of those sub problems across the interface will be introduced.

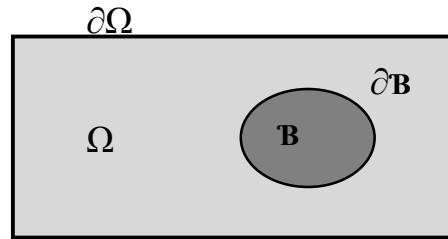


Figure 2.2. Representation of a solid body B immersed in a domain Ω^f , with the respective boundary, ∂B and $\partial\Omega$

2.2.1 Governing equations of fluid mechanics

Fluid flow is described by differential equations representing the interrelationship between the flow variables and their evolution in time and space. The laws of motion (mass, momentum and energy conservation) that apply to continuum solids are valid for all matter including liquids and gases. However, the main feature which distinguishes a fluid from a solid is the incapacity to resist shear stresses when remaining at rest. A fluid can resist shear stresses only when it is in motion. Hence, the shear stresses in a fluid are proportional to the time rate of strain. Thereby, independent variable is the velocity \mathbf{v} (m/s), and the proportionality parameter is the viscosity μ ($\text{Kg}\cdot\text{m}^{-1}\cdot\text{s}^{-1}$).

Motion of fluid is governed by the so-called Navier-Stokes equation. In the problem of interest and in many of civil engineering applications, air can be modelled as a viscous incompressible flow in the Navier-Stokes equations.

2.2.1.1 Conservation of Mass

Applying the *continuity equation*³ to the density of fluid ρ^f (kg/m^3), one obtains:

³The continuity equation is an equation which describes the change of an intensive property L , and is representing as

$$\frac{dL}{dt} + \nabla \cdot (L \mathbf{v} + Q) = 0$$

where \mathbf{u} and Q are the velocity and the sink term respectively.

$$\frac{\partial \rho^f}{\partial t} + \nabla \cdot (\rho^f \mathbf{v}) + Q = 0 \quad (2.1)$$

REMARK 2.1 The sink term it will not be considered as the project will be concerned with a constant control volume, with no sources or sinks of mass ($Q=0$).

Hence, the equation of conservation of mass, can be represented as

$$\frac{\partial \rho^f}{\partial t} + \nabla \cdot (\rho^f \mathbf{v}) = 0 \quad (2.2)$$

It is worth mentioning that in fluid mechanics modelling, the control volume fixed in space is typically considered. This is known as the *Eulirian formulation*. Therefore, the *material derivative* or *Eulirian derivative* operator D/Dt must be introduce.

$$\frac{D}{Dt} = \frac{\partial}{\partial t} + \mathbf{v} \cdot \nabla \quad (2.3)$$

Applying the Eulirian derivative to equation (2.2), the conservation of mass can be expressed in the alternative form

$$\frac{D\rho^f}{Dt} + \rho \nabla \cdot \mathbf{v} = 0 \quad (2.4)$$

When the density changes following a fluid particle are negligible, the fluid continuum is termed *incompressible fluid*. Setting the derivative of density equal to zero $D\rho^f/Dt=0$, the conservation of mass (2.4) becomes

$$\nabla \cdot \mathbf{v} = 0 \quad (2.5)$$

2.2.1.2 Conservation of Momentum: Equation of Motion

The derivation of conservation of momentum equations can be done using Newton's laws and applying the chain rule. Basic physics dictates that

$$\mathbf{F} = m\mathbf{a} \quad (2.6)$$

Allowing for the body force $\vec{F} = \vec{b}$ and substituting density for mass, since it is operating with a fixed control volume and infinitesimal fluid parcels, it is obtained the similar equation

$$\mathbf{b} = \rho^f \frac{\partial}{\partial t} \mathbf{v}(x, y, z, t) \quad (2.7)$$

Applying the chain rule to the derivative of velocity

$$\mathbf{b} = \rho^f \left(\frac{\partial \mathbf{v}}{\partial t} + \frac{\partial \mathbf{v}}{\partial x} \frac{\partial x}{\partial t} + \frac{\partial \mathbf{v}}{\partial y} \frac{\partial y}{\partial t} + \frac{\partial \mathbf{v}}{\partial z} \frac{\partial z}{\partial t} \right) \quad (2.8)$$

Equivalently,

$$\mathbf{b} = \rho^f \left(\frac{\partial \mathbf{v}}{\partial t} + \mathbf{v} \cdot \nabla \mathbf{v} \right) \quad (2.9)$$

Hence, substituting the value in parentheses in equation (2.9) for the definition of the Eulerian derivative, the equation can be expressed as

$$\rho^f \frac{D\mathbf{v}}{Dt} = \mathbf{b} \quad (2.10)$$

By adding few assumptions about the forces and the behaviour of fluids, the conservation of Momentum derived above leads to the equations of motion for fluids. It is assumed that the body force on the fluid parcels is owing to two components, fluid stresses and other external forces.

$$\mathbf{b} = \nabla \cdot \boldsymbol{\sigma}^f + \mathbf{f} \quad (2.11)$$

Hence, the principle of conservation of linear momentum (or Newton's Second Law of motion) can be written as

$$\rho^f \frac{D\mathbf{v}}{Dt} = \nabla \cdot \boldsymbol{\sigma}^f + \mathbf{f} \quad (2.12)$$

where $\boldsymbol{\sigma}^f$ is the Cauchy stress tensor (N/m^2) and \mathbf{f} is the body force vector, measured per unit of mass.

The Navier-Stokes equation (2.12) is an equation which can be used to determine the velocity vector field that applies to a fluid, given some initial conditions. They arise from the conservation of momentum in combination with a constitutive law for fluid stress (due to viscosity) and a pressure term.

2.2.1.3 Constitutive equations

The Cauchy stress tensor $\boldsymbol{\sigma}$ commented above is often, for incompressible fluids, decomposed into two terms. These two terms are the volumetric stress tensor, and the stress deviator tensor, or also termed as the hydrostatic and viscous part respectively:

$$\boldsymbol{\sigma}^f = -p\mathbf{I} + \boldsymbol{\tau} \quad (2.13a)$$

or in matrix notation

$$\boldsymbol{\sigma}^f = \begin{pmatrix} \sigma_{xx} & \tau_{xy} & \tau_{xz} \\ \tau_{yx} & \sigma_{yy} & \tau_{yz} \\ \tau_{zx} & \tau_{zy} & \sigma_{zz} \end{pmatrix} = -\begin{pmatrix} p & 0 & 0 \\ 0 & p & 0 \\ 0 & 0 & p \end{pmatrix} + \begin{pmatrix} \sigma_{xx} + p & \tau_{xy} & \tau_{xz} \\ \tau_{yx} & \sigma_{yy} + p & \tau_{yz} \\ \tau_{zx} & \tau_{zy} & \sigma_{zz} + p \end{pmatrix} \quad (2.15b)$$

where P is the hydrostatic pressure, \mathbf{I} is the unit tensor and $\boldsymbol{\tau}$ is the viscous stress tensor.

Applying this form of the Cauchy stress tensor into the equation of the continuum momentum (2.12), the most general form of the Navier-Stokes equation can be expressed as

$$\rho^f \frac{D\mathbf{v}}{Dt} = -\nabla p + \nabla \cdot \boldsymbol{\tau} + \mathbf{f} \quad (2.14)$$

- $\rho^f \frac{D\mathbf{v}}{Dt}$: Represents the inertia.
- $-\nabla p$: Is the pressure gradient term, which prevents motion due to normal stresses. The fluid presses against itself and keeps it from shrinking in volume.
- $\nabla \cdot \boldsymbol{\tau}$: Is the viscous stress term, which causes motion due to horizontal friction and shear stresses. The shear stress causes turbulence and viscous flows.
- \mathbf{f} : Represents the force term which is acting on every single fluid particle.

The equation (2.14) is the general form of the Navier-Stokes equation for incompressible fluids.

For *Newtonian Fluids*, such as e.g. air, the basis of the assumptions is about the nature of the viscous stress tensor $\boldsymbol{\tau}$. The stress is proportional to the rate of deformation

$$\tau_{ij} = \mu \left(\frac{\partial v_i}{\partial x_j} + \frac{\partial v_j}{\partial x_i} \right) \quad (2.15)$$

The proportionality constant μ is the viscosity, mentioned in the beginning of the section 2.2.1 of this chapter, and it defines how easily the fluid flows when is subjected to body forces.

Applying the expression (2.15) in the term of the divergence of the viscous stress tensor in the equation (2.14), it is obtained the vector Laplacian

$$\boldsymbol{\nabla} \cdot \boldsymbol{\tau} = \mu \boldsymbol{\nabla}^2 \mathbf{v} \quad (2.16)$$

Finally, the Navier-Stokes equation for an incompressible Newtonian fluid, in the convective form, can be written as

$$\rho^f \frac{D\mathbf{v}}{Dt} = -\boldsymbol{\nabla} p + \mu \boldsymbol{\nabla}^2 \mathbf{v} + \mathbf{f} \quad (2.17)$$

2.2.2 Governing equations of structural mechanics

The behaviour of the structural domain \mathbf{B} (Figure 2.2) is generally described using a Lagrangian description. The momentum equation governing the motion of the body is

$$\rho^s \ddot{\mathbf{u}} = \boldsymbol{\nabla} \cdot \boldsymbol{\sigma}^s + \rho^s \mathbf{f} \quad (2.18)$$

where \mathbf{y} is the displacement, $\boldsymbol{\sigma}^s$ is the Cauchy stress tensor of the structure and \mathbf{f} the external body force per unit of mass.

REMARK 2.2: Note the emphasis dot over the displacements ($\ddot{\mathbf{u}}$) represents the second partial derivative respect to time $\left(\frac{\partial^2}{\partial t^2}\right)$, so $\ddot{\mathbf{u}}$ represents the structural acceleration.

The compatibility conditions are expressed as

$$\begin{aligned}
t_j &= n_i \sigma_{ij} = \bar{t}_j \quad \text{on } \partial\mathcal{B}_t \subset \partial\mathcal{B}, \\
\sigma_{ij} &= \sigma_{ji} \\
\varepsilon_{ij} &= \frac{1}{2} \left(\frac{\partial u_j}{\partial x_i} + \frac{\partial u_i}{\partial x_j} \right) \\
u_j &= \bar{u}_j \quad \text{on } \partial\mathcal{B}_u \subset \partial\mathcal{B}
\end{aligned} \tag{2.19}$$

where σ_{ji} is the Cauchy stress tensor, $x_i = [x_1, x_2, x_3]$ the Cartesian coordinates of a given point of the underformed body, \bar{u}_j the displacement imposed on the Dirichlet boundary $\partial\mathcal{B}_u$, t_j the surface tractions (\bar{t}_j is the surface traction applied on the Neumann boundary $\partial\mathcal{B}_t$, n_i the outward normal vector of the surface and ε_{ij} is the strain tensor.

2.2.2.1 Constitutive law

A constitutive law that expresses the stress tensor in terms of displacement or velocity is required. The structures considered in this thesis can be modelled using linear elasticity, since permanent deformations are negligible

$$\sigma_{ij} = C_{ijkl} \varepsilon_{kl} \tag{2.20}$$

where C_{ijkl} is the constitutive material matrix.

$$C_{ijkl} = \begin{bmatrix} \frac{E_1}{(1 - \nu_{12}\nu_{21})} & \frac{\nu_{21}E_1}{(1 - \nu_{12}\nu_{21})} & 0 \\ \frac{\nu_{12}E_2}{1 - \nu_{12}\nu_{21}} & \frac{E_2}{(1 - \nu_{12}\nu_{21})} & 0 \\ 0 & 0 & G_{12} \end{bmatrix} \tag{2.21}$$

Here, E_1 and E_2 are the Young's moduli in the directions defined by the local basis vectors, ν_{12} and ν_{21} are the Poisson's ratios, G_{12} is the shear modulus, and $\nu_{21}E_1 = \nu_{12}E_2$ in order to ensure the symmetry of the constitutive material matrix. In the case of an isotropic material, $E_1 = E_2 = E$, $\nu_{21} = \nu_{12} = \nu$, and $G_{12} = E/(2(1 + \nu))$.

2.2.3 Interface conditions

To describe and model the interaction between the external fluid domain Ω^f and the immersed structural body \mathbf{B} , a set of interface conditions must be enforced on the boundary $\partial\mathbf{B}$. The main coupling conditions to satisfy the interaction are the dynamic and kinematic

compatibility. No mass flow across the interface is assumed and a viscous fluid is considered. Hence the normal and tangential velocities have to match the following *continuity conditions*:

$$\mathbf{v} \cdot \mathbf{n}^f = -\dot{\mathbf{u}} \cdot \mathbf{n}^s \quad \forall \mathbf{x} \in \partial \mathcal{B} \quad (2.22)$$

$$\mathbf{v} = \dot{\mathbf{u}} \quad \forall \mathbf{x} \in \partial \mathcal{B} \quad (2.23)$$

The equilibrium condition requires the surface traction to be equal as

$$\boldsymbol{\sigma}^f \cdot \mathbf{n}^f = \boldsymbol{\sigma}^s \cdot \mathbf{n}^s \quad (2.24)$$

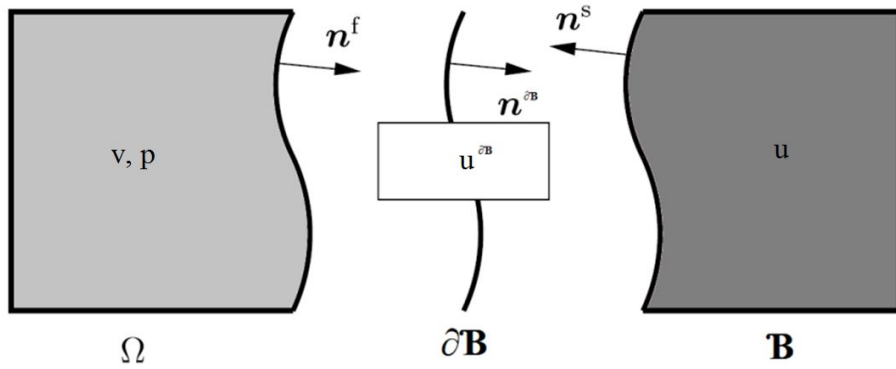


Figure 2.3. Matching interface conditions for a fluid-structure interaction

2.3 Body fitted and non-body fitted meshes

Let us consider now the issues related to the relative motion of the computational domains in the FSI problem. Let us consider (at a conceptual level) the two computational meshes and corresponding formulations: one for the structure, and another one for the fluid.

The structural domain, typically described in the Lagrangian framework, follows the material particles belonging to the structure. This is known as the Lagrangian description of the structural motion. The shape of the fluid domain has to change in order to conform to the motion of the structure, as the solid deforms in space. On the other hand, in the

Eulerian description, which is widely used in fluid dynamics, the mesh remains fixed and the continuum moves with respect to the grid.

There are two major classes of methods to account for the interfaces bodies moving inside the fluid domain. These methods are known in the discrete setting as the Body-fitted mesh (BF) methods and the Non-body-fitted mesh (NBF) methods.

It is worth noting that this thesis deals with an embedded approach, a Non-body fitted method.

2.3.1 Body-fitted mesh

The main feature of the BF mesh methods is that they operate on dynamic, body-conforming CFD grids and a particular algorithm takes care of the mesh motion (deformation) to accommodate the body motion and maintain a conformal CFD wet surface of the solid body.

2.3.1.1 Moving mesh method

The *moving mesh method* is based on a Lagrangian flow formulation, and dynamic finite element meshes. The dynamic wet interface is treated with a material flow description to avoid the additional tracking of the moving boundaries. However, the dynamic meshes that propagate with the flow become distorted and should be regenerated at each time step. It relocates grid points in a mesh having a fixed number of nodes in such a way that the nodes remain concentrated in regions of rapid variation of the solution. This approach becomes impractical for high Reynolds number problems that require large and fine meshes. The method requires, at each time step, a remeshing procedure which has an expensive computational cost. For extensive reviews in this approach see Tao Tang [11]; Andrew A. Johnson [12]; R. Radovitzky, M. Ortiz [13] and [14].

2.3.1.2 The Arbitrary Lagrangian-Eulerian (ALE) method

The Arbitrary Lagrangian-Eulerian is a method in which the computational system is neither fixed in space (Eulerian description) nor attached to material particles (Lagrangian description). ALE is a method which combines the advantages of the classical kinematical descriptions, a well defined interface and facility in imposing the boundary conditions (Lagrangian description) and the possibility of handling deformation (Eulerian description).

In this approach, the continuum moves relative to the mesh as in Eulerian framework, but in the Fluid-structure interface, also known as the *wet interface*, the grid is controlled by the boundary conditions of the problem as in a Lagrangian formulation.

The main disadvantage of this approach is that for large deformation and topological changes, some pseudo-structural edges can penetrate their neighbouring triangles and produce negative volume elements, in these occasions it is produced numerical errors.

ALE methods can be equipped with the re-meshing technique similarly to the Lagrangian methods. However, it greatly impacts the computational cost of the method.

2.3.2 Non body-fitted mesh (NBF)

Non body-fitted mesh differs from the BF in that the grids do not conform to the surface of the body (see Figure 2.4). The whole domain is discretized by a Cartesian grid, extending through solid walls within the computational domain. This transforms the problem from conforming the meshing to the surface into a characterizing and computing the intersection between the Cartesian grid and the surface geometry. Hence, the cells of the mesh are flagged in three different groups: *solid cells*, if they belong inside the embedded body where no flow computations will take place, *flow cells*, if they belong to the region where the flow computations take place, and *boundary cells*, for those cells where the solid boundary intersects the mesh, see Figure 2.5.

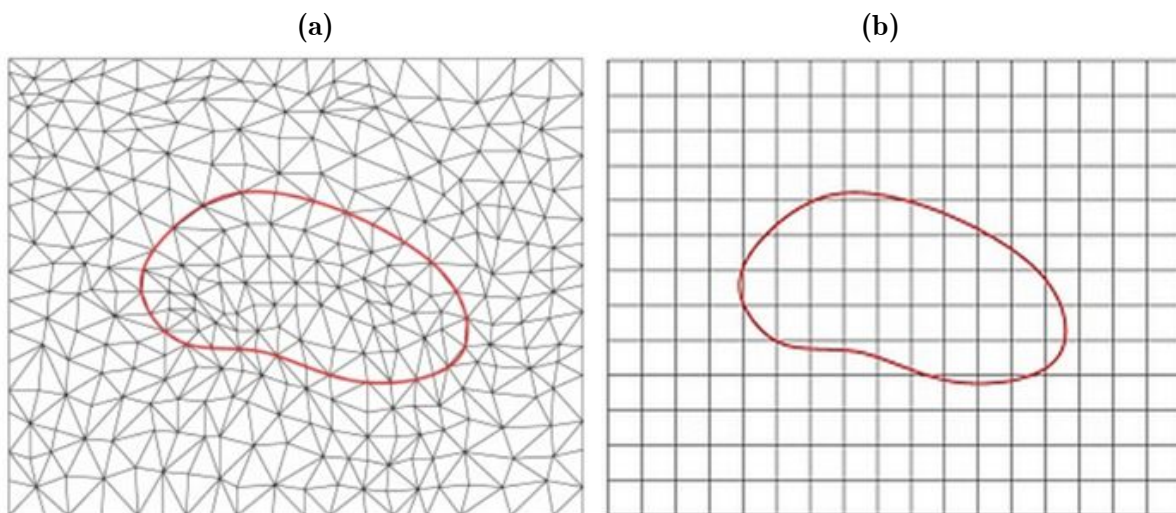


Figure 2.4. Representation of a Body-fitted mesh (a), and a Non Body-fitted mesh (b)

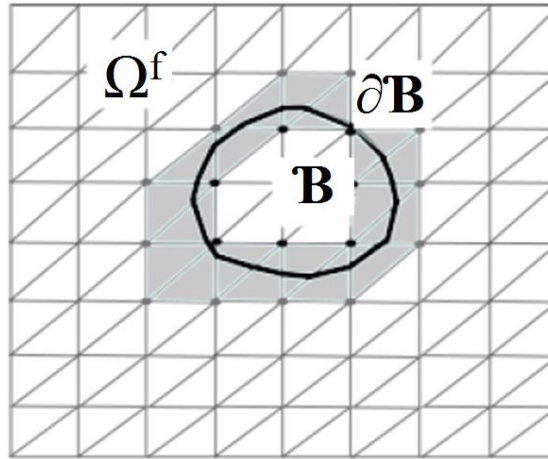


Figure 2.5. Interface elements. Solid cells: elements inside the black polyline. Boundary cells: elements represented in colour grey. Flow cells: elements outside black polyline and belonging to the fluid domain Ω^f

What distinguishes one type of NBF method from the other is the way boundary conditions are treated. Modifications of the governing equations are needed in the vicinity of the boundary cells to assign the appropriate boundary conditions. One approach is to impose boundary conditions using a forcing function and extrapolation of the variables. For more details see (R. Glowinski et al [15]; J. Mohd-Yosuf [16]; Y.H. Tseng, J.H. Ferziger [17]; or A. Gertenberger, W.A. Wall [18]).

2.4 Fluid-structure coupling

There exist two different approaches to face FSI coupling problems: *monolithic* and *partitioned*.

In the *Monolithic approach* the equations of fluid, structure and interface are solved simultaneously at every time step. The monolithic solution is more robust, a main advantage for adopting this approach. However, some complications arise when dealing with monolithic approach. The variables describing the fluid and the solid are of different nature, which generally leads to badly conditioned system matrices. Furthermore, the single discrete equation system describing the FSI problem is larger than the subsystem (fluid and structure) of the problem. Success of the monolithic approaches greatly depends on the

availability of efficient preconditioners capable of accelerating the solution of large, heterogeneous and poorly conditioned linear systems

Partitioned approaches rely on the decomposition of the problem into different sub-problems. In FSI the problem is decomposed into fluid and structure subdomains. Each one is independently solved and the data is interchanged between them through the interface boundary. Hence, the best available solver for each sub-problem can be chosen. Nevertheless, though partitioned approach works well and is very efficient for several problems, it may suffer from stability problems (convergence difficulties are encountered).

These difficulties most-commonly arise when the structure is light and the fluid is heavy. The interaction between the subdomains can be performed in two different ways. If there is not feedback between fluid and structure, the interaction is called *one-way coupling*, while if there is feedback between subsystems the interaction is called *two-way coupling*. Figure 2.6 depicts a scheme of the different ways to deal with the interaction between both subdomains. Weak one-way coupling neglects the effect of the structural motion upon the flow. This is generally valid assumption for heavy rigid structures undergoing minor motions. However, for light-weight structures in which large deformation in the structure are produced, the motion of the structure has a non-negligible effect upon the flow of the air. Here, is when the application of a two-way coupling approach makes sense.

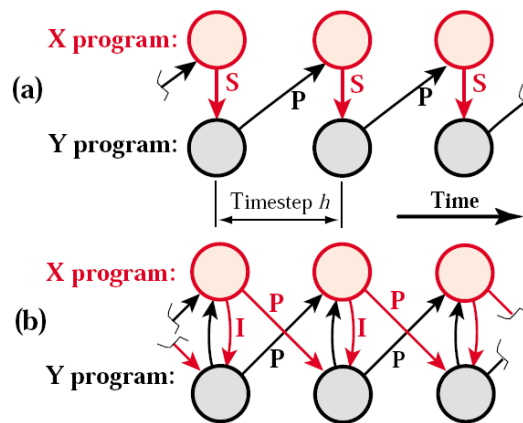


Figure 2.6⁴. Two different approach for interaction between subdomains: (a) One-way coupling (b) two-way coupling

⁴ Figure reprint from class notes of *Synthesis Tools for Structural Dynamics and Partitioned Analysis of Coupled Systems*, C.A. Felippa and K.C. Park, University of Colorado at Boulder.

In the present work we shall analyze whether two-way coupling is necessary for the simulation involving light-weight structures by comparing one-way and two-way coupled solutions.

References

1. C.A. Felippa and K.C. Park, "Synthesis Tools for Structural Dynamics and Partitioned Analysis of Coupled Systems", class notes ASEN 5509, Dpt. Aerospace Engineering Science, University of Colorado, Boulder, USA, 2014.
2. C. G. Giannopapa, "Fluid Structure Interaction in flexible vessels", PhD thesis, Dpt. Philosophy of the University of London, King's College London, 2004
3. J. Donea, Antonio Huerta, J.-Ph. Ponthot and A. Rodríguez-Ferran, "Arbitrary Lagrangian-Eulerian Methods", *Encyclopedia of Computational Mechanics*, vol. 1: Fundamentals, Chapter 14, 2004.
4. J.N. Reddy and D.K. Gartling, *The Finite Element Methods in Heat Transfer and Fluid Dynamics*, Second Edition ed. Florida, USA: CRC Press, 2000.
5. M. Pisanoni, "Embedded Boundary Method for aerospace problems", Msc Thesis, Faculty of Aerospace Engineering, Delft University of Technology, Delft, 2013.
6. P.B. Ryzhakov, R. Rossi, S.R. Idelsohn, E. Oñate, "A monolithic Lagrangian approach for fluid-structure interaction problems", *Computational Mechanics*, vol. 46, pp. 883-899, 2010.
7. R.L. Taylor y P. Nithiarasu O.C. Zienkiewicz, *El Método de los Elementos Finitos: Dinámica de fluidos*, Sexta edición ed., M. Cervera, E. Oñate G. Bugeda, Ed. Barcelona, España: CIMNE, 2005.
8. R. Rossi, P. B. ryzhakov, E. Oñate, "A monolithic FE formulation for the analysis of membranes in fluids", *Internal Journal of Space Structures*, vol.24, Num. 4, 2009.
9. S.A. Carrillo, "Cartesian Grid Generation", October 2013.
10. Wolfgang A. Wall Axel Gerstenberger, "An eXtended Finite Element Method/Lagrange multiplier based approach for fluid-structure interaction," *Computer methods in applied mechanics and engineering*, vol. 197, pp. 1699-1714, 2008.

11. Yuri Bazilevs, Kenji Takizawa, Tayfun E. Tezduyar, *Computational Fluid-Structure Interaction: Methods and applications*, A John Wiley & Sons, Ltd., 2013.

Chapter 3:

Two-way FSI coupling algorithm

In this chapter the algorithm implemented for modelling and simulation of light-weight structures subjected to wind loads will be presented in detail. First, a description of the overall framework will be introduced. Afterwards, the discrete formulations and related solution procedure used for the fluid and the structure domains are explained. Finally, the coupling will be described.

As commented in previous chapters, this thesis is concerned with inflatable structures and wind loads. Hence, membrane elements are used to model the structure domain, and incompressible viscous fluid is assumed for the fluid domain.

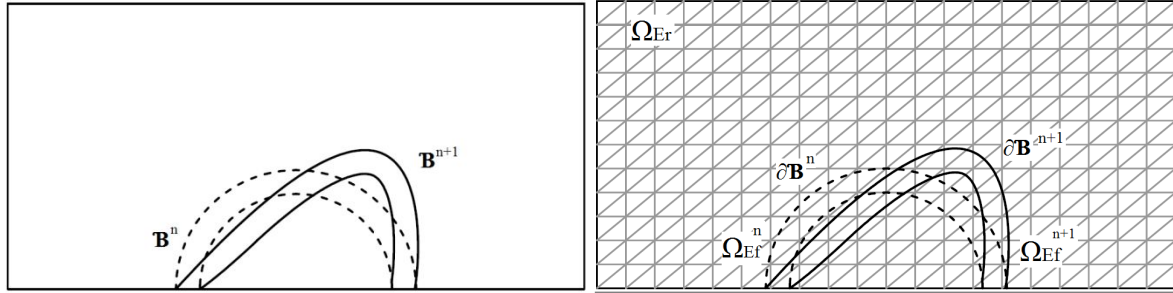
The code of the corresponding algorithms is presented in Annex I.

3.1 Overall embedded solution

The problem of interest is a FSI related to light-weight structures. These types of structures are known for undergoing large displacements due to wind loads. A partitioned coupling approach is implemented in order to obtain a computationally efficient simulation tool. The two sub-problems analyzed in the partitioned approach are the fluid domain, which is modelled in an Eulerian description, and the structure domain, modelled by a Lagrangian one.

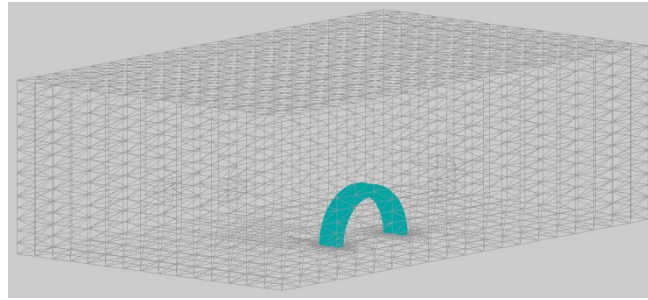
In the present problem, the solid body moves inside a fluid domain. Large deformations are expected at the interface, thus precluding the use of the mesh-fitted methods. Hence, an embedded approach is used for the discretization of the fluid and structure domain. In that way, mesh distortions due to large displacements and remeshing will be avoided, keeping the system far from numerical errors and reducing computational cost.

Since the structure domain moves inside the fluid domain, the fluid must deform according to the immersed body motion. The position of the Lagrangian domain within the Eulerian mesh, along time, defines the location of the fluid-structure interface at every time step; see Figure 3.1 for a graphical representation. From now on let us call the representation of the solid within the Eulerian domain as the Lagrangian image.



(a) Lagrangian domain -2D

(b) Eulerian domain and Lagrangian image -2D



(c) Eulerian domain and Lagrangian image – 3D representation

Figure 3.1. Embedded approach: movement of the Lagrangian domain and its image within the Eulerian mesh from time step t_n to t_{n+1}

The representation of the Lagrangian domain within the Eulerian mesh leads to a differentiation of the fluid domain into two parts. The part of the Eulerian domain lying inside of the Lagrangian image, which is referred to as “fictitious Eulerian domain Ω_{Ef} ” with its corresponding nodes “fictitious nodes”, and the part representing the fluid which is called “real Eulerian domain Ω_{Er} ” and the corresponding nodes “real nodes”, see Figure 3.1.a. The interface which divides the Eulerian domain into two parts is the boundary of the Lagrangian image $\partial\mathbf{B}$. The elements cut by the Lagrangian image boundary $\partial\mathbf{B}$ are also distinguished from the other elements. Those elements contain both real and fictitious nodes. Figure 3.1.b depicts a graphical representation, where the boundary $\partial\mathbf{B}$ is

represented as a black polyline, the interface elements are shown in grey, fictitious and real nodes are indicated by black and grey dots respectively.

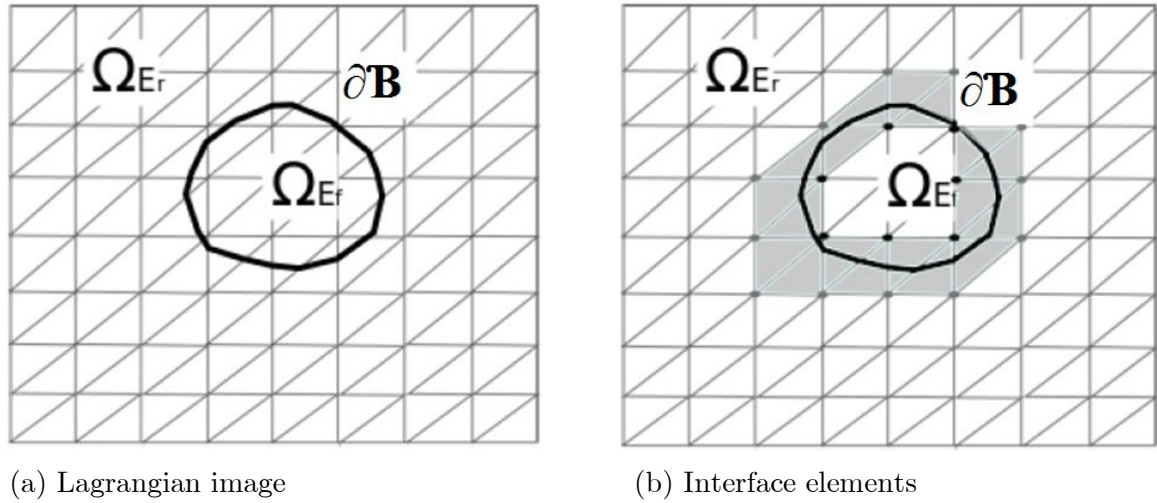


Figure 3.2. Embedded setting: real, fictitious and interface parts of the Eulerian domain⁵

The Lagrangian image in the fluid model is obtained by using space-search techniques (quad or oct-tress) and subsequent ray casting, see de Berg M et al [19], Yang S. et al [20] and Baumgartner D. and Wolf J. [21] for a wide description of the methods and their implementation. These techniques allows to described a signed distance function defined over the Eulerian mesh which distinguish the nodes lying outside and inside the Lagrangian image with positive and negative values on the prescribed distance variable, respectively. The position of the interface $\partial\mathbf{B}$ is defined by those nodes containing a zero value in the distance function.

The fictitious nodes of the interface elements are used exclusively for imposing the Dirichlet boundary condition representing the effect of the structural velocity. Fully fictitious elements are “switched off” thus enabling for natural representation of the pressure discontinuity across the interface.

Following, the model for the fluid and the structure are going to be presented, as well as the coupling scheme for boundaries conditions.

⁵ Figure reprint from P.B. Ryzhakov, A. Jarauta. “An embedded approach for immiscible multi-fluid problems”, *International Journal for Numerical Methods in Fluids*, 00: 1-33, 2015

3.2 Model for the fluid

The laws governing the flow of viscous incompressible Newtonian fluids, in the Eulerian form, have been described in the previous chapter (2.2.1). Nevertheless, they are represented here in order to facilitate the reading of the derivation of the discrete equations.

Conservation of mass:

$$\nabla \cdot \mathbf{v} = 0 \quad (3.1)$$

Conservation of Momentum:

$$\rho \frac{\partial \mathbf{v}}{\partial t} + \rho \mathbf{v} \cdot \nabla \mathbf{v} + \nabla p - \nabla \cdot (\mu \nabla^T(\mathbf{v})) - \rho \mathbf{g} = 0 \quad (3.2)$$

where \mathbf{v} denotes the velocity vector, ρ the density, p the pressure, μ the dynamic viscosity and \mathbf{g} the body force.

The boundary conditions are given by

$$\mathbf{v} = \mathbf{f}^v \quad \text{on } \Gamma_v \quad (3.3)$$

$$\boldsymbol{\tau} = \boldsymbol{\sigma} \cdot \hat{\mathbf{n}} = \mathbf{f}^\tau \quad \text{on } \Gamma_\tau \quad (3.4)$$

where $\boldsymbol{\tau}$ is the viscous stress tensor, $\boldsymbol{\sigma}$ is the total stress tensor, $\hat{\mathbf{n}}$ is the outward unit normal to the boundary, \mathbf{f}^v and \mathbf{f}^τ are specific functions for standard situations on the Dirichlet (Γ_v) and Neumann (Γ_τ) boundaries, respectively. With $\Gamma_f = \Gamma_v \cup \Gamma_\tau$, being Γ_f the total boundary enclosing the fluid domain, Ω_f .

The development of the finite element model for the continuity equation (Eq. (3.1)) and Navier-Stokes equation (Eq. (3.2)), which is used to construct the weak form is the so-called *mixed model*. This model mixes the velocity variables with the force-like variable –pressure–, and both types of variables are retained in a single formulation.

To obtain the weak form, the equations (3.1) and (3.2) are multiplied by a weight functions. The weight-integral statements of the two equations over a typical element Ω_e are given by

$$\int_{\Omega_e} Q \nabla \cdot \mathbf{v} \, d\Omega_e \quad (3.5)$$

$$\int_{\Omega_e} w \cdot \left[\rho \frac{\partial \mathbf{v}}{\partial t} + \rho \mathbf{v} \cdot \nabla \mathbf{v} + \nabla p - \nabla \cdot (\mu \nabla^T(\mathbf{v})) - \rho \mathbf{g} \right] d\Omega_e \quad (3.6)$$

where Q and w are the weight functions, which will be equated to the interpolation functions used for p and \mathbf{v} respectively, in the Ritz-Galerkin finite element modelling. Integration-by-parts, to equally distribute integration between the dependent variables and the weight functions, is used to obtain the weak form of the Navier-Stoke equation (3.2). However, no integration-by-parts is used in the conservation of mass equation (3.1) due to no relaxation of differentiability on \mathbf{v} can be accomplished. Hence, developing equations (3.5) and (3.6), the complete develop weak form can be described

$$0 = \int_{\Omega_e} Q \nabla \cdot \mathbf{v} \, d\Omega_e \quad (3.7)$$

$$0 = \int_{\Omega_e} [\rho(w \cdot \nabla \dot{\mathbf{u}} + w \mathbf{v} \cdot \nabla \mathbf{v}) + \nabla w (-pI + \mu(\nabla \cdot \mathbf{v})) - \rho w \mathbf{f}] \, d\Omega_e - \oint_{\Gamma_e} w \boldsymbol{\tau} \, d\Gamma_e \quad (3.8)$$

3.2.1 Spatial discretization

Developing the Ritz-Galerkin finite element model, and supposing that the dependent variables (v_i, p) are approximated with a liner interpolation

$$v_i(\mathbf{x}, t) = \sum_{m=1} N_m(\mathbf{x}) v_1^m(t) = \mathbf{N}_v^T \mathbf{v} \quad (3.9)$$

$$p(\mathbf{x}, t) = \sum_{l=1} N_l^T(\mathbf{x}) p_1(t) = \mathbf{N}_p^T \mathbf{p} \quad (3.10)$$

where \mathbf{N}_v and \mathbf{N}_p are column vectors of shape functions for velocity and pressure, respectively, and $\bar{\mathbf{v}}$ and $\bar{\mathbf{p}}$ are vectors of nodal values of velocity components and pressure, respectively.

Substituting equations (3.9) and (3.10) into equations (3.1) and (3.2), the finite element equations are stated as follow

Conservation of mass (Continuity):

$$-\left[\int_{\Omega_e} \mathbf{N} \nabla \mathbf{N}^T d\Omega_e\right] \bar{\mathbf{v}} = 0 \quad (3.11)$$

i-th Momentum:

$$\begin{aligned} \left[\rho \int_{\Omega_e} \mathbf{N} \mathbf{N}^T d\Omega_e\right] \frac{d\bar{\mathbf{v}}}{dt} + \left[\rho \int_{\Omega_e} \mathbf{N} (\bar{\mathbf{v}} \cdot \nabla \mathbf{N}) d\Omega_e\right] \bar{\mathbf{v}} + \left[\mu \int_{\Omega_e} \nabla \mathbf{N} \nabla \mathbf{N}^T d\Omega_e\right] \bar{\mathbf{v}} \\ - \left[\int_{\Omega_e} \nabla \mathbf{N} \mathbf{N} d\Omega_e\right] \bar{\mathbf{p}} = \left[\rho \int_{\Omega_e} \mathbf{N} \bar{\mathbf{f}} d\Omega_e\right] + \left\{ \oint_{\Gamma_e} \bar{\boldsymbol{\tau}} \mathbf{N} d\Gamma_e \right\} \end{aligned} \quad (3.12)$$

where the superscript $(\cdot)^T$ denotes a transpose of the enclosed vector or matrix. The above equations (3.11) and (3.12) can be expressed in matrix form as

Continuity:

$$\mathbf{D} \bar{\mathbf{v}} = 0 \quad (3.13)$$

Momentum:

$$\mathbf{M} \frac{d\bar{\mathbf{v}}}{dt} + \mathbf{K}(\bar{\mathbf{v}}) \bar{\mathbf{v}} + \mu \mathbf{L} \bar{\mathbf{v}} + \mathbf{G} \bar{\mathbf{p}} = \mathbf{F} \quad (3.14)$$

where \mathbf{M} is de mass matrix, $\mathbf{K}(\bar{\mathbf{v}})$ is the nonlinear convection operator, \mathbf{L} is the Laplacian matrix, \mathbf{G} is the gradient matrix, $\bar{\mathbf{v}}$ and $\bar{\mathbf{p}}$ are the velocity and pressure, respectively, and \mathbf{F} is the body force vector.

The assembled matrices shown in Eq. (3.13) and (3.14) are defined as

$$\mathbf{M} = \rho \int_{\Omega_e} \mathbf{N} \mathbf{N}^T d\Omega_e \quad (3.15)$$

$$\mathbf{K}(\bar{\mathbf{v}}_{n+1}) = \rho \int_{\Omega_e} \mathbf{N}(\bar{\mathbf{v}} \cdot \nabla \mathbf{N}) d\Omega_e \quad (3.16)$$

$$\mathbf{L} = \int_{\Omega_e} \nabla \mathbf{N} \nabla \mathbf{N}^T d\Omega_e \quad (3.17)$$

$$\mathbf{G} = - \int_{\Omega_e} \nabla \mathbf{N} \mathbf{N} d\Omega_e \quad (3.18)$$

$$\mathbf{F} = \left[\rho \int_{\Omega_e} \mathbf{N} \bar{f} d\Omega_e \right] + \left\{ \oint_{\Gamma_e} \bar{\boldsymbol{\tau}} \mathbf{N} d\Gamma_e \right\} \quad (3.19)$$

$$\mathbf{D} = -\mathbf{G}^T \quad (3.20)$$

\mathbf{N} stands for the vector of standard linear shape functions, and Ω_e is the element integration domain.

The system can be written in the matrix form as

$$\begin{pmatrix} \frac{\mathbf{M}}{dt} + \mathbf{K}(\bar{\mathbf{v}}) + \mu \mathbf{L} & \mathbf{G} \\ \mathbf{D} & 0 \end{pmatrix} \begin{pmatrix} d\bar{\mathbf{v}} \\ d\bar{\mathbf{p}} \end{pmatrix} = \begin{pmatrix} \bar{\mathbf{r}}_m \\ \bar{\mathbf{r}}_c \end{pmatrix} \quad (3.21)$$

where $\bar{\mathbf{r}}_m$ and $\bar{\mathbf{r}}_c$ are the residual of the momentum equation and continuity equation.

$$\bar{\mathbf{r}}_m = \mathbf{F} - \frac{\mathbf{M}}{dt} (d\bar{\mathbf{v}}) - \mathbf{K}(\bar{\mathbf{v}}) \bar{\mathbf{v}} - \mu \mathbf{L} \bar{\mathbf{v}} - \mathbf{G} \bar{\mathbf{p}} \quad (3.22)$$

$$\bar{\mathbf{r}}_c = -\mathbf{D} \bar{\mathbf{v}} \quad (3.23)$$

The application of the residual form is convenient for the implementation of a general Newton-Raphson procedure for solving nonlinear systems of equations. For the system presented herein, the nonlinearity of the system is exclusively present in the convection term. Computing the velocity obtained from the previous iteration and using the convective operator, Newton-Raphson's procedure coincides with a fixed-point method.

3.2.2 Time discretization

Equation (3.22) represents a discrete in space and continuous in time, approximation to the original system of partial differential equations. Due to the implicit nature of the incompressible Navier-Stokes equations, an implicit scheme is needed for the time discretization. Herein, an implicit Backward Euler time integration is chosen to replace the continuous time derivative with an approximation for the history of the dependent variables over a small portion of the problem time scale. Though, implicit integration method is more computationally expensive, it is desirable due to its increased stability and the consistent treatment of the pressure.

Writing the time derivative terms of the Eq. (3.22) on the left-hand side and the other in the right-hand side, it can be described as

$$\frac{\mathbf{M}}{\Delta t} \left(\frac{\mathbf{M}}{dt} (d\bar{\mathbf{v}}) \right) = -\bar{\mathbf{r}}_m + \mathbf{F} - \mathbf{K}(\bar{\mathbf{v}})\bar{\mathbf{v}} - \mu\mathbf{L}\bar{\mathbf{v}} - \mathbf{G}\bar{\mathbf{p}} \quad (3.24)$$

Applying the Backward Euler method to Eq.(3.24), the implicit method yields

$$\mathbf{M}\bar{\mathbf{v}}_{n+1}^i = \mathbf{M}\bar{\mathbf{v}}_n + \Delta t_n [-\bar{\mathbf{r}}_{m_{n+1}} + \mathbf{F}_{n+1} - \mathbf{K}(\bar{\mathbf{v}}_{n+1}^i)\bar{\mathbf{v}}_{n+1}^i - \mu\mathbf{L}\bar{\mathbf{v}}_{n+1}^i - \mathbf{G}\bar{\mathbf{p}}_{n+1}^i] \quad (3.25)$$

or in a form more suitable for computation

$$\left[\frac{1}{\Delta t_n} \mathbf{M} + \mathbf{K}(\bar{\mathbf{v}}_{n+1}^i) + \mu\mathbf{L} \right] \bar{\mathbf{v}}_{n+1}^i + \mathbf{G}\bar{\mathbf{p}}_{n+1}^i = \frac{1}{\Delta t_n} \mathbf{M}\bar{\mathbf{v}}_n - \bar{\mathbf{r}}_{m_{n+1}} + \mathbf{F}_{n+1} \quad (3.26)$$

With the discretization of the time derivative, the Eq (3.26) represents a set of nonlinear algebraic equations for the solution vector.

3.3 Model for the structure

Prior describing the formulation used for the structure, it is worth noting that this thesis restricts to membrane elements due to the nature of the problem of interest. Also, only triangular shapes elements will be considered.

3.3.1 Membrane element

The behaviour of the textile material used for manufacturing inflatable structures can be modelled by a membrane theory of shells. A membrane can be seen as a 2D shell element interacting in a 3D environment which has no flexural stiffness. They resist only tensile forces. Hence, membranes resist external forces by deforming and “finding” the best shape to resist such forces.

The finite element model of a membrane is based on the assumptions:

- No bending resistance
- Plane stress state ($\sigma_{33} = 0$)
- Sections keep planar and normal to the mid-plane of the membrane

3.3.1.1 Three Dimensional approach

Let's consider a set of points representing a membrane continuum in a 3D space. It is possible to describe the position of any arbitrary point inside this continuum as

$$\mathbf{x}(\xi, \eta, \zeta) = N_I(\xi, \eta)\mathbf{x}_I + \frac{t}{2}\zeta\mathbf{n} \quad (3.27)$$

where $\mathbf{x}_I = \{x_I, y_I, z_I\}^T$ represents the position vector of the I-th node in the Cartesian space; $N_I(\xi, \eta)$ the value of the shape function centred on node I on the point of local coordinates (ξ, η) ; \mathbf{n} represents the normal to the 3D plane and t is the membrane thickness.

The first term of the right-hand side in Eq. (3.27) contains a set of points representing the position of the mid-plane of the membrane, while the second term represents the position along the thickness.

The coordinate Jacobian J can be derived from 1.2 giving

$$J = \begin{pmatrix} \frac{\partial N_I}{\partial \xi} x_{11} & \frac{\partial N_I}{\partial \eta} x_{11} & \left(\frac{t}{2} \frac{\partial \zeta \mathbf{n}}{\partial \zeta}\right)_1 \\ \frac{\partial N_I}{\partial \xi} x_{21} & \frac{\partial N_I}{\partial \eta} x_{21} & \left(\frac{t}{2} \frac{\partial \zeta \mathbf{n}}{\partial \zeta}\right)_2 \\ \frac{\partial N_I}{\partial \xi} x_{31} & \frac{\partial N_I}{\partial \eta} x_{31} & \left(\frac{t}{2} \frac{\partial \zeta \mathbf{n}}{\partial \zeta}\right)_3 \end{pmatrix} \quad (3.28)$$

Taking into account the assumption on the membrane behaviour related to forces, which states that the normal is the same through the thickness ($\mathbf{n} = \mathbf{n}(\xi, \eta)$), the Jacobian matrix can be described as:

$$\mathbf{j} = \begin{pmatrix} \frac{\partial N_I}{\partial \xi} \mathbf{x}_{1I} + \left(\frac{t}{2} \frac{\partial \zeta \mathbf{n}}{\partial \zeta}\right)_1 & \frac{\partial N_I}{\partial \eta} \mathbf{x}_{1I} + \left(\frac{t}{2} \frac{\partial \zeta \mathbf{n}}{\partial \zeta}\right)_1 & \left(\frac{t}{2} \mathbf{n}\right)_1 \\ \frac{\partial N_I}{\partial \xi} \mathbf{x}_{2I} + \left(\frac{t}{2} \frac{\partial \zeta \mathbf{n}}{\partial \zeta}\right)_2 & \frac{\partial N_I}{\partial \eta} \mathbf{x}_{2I} + \left(\frac{t}{2} \frac{\partial \zeta \mathbf{n}}{\partial \zeta}\right)_2 & \left(\frac{t}{2} \mathbf{n}\right)_2 \\ \frac{\partial N_I}{\partial \xi} \mathbf{x}_{3I} + \left(\frac{t}{2} \frac{\partial \zeta \mathbf{n}}{\partial \zeta}\right)_3 & \frac{\partial N_I}{\partial \eta} \mathbf{x}_{3I} + \left(\frac{t}{2} \frac{\partial \zeta \mathbf{n}}{\partial \zeta}\right)_3 & \left(\frac{t}{2} \mathbf{n}\right)_3 \end{pmatrix} \quad (3.29)$$

$$\mathbf{J} = \begin{pmatrix} \frac{\partial N_I}{\partial \xi} \mathbf{X}_{1I} + \left(\frac{t}{2} \frac{\partial \zeta \mathbf{N}}{\partial \zeta}\right)_1 & \frac{\partial N_I}{\partial \eta} \mathbf{X}_{1I} + \left(\frac{t}{2} \frac{\partial \zeta \mathbf{N}}{\partial \zeta}\right)_1 & \left(\frac{t}{2} \mathbf{N}\right)_1 \\ \frac{\partial N_I}{\partial \xi} \mathbf{X}_{2I} + \left(\frac{t}{2} \frac{\partial \zeta \mathbf{N}}{\partial \zeta}\right)_2 & \frac{\partial N_I}{\partial \eta} \mathbf{X}_{2I} + \left(\frac{t}{2} \frac{\partial \zeta \mathbf{N}}{\partial \zeta}\right)_2 & \left(\frac{t}{2} \mathbf{N}\right)_2 \\ \frac{\partial N_I}{\partial \xi} \mathbf{X}_{3I} + \left(\frac{t}{2} \frac{\partial \zeta \mathbf{N}}{\partial \zeta}\right)_3 & \frac{\partial N_I}{\partial \eta} \mathbf{X}_{3I} + \left(\frac{t}{2} \frac{\partial \zeta \mathbf{N}}{\partial \zeta}\right)_3 & \left(\frac{t}{2} \mathbf{N}\right)_3 \end{pmatrix} \quad (3.30)$$

where \mathbf{J}_0 and \mathbf{j} represents de Jacobian matrices in the *current* and *reference* configuration respectively. In the same way, vectors designed with capital letters (\mathbf{X} , \mathbf{N}) correspond to the current configuration, while vectors designed with small letters (\mathbf{x} , \mathbf{n}) to the reference configuration.

On the other hand, assuming constant deformation over the thickness, the coordinate Jacobians can be calculated on the middle surface ($\zeta = 0$). This assumptions allows to simplify the problem by removing the dependence of the solution on the local derivatives of the normal at ξ and η .

Introducing the two vectors

$$\mathbf{g}_\xi^{3 \times 1} = \left\{ \frac{\partial \mathbf{N}_I(\xi, \eta)}{\partial \xi} \mathbf{x}_I \right\} \quad (3.31)$$

$$\mathbf{g}_\eta^{3 \times 1} = \left\{ \frac{\partial \mathbf{N}_I(\xi, \eta)}{\partial \eta} \mathbf{x}_I \right\} \quad (3.32)$$

which are tangent to the membrane's mid-plane, the normal can be calculated as

$$\mathbf{n}^{3 \times 1} = \frac{\mathbf{g}_\xi \times \mathbf{g}_\eta}{\|\mathbf{g}_\xi \times \mathbf{g}_\eta\|} \quad (3.33)$$

And express the Jacobian gradient as

$$\mathbf{J}^{3 \times 3} = \begin{pmatrix} \mathbf{g}_\xi & \mathbf{g}_\eta & \frac{t}{2} \mathbf{n} \end{pmatrix} \quad (3.34)$$

The assumption of plane stress ($\sigma_{33} = 0$) provides an extra condition which relates the thickness variation with the in-plane strain. However, it is possible to calculate the Jacobian keeping constant the thickness of the membrane if an appropriate form for the elasticity tensor is chosen (see Vitaliani et al [22]). The elasticity tensor for membranes initially lying in the XY plane is represented as

$$\mathbf{D}_{\text{iso}} = \frac{E}{1-\nu^2} \begin{pmatrix} 1 & \nu & 0 & 0 & 0 & 0 \\ \nu & 1 & 0 & 0 & 0 & 0 \\ 0 & 0 & \frac{1-\nu}{2} & 0 & 0 & 0 \\ 0 & 0 & 0 & 0 & 0 & 0 \\ 0 & 0 & 0 & 0 & 0 & 0 \\ 0 & 0 & 0 & 0 & 0 & 0 \end{pmatrix} \quad (3.35)$$

which can effectively be used for the calculation assuming a constant thickness, since any strain in the Z direction does not take relevance, while the other terms match the corresponding plane stress isotropic elasticity tensor

$$\mathbf{D}^{2D} = \frac{E}{1-\nu^2} \begin{pmatrix} 1 & \nu & 0 \\ \nu & 1 & 0 \\ 0 & 0 & \frac{1-\nu}{2} \end{pmatrix} \quad (3.36)$$

When reference configuration for the membrane and the XY plane do not coincide, the thickness stretch does not coincide with the \mathbf{E}_{zz} Green Lagrange strain. In this case the same elasticity tensor is given in the tangent system of coordinates and needs to be brought back to the global coordinate system. This can be done by rotating (on each Gauss integration point) the elasticity tensor in Eq. (3.35) from tangent coordinate system to the global coordinate system. Hence, the effective constant elastic modulus can be expressed

$$[\mathbf{D}^{\text{effective}}] = [\mathbf{T}]^T [\mathbf{D}] [\mathbf{T}] \quad (3.37)$$

where \mathbf{T} represents the rotation matrix, see Ricardo Rossi [23].

With the definition of the constitutive law, the membrane can be considered as a normal 3D total Lagrangian element. Thereby, it can be introduced using standard techniques for total Lagrangian elements.

3.3.2 Spatial discretization

The strong form of the structural mechanics boundary value problem may be written as

$$\rho \cdot \ddot{\mathbf{u}} - \nabla \boldsymbol{\sigma} - \rho \mathbf{f} = 0 \quad (3.38)$$

$$\mathbf{u} = \bar{\mathbf{u}} \quad \text{on } \Gamma_d \quad (3.39)$$

$$\boldsymbol{\sigma} \cdot \mathbf{n} = \mathbf{g} \quad \text{on } \Gamma_\sigma \quad (3.40)$$

As it is commonly used for structure problems, a virtual work is used in Eq. (3.38) to obtain the weak form of the structural domain.

The membrane structure may suffer of large displacements from the first to the final position. From numerical point of view, this behaviour can lead the membrane system to an ill-conditioned or even of singularity of the tangent stiffness matrix. To avoid these problems, a linear damping term is included for the purposes in getting initially stable solutions. Only first time derivatives of time will occur if the inertial loading based on $\ddot{\mathbf{u}}$ is ignored. Thereby, the weak form, using a virtual work expression for the membrane may be written by

$$- \int_{\Omega^s} t \delta \mathbf{E} : \mathbf{S} \, d\Omega^s = \int_{\Omega^s} \boldsymbol{\omega} \cdot \rho (\ddot{\mathbf{u}} - \mathbf{f}) \, d\Omega^s + \int_{\Omega^s} \boldsymbol{\omega} \cdot c_0 \dot{\mathbf{u}} \, d\Omega^s - \int_{(\Gamma^s)_h} \boldsymbol{\omega} \cdot \mathbf{h} \, d\Gamma^s \quad (3.41)$$

where the left-hand side represents the internal work, and the right-hand side the external work. Also, $\delta \mathbf{E}$ is the variation of the Green-Lagrange strain tensor referred to the virtual strain, \mathbf{S} is the second Piola-Kirchhoff stress tensor, which is symmetric and work-conjugate to \mathbf{E} , t is the membrane thickness, $\boldsymbol{\omega}$ is a virtual displacement, c_0 is a linear damping coefficient in the reference configuration, and \mathbf{h} is the external traction vector applied on the subset $(\Gamma^s)_h$, where traction values are specified of the total boundary Γ^s .

Eq. (3.41) may be written in component form as

$$\int_{\Omega^s} \omega_i \cdot \rho(\ddot{u}_i - f_i) d\Omega^s + \int_{\Omega^s} \omega_i \cdot c_o \dot{u}_i d\Omega^s + \int_{\Omega^s} t \delta E_{IJ} S_{IJ} d\Omega^s - \int_{(\Gamma^s)_h} \omega_i \cdot h_i d\Gamma^s \quad (3.42)$$

Using the definition of the Cauchy-Green deformation tensor

$$\mathbf{C} = \mathbf{F}^T \mathbf{F} = \mathbf{J}_o^{-T} \mathbf{J}^T \mathbf{J} \mathbf{J}_o^{-1} = \mathbf{G}^T \mathbf{g} \mathbf{G} \quad (3.43)$$

Where \mathbf{F} is the deformation gradient

$$\mathbf{F} = \frac{\partial \mathbf{x}}{\partial \mathbf{x}_o} \quad (3.44)$$

and \mathbf{G} is used to denote the invers of \mathbf{J} . In component form the Cauchy-Green deformation tensor is written as

$$\mathbf{C} = G_{II} g_{ij} G_{JJ} \quad \text{for } i, j = 1, 2 \text{ and } I, J = 1, 2 \quad (3.45)$$

where

$$G_{11} = \frac{1}{J_{11}} ; G_{22} = \frac{1}{J_{22}} ; G_{12} = \frac{1}{J_{12}} ; G_{22} = 0 \quad (3.46)$$

The integrant of the internal work in Eq. (3.42) may be written as

$$\delta C_{ij} S_{IJ} = G_{II} \delta g_{ij} G_{JJ} S_{IJ} = \delta g_{ij} s_{ij} \quad (3.47)$$

Where the stress like variable s_{ij} is defined by

$$s_{ij} = G_{II} G_{JJ} S_{IJ} \quad (3.48)$$

or in matrix form

$$\mathbf{s} = \mathbf{Q}^T \mathbf{S} \quad (3.49)$$

in which

$$\mathbf{Q}_{ab} \equiv \mathbf{G}_{ij} \mathbf{G}_{jj} \quad (3.50)$$

where the index map is performed according to (Table 3-1), yielding the result

$$\mathbf{Q} = \begin{bmatrix} \mathbf{G}_{11}^2 & 0 & 0 \\ \mathbf{G}_{12}^2 & \mathbf{G}_{22}^2 & \mathbf{G}_{12}\mathbf{G}_{22} \\ 2\mathbf{G}_{11}\mathbf{G}_{12} & 0 & \mathbf{G}_{11}\mathbf{G}_{22} \end{bmatrix} \quad (3.51)$$

Table 3-1. Index map for \mathbf{Q} array

Indices	Values
a	1 2 3
I,J	1,1 2,2 1,2 & 2,1
b	1 2 3
i, j	1,1 2,2 1,2 & 2,1

With the assumption of taken the thickness constant over each element, the results for the stresses are constant, since the deformation tensor is also constant over each element and, thus, the surface integral for the first term leads to the simple expression

$$\int_{\Omega^s} t \delta \mathbf{E}_{IJ} \mathbf{S}_{IJ} d\Omega^s = \int_{\Omega^s} \frac{t}{2} \delta \mathbf{C}_{IJ} \mathbf{S}_{IJ} d\Omega^s = \int_{\Omega^s} \frac{t}{2} \delta g_{ij} \mathbf{S}_{ij} d\Omega^s = \frac{t}{2} \delta g_{ij} \mathbf{S}_{ij} A \quad (3.52)$$

where A is the reference area for the element.

In addition, the strain-displacement matrix for the variation of \mathbf{E} , $\delta \mathbf{E} = \mathbf{Q} \mathbf{b} \delta \tilde{\mathbf{x}}$, may be described as (see E. Oñate and Bern Kröplin [24])

$$\mathbf{B} = \mathbf{Q} \mathbf{b} \quad (3.53)$$

where \mathbf{b} is the strain-displacement matrix

$$\mathbf{b} = \begin{bmatrix} -(\Delta \tilde{\mathbf{x}}^{21})^T & (\Delta \tilde{\mathbf{x}}^{21})^T & 0 \\ -(\Delta \tilde{\mathbf{x}}^{31})^T & 0 & (\Delta \tilde{\mathbf{x}}^{31})^T \\ -(\Delta \tilde{\mathbf{x}}^{21} + \Delta \tilde{\mathbf{x}}^{31})^T & (\Delta \tilde{\mathbf{x}}^{31})^T & (\Delta \tilde{\mathbf{x}}^{21})^T \end{bmatrix}_{3 \times 9} \quad (3.54)$$

in which

$$\Delta \tilde{\mathbf{x}}^{ij} = \tilde{\mathbf{x}}^i - \tilde{\mathbf{x}}^j \quad (3.55)$$

The residual form for each element may be written as

$$\begin{Bmatrix} \mathbf{R}^1 \\ \mathbf{R}^2 \\ \mathbf{R}^3 \end{Bmatrix} = \begin{Bmatrix} \mathbf{f}^1 \\ \mathbf{f}^2 \\ \mathbf{f}^3 \end{Bmatrix} - [\mathbf{M}_e] \begin{Bmatrix} \tilde{\mathbf{u}}^1 \\ \tilde{\mathbf{u}}^2 \\ \tilde{\mathbf{u}}^3 \end{Bmatrix} - [\mathbf{C}_e] \begin{Bmatrix} \dot{\tilde{\mathbf{u}}}^1 \\ \dot{\tilde{\mathbf{u}}}^2 \\ \dot{\tilde{\mathbf{u}}}^3 \end{Bmatrix} - t\mathbf{A}[\mathbf{B}]^T \quad (3.56)$$

where $[\mathbf{M}_e]$ and $[\mathbf{C}_e]$ are the element mass and damping matrices given by

$$[\mathbf{M}_e] = \begin{bmatrix} M^{11} & M^{12} & M^{13} \\ M^{21} & M^{22} & M^{23} \\ M^{31} & M^{32} & M^{33} \end{bmatrix} \quad ; \quad [\mathbf{C}_e] = \begin{bmatrix} C^{11} & C^{12} & C^{13} \\ C^{21} & C^{22} & C^{23} \\ C^{31} & C^{32} & C^{33} \end{bmatrix} \quad (3.57)$$

with

$$\begin{aligned} \mathbf{M}^{\alpha\beta} &= \int_{\Omega^s} \rho \, t \, \xi_\alpha \, \xi_\beta \, d\Omega^s \, \mathbf{I} \\ \mathbf{C}^{\alpha\beta} &= \int_{\Omega^s} c_o \, t \, \xi_\alpha \, \xi_\beta \, d\Omega^s \, \mathbf{I} \end{aligned} \quad (3.58)$$

For membranes subjected to internal pressure, the finite element nodal forces must be computed based on the *deformed* current configuration. Thereby, the nodal forces must be computed for each triangle element as

$$\tilde{\omega}^{\alpha,T} \mathbf{f}^\alpha = \tilde{\omega}^{\alpha,T} \int_{\Omega^s} \xi_\alpha \, (p \, \mathbf{n}) \, d\Omega^s \quad (3.59)$$

Assuming a triangular element and a constant pressure over the element, the normal vector \mathbf{n} is also constant, the integral term of the nodal forces yields

$$\mathbf{f}^\alpha = \frac{1}{3} p_e \, \mathbf{n} \, A_e \quad (3.60)$$

where p_e is the constant pressure over the element.

Finally, the weak form for the implementation of the Finite Element Method can be described as

$$\mathbf{R}_n^\alpha = \mathbf{f}_n^\alpha - \sum_e \mathbf{M}_e^{\alpha\beta} \ddot{\mathbf{u}}_n^\beta - \sum_e \mathbf{C}_e^{\alpha\beta} \dot{\mathbf{u}}_n^\beta - \sum_e (\mathbf{t}_e \mathbf{A}_e \mathbf{B}_e^{\alpha,T} \mathbf{S}_e)_n \quad (3.61)$$

where

$$\begin{aligned} \mathbf{M}_e^{\alpha\beta} &= \int_{\Omega^s} \rho \, t \, \xi_\alpha \, \xi_\beta \, d\Omega^s \, \mathbf{I} \\ \mathbf{C}_e^{\alpha\beta} &= \int_{\Omega^s} c_o \, t \, \xi_\alpha \, \xi_\beta \, d\Omega^s \, \mathbf{I} \\ \mathbf{f}_e^\alpha &= \frac{1}{3} p_e \, \mathbf{n} \, \mathbf{A}_e \end{aligned} \quad (3.62)$$

3.3.3 Time discretization

In the same manner as the fluid domain, an implicit method for the time discretization of the structure is used. Hence, an iterative solution scheme at each time step is necessary to solve a sequence of linear, algebraic problem. Herein, it is only presented the results for the St. Venant-Kirchhoff material model and the normal internal pressure. Thereby, the implicit Newmark method may be written as

$$\begin{aligned} \mathbf{u}_n &= \mathbf{u}_{n-1} + \Delta t_n \dot{\mathbf{u}}_{n-1} + \left(\frac{1}{2} - \beta\right) \Delta t_n^2 \ddot{\mathbf{u}}_{n-1} + \beta \Delta t_n^2 \ddot{\mathbf{u}}_n \\ \dot{\mathbf{u}}_n &= \dot{\mathbf{u}}_{n-1} + (1 - \gamma) \Delta t_n \ddot{\mathbf{u}}_{n-1} + \gamma \Delta t_n \ddot{\mathbf{u}}_n \end{aligned} \quad (3.63)$$

Using the implicit Newmark method (Eq.(3.63)) to the Eq. (3.61) a iterative Newton Raphson Method must be used to solve the system. In this process, the nonlinear residual equations are linearized about a given set of nodal positions $\tilde{\mathbf{x}}_n^k$ corresponding to known values at some iteration stage k . The result is written as

$$\mathbf{R}_n^{k+1} \approx \mathbf{R}_n^k + \left. \frac{\partial \mathbf{R}_n}{\partial \tilde{\mathbf{u}}} \right|^k d\tilde{\mathbf{u}}_n^k = 0 \quad (3.64)$$

defining the tangent (jacobian) matrix \mathbf{A} as

$$\mathbf{A} = - \frac{\partial \mathbf{R}}{\partial \tilde{\mathbf{u}}} \quad (3.65)$$

the Eq. (3.64), as a set of linear algebraic equations to be solved at each iteration yields

$$\mathbf{A}_n^k d\tilde{\mathbf{u}}_n^k = \mathbf{R}_n^k \quad (3.66)$$

The solution may be updated using

$$\mathbf{u}_n^{k+1} = \mathbf{u}_n^k + d\tilde{\mathbf{u}}_n^k \quad (3.67)$$

For transients applications the use of the specified time stepping algorithm is required to compute the tangent matrix. Hence, the computation for the transient term is described as

$$\mathbf{A} = -\frac{\partial \mathbf{R}}{\partial \tilde{\mathbf{u}}} - \frac{\partial \mathbf{R}}{\partial \dot{\tilde{\mathbf{u}}}} \frac{\partial \dot{\tilde{\mathbf{u}}}}{\partial \tilde{\mathbf{u}}} - \frac{\partial \mathbf{R}}{\partial \ddot{\tilde{\mathbf{u}}}} \frac{\partial \ddot{\tilde{\mathbf{u}}}}{\partial \tilde{\mathbf{u}}} \quad (3.68)$$

or

$$\mathbf{A} = c_1 \mathbf{K} + c_2 \mathbf{C} + c_3 \mathbf{M}$$

where the c_i result from any differentiation of the nodal vectors with respect to the solution vector. For the Newmark method the result from Eq. (3.61) gives $c_1 = 1$ and from Eq. (3.63) it is obtained

$$\frac{\partial \tilde{\mathbf{u}}}{\partial \ddot{\tilde{\mathbf{u}}}} = \beta \Delta t_n^2 \mathbf{I} \quad ; \quad \frac{\partial \dot{\tilde{\mathbf{u}}}}{\partial \ddot{\tilde{\mathbf{u}}}} = \beta \Delta t_n^2 \mathbf{I} \quad (3.69)$$

Hence,

$$c_2 = \frac{\gamma}{\beta \Delta t_n} \quad ; \quad c_3 = \frac{1}{\beta \Delta t_n^2} \quad (3.70)$$

3.3.3.1 Membrane tangent matrix

To compute the element stiffness matrix it is necessary to determine the change in stress due to an incremental change in the motion. In accordance the St. Venant-Kirchhoff model it is obtained

$$d\mathbf{S}_e = \mathcal{D}d\mathbf{E}_e \quad (3.71)$$

where

$$d\mathbf{E}_e = \mathbf{Q}_e \mathbf{b}_e d\tilde{\mathbf{x}}_e \quad (3.72)$$

The element stiffness matrix is given by

$$\mathbf{K}_e = \left(t\mathbf{A}\mathbf{B}_n^t \mathcal{D}_n \mathbf{B}_n + \mathbf{K}_g \right)_e \quad (3.73)$$

where \mathbf{K}_g is a geometric stiffness may be written as

$$\mathbf{K}_g = t_e A_e \begin{bmatrix} (s_{11} + 2s_{12} + s_{22})\mathbf{I} & -(s_{11} + s_{12})\mathbf{I} & -(s_{22} + s_{12})\mathbf{I} \\ -(s_{11} + s_{12})\mathbf{I} & s_{11}\mathbf{I} & s_{12}\mathbf{I} \\ -(s_{22} + s_{12})\mathbf{I} & s_{12}\mathbf{I} & s_{22}\mathbf{I} \end{bmatrix} \quad (3.74)$$

3.4 Coupling scheme

The coupling scheme used in Kratos framework for FSI problems in light-weight structures is an embedded approach which treats the fluid and the structure in a partitioned way. The formulation for fluid and structure presented above must be completed with a coupling strategy.

The coupling between the Eulerian and Lagrangian domains consists in finding the positions of the Lagrangian image within the fixed Eulerian mesh, which splits the Eulerian domain into real and fictitious parts. In addition to the interchange of boundary conditions between the Lagrangian and Eulerian parts. The interchange of boundary condition is prescribed as:

- The velocity of the Lagrangian domain boundary provides an "interface" Dirichlet condition for the fluid.
- The fluid pressure provides a Neumann condition for the solid surface.

3.4.1 Boundary conditions

The interaction between the sub-domains must be ensured by imposing constraints at the interface. These constraints are imposed in the Dirichlet and the Neumann boundaries.

3.4.1.1 Dirichlet coupling

In Dirichlet boundary conditions, the imposed constraint must ensure, since the fluid is viscous, a continuity of all the velocity components.

$$\mathbf{v}_{\Gamma_I} = \dot{\mathbf{u}}_{\Gamma_L} \quad (3.75)$$

being \mathbf{v}_{Γ_E} and $\dot{\mathbf{u}}_{\Gamma_L}$, the velocity of the Eulerian and Lagrangian domain at the interface Γ_I , respectively.

The Lagrangian image Γ_I not necessarily intersects the Eulerian mesh at the nodes. Hence, the interface Dirichlet boundary conditions is applied by minimizing the difference between the velocity Lagrangian image and the velocity field of the Eulerian fluid. See P.B. Ryzhakov and A. Jarauta [25], for an implementation of this strategy.

3.4.1.2 Neumann coupling

In Neumann boundary conditions the imposed constraint must satisfy the continuity of the normal component of the stress $\boldsymbol{\sigma}$. The approximation of considering only the continuity of normal stresses and no continuity in tangential stresses is commonly accepted for the fluids with low viscosity such as the case of the air. This approximation ensures the conservation of momentum at the interface:

$$(\boldsymbol{\sigma} \cdot \mathbf{n})_{T_E} p_{T_L} \quad (3.76)$$

Considering that the Lagrangian surface is entirely embedded into the Eulerian mesh, the pressure from the Eulerian mesh can be simply projected onto Lagrangian nodes using direct interpolation. The pressure value at a Lagrangian node i encountered inside the Eulerian element ABC, see , is computed as, see again P.B. Ryzhakov and A. Jarauta [25] for an example of the implementation of this technique:

$$p_E^i = N_A(x_i)p_A + N_B(x_i)p_B + N_C(x_i)p_C \quad (3.77)$$

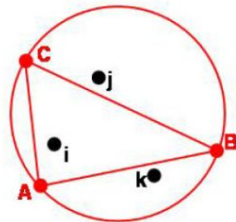


Figure 3.3. Interpolation technique for Neumann boundary conditions coupling

3.5 Solution Algorithm

At this point, the required arguments for describing the embedded Eulerian-Lagrangian (fluid-structure) formulation have been described. Following, a pseudo-code of the coupled fluid-structure problem is presented.

Let us consider that the velocity $\bar{\mathbf{v}}$ and pressure $\bar{\mathbf{p}}$ at time t_n is known in both domains, fluid Ω^f and structure \mathbf{B} . Table 3-2 describes the algorithm implemented to find the velocity and pressure fields at t_{n+1} :

Table 3-2. Solution algorithm of the coupled fluid-structure problem.

-
1. **Solve the structure problem**
 - Output: new position of the Lagrangian domain, $\bar{\mathbf{u}}_{n+1}^s$ and $\bar{\mathbf{v}}_{n+1}^s$ in \mathbf{B} .
 2. **Identify the position of the Lagrangian Domain within the Eulerian one**
 - Output: Lagrangian image $\partial\mathbf{B}$.
 3. **Represent structural velocity on the fixed mesh**
 - Solve the minimization problem at the interface boundary conditions.
 - Apply interface Dirichlet boundary conditions.
 - Output: $\bar{\mathbf{v}}_{n+1}^{\partial\mathbf{B}}$ and $\bar{\mathbf{p}}_{n+1}^{\partial\mathbf{B}}$ in the interface elements
 4. **Solve the fluid problem**
 - Output: $\bar{\mathbf{v}}_{n+1}^f$ and $\bar{\mathbf{p}}_{n+1}^f$ in Ω^f
 5. **Map fluid pressure onto structure surface**
 - Projection pressure from $\bar{\mathbf{p}}_{n+1}^{\partial\mathbf{B}}$ at Lagrangian image onto \mathbf{B} , as a Neumann boundary condition, compute the corresponding force term for the momentum equation of the structure.
 6. **Repeat steps 1 to 5**
 - Iterative solution for a strong two-way coupling problem. Iterative process is carried out until convergence in terms of the displacements of the Lagrangian domain is achieved.
 7. **Go to next time step**
-

References

1. Bandringa Henry, "Immersed boundary methods", *Master Thesis in Applied Mathematics*, University of Groningen, August 2010.
2. Baumgartner D. and Wolf J., "Interface treatment and solution procedures in fsi simulations using an ale or embedded strategy," *Master's thesis, Technical University of Munich, TUM*, 2013.
3. C.A. Felippa and K.C. Park, "Synthesis Tools for Structural Dynamics and Partitioned Analysis of Coupled Systems", class notes ASEN 5509, Dpt. Aerospace Engineering Science, University of Colorado, Boulder, USA, 2014.
4. Eugenio Oñate, Pere-Andreu Ubach Robert L. Taylor, "Textil Composites and Inflatable Structures," in *Textil Composites and Inflatable Structures.*: Springer, 2005, pp. 47-68.
5. J.N. Reddy and D.K. Gartling, *The Finite Element Methods in Heat Transfer and Fluid Dynamics*, Second Edition ed. Florida, USA: CRC Press, 2000.
6. Lazzari M., Saetta A.V. Vitalini R.V., "Non-linear dynamic analysis of cable suspended structures subjected to wind actions," *Journal of Computer and Structures*, no. 79, pp. 233-251, 2001.
7. P.B. Ryzhakov and A. Jarauta, "An embedded approach for immiscible multi-fluid problems," *Internal Journal for Numerical Methods in Fluids*, no. 00, pp. 1-33, 2015.
8. Riccardo Rossi, "Light-weight structures. Numerical Analysis and Coupling issues," Università di Bologna, PhD dissertation January, 2006.
9. van Kreveld M., Overmars M., and Schwarzkopf O. de Berg M., "Computational Geometry Algorithms and applications," *Springer-Verlag*, 1997.
10. Yong J. H., Sun J. G., Gu H. J., and Paul J. C. Yang S., "A cell-based algorithm for evaluating directional distances in GIS," *International Journal of Geographical Information Science*, no. 24(4), pp. 577-590, 2010.
11. Yuri Bazilevs, Kenji Takizawa, Tayfun E. Tezduyar, *Computational Fluid-Structure Interaction. Methods and Applications.* A John Wiley & Sons, Ltd., 2013.

Chapter 4:

Implementation Issues

Dynamic analysis of structural (membrane) and fluid dynamic problems requires several time steps to reach stable solution. Hence, an immediate application of a strong two-way coupling solution for the first time step of the problem typically leads to a divergent solution.

In order to obtain a robust and efficient implementation, stable fluid and structure solution must be guaranteed prior to the application of a strong two-way coupling. This is achieved by the inclusion of several preliminary stages. A scheme of the overall solution is summarized in Table 4-1:

Table 4-1. Scheme of the overall solution strategy in the solution of a two-way coupling interaction

1. Start fluid solver
<ul style="list-style-type: none"> • 100 Stokes steps are performed to obtain initial divergence-free solution in the fluid domain.
2. Uncoupled Fluid and Structure solution
<ul style="list-style-type: none"> • Fluid and structure are solved separately without performing the coupled fluid-structure problem. This is done until the both domains reach static equilibrium solution.
3. One-way coupling interaction
<ul style="list-style-type: none"> • Fluid and structure are solved using one-way coupling interaction. Fluid pressure is mapped onto the structure domain and used as Neumann boundary condition.
4. Two-way coupling interaction
<ul style="list-style-type: none"> • Fluid and structure are solved using a strong two-way coupling interaction. Iterative solution in the coupling process is carried out.

Following, a deeper explanation of the different stages for the overall solution is presented.

4.1 Overall solution strategy

In order to obtain a preliminary divergence-free flow pattern in the whole fluid domain, few steps of the fluid simulation with a very small time-step are solved considering Stokes problem and a fixed rigid structure. This stage allows obtaining a preliminary solution on the fluid domain.

Once the preliminary solution of the fluid is obtained, the uncoupled fluid-structure solution is performed. In each time-step of this stage, identification of the position of the Lagrangian domain within fixed fluid mesh is carried out an embedded approach is carried out, but no coupling boundary conditions take place. The uncoupled fluid-structure solution must be solved until both, fluid and structure domains reach a stable static solution. Observing the structural dynamic response due to self-weight and a constant internal pressure represented in Figure 4.1, one can appreciate that if the coupling was carried out at the beginning of the solution, the coupled problem could typically lead to a divergent solution, since large variation of displacements (and velocity) in the structure domains are produced.

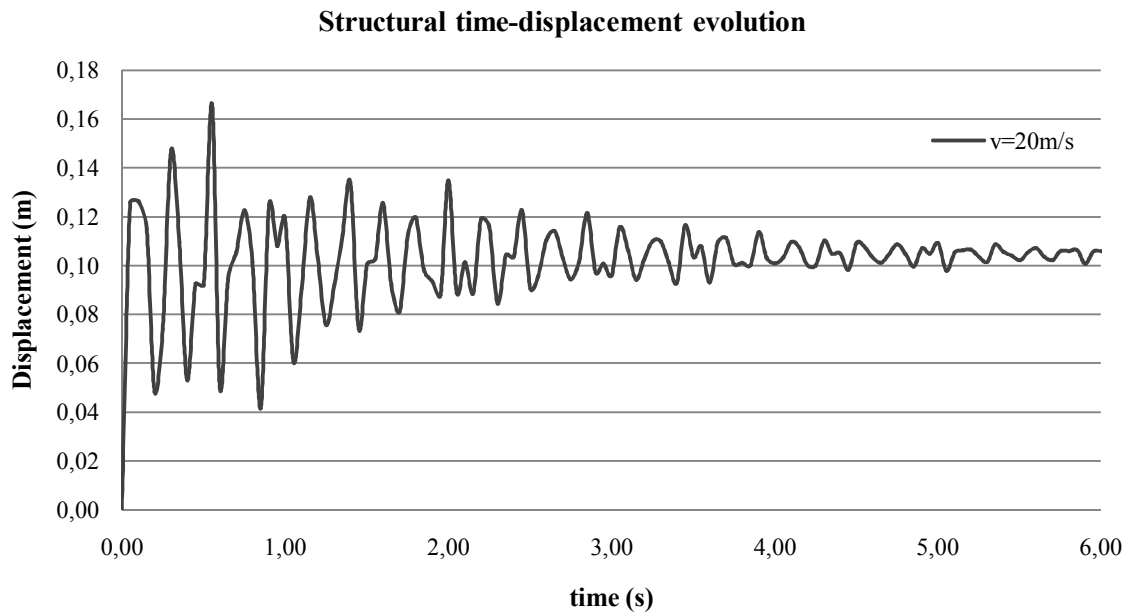


Figure 4.1. Structural dynamic response due to self-weight and constant internal pressure

When stable solution in both domains is obtained, the coupling process takes place. First, a one-way coupling is applied to obtain initial approximation of the coupling solution.

Afterwards, a strong two-way coupling is applied where properties –velocity and pressure – between both domain are interchanged thanks the solution of iterative coupling boundary problem. The interaction is carried out in two directions; fluid solution is transferred to the structure and inversely.

At the instant in which the fluid pressure is applied to the flexible structure for the first time, large displacements and, consequently large velocities in the structure domain arise. Figure 4.2 depicts the structural velocity response in an arbitrary node at time of the coupling solution for an inlet fluid velocity of 35m/s.

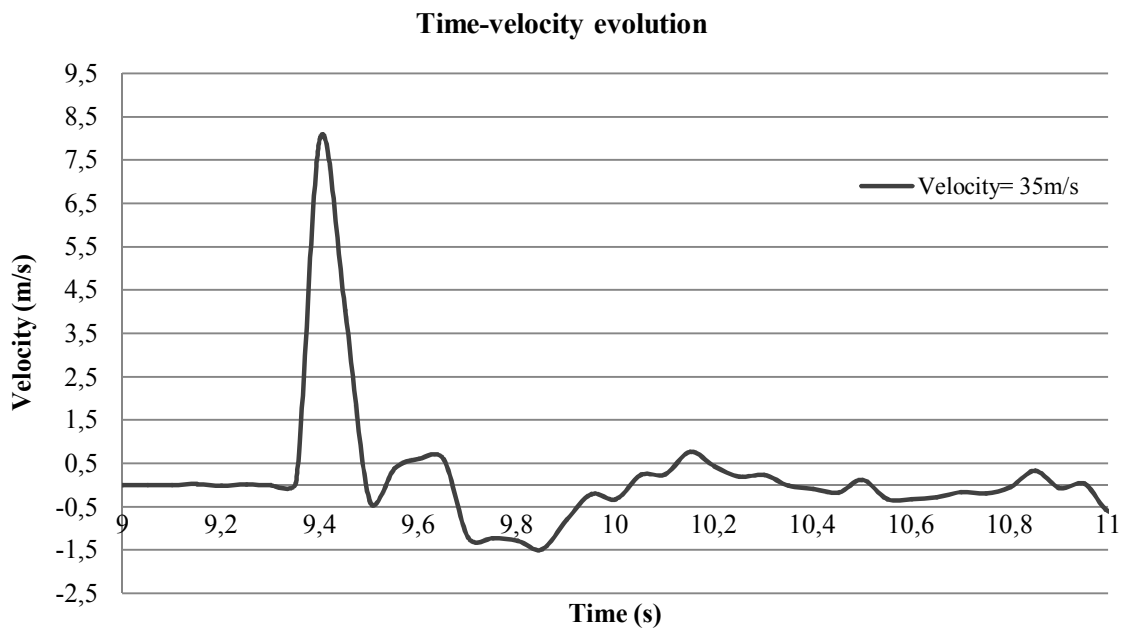


Figure 4.2. Structural velocity response due to an inlet fluid velocity of 35m/s

It is worth noting that these instantaneous large velocities are a numerical artefact. Hence, it is obvious that a premature application of the strong two-way coupling solution could present a divergent solution (large velocities in structure domain would disturb fluid velocities when minimizing Dirichlet coupling boundaries conditions).

Finally, two-way coupling is applied in order to obtain the final solution of the problem.

4.1.1 Optimal time duration of preliminary stages

Different stages on the solution strategy have been presented in the previous section of the chapter. Identification of the time when the analysis should change from one stage to the next one has an important impact in the solution of the simulation. As previously commented, one must ensure that structure reaches a static equilibrium prior to apply the necessary and final conditions of the problem in order to avoid divergent solutions. In this work an algorithm for automatic identification of the necessary time for each stage has been implemented in order to reduce computational cost. Otherwise, the user would have to estimate these times in a “trial-and-error” way, leading to the possible divergent solution of the model or computing unnecessary time spent in the different stages.

In the following, we present two different codes implemented. First one, for the identification of the necessary time in the uncoupled fluid and structure solution (2)⁶. The other is implemented to identify the time necessary in the one-way coupling strategy (3).

4.1.1.1 Identification of the uncoupled solution time

The first algorithm takes into account the relative error of the current total average displacement, and the average displacement of the last three time steps. Table 4-2 shows a pseudo-code of the algorithm implementation. It was detected that fluid domain needs few steps for reaching the equilibrium solution due to the previous solution of the Stokes steps carried out in stage (1). Hence, the idea consists of determining the static equilibrium solution of the structure by analysing the displacements along the time. Small variability in the displacement guarantees the static solution. Observing again Figure 4.1, one can see that after four seconds the structure tends to a static solution, since small variability of displacement is detected.

In order to avoid unexpected time identification due to small time step (Δt), the requirement precise error has been determined in function of Δt .

⁶ The number in parenthesis indicates the stage number represented in Table 4-1. Scheme of the overall solution strategy in the solution of a two-way coupling interaction

Table 4-2. Pseudo-code of the implementation in the algorithm for the uncoupled time solution identification

Uncoupled simulation:

For each new time step n+1

 Compute structural solver

 Compute fluid solver

if structure did not converge in previous time step

for all the nodes of the Lagrangian image

 get the value of the displacement in the previous three steps and the current step

 calculate norm of the displacements in the 4 steps taken into account

$$\text{displacement error } (\Delta t) = \text{abs} \left(\frac{\bar{u}_{t_i} - \frac{\bar{u}_{t_i} + \bar{u}_{t_{i-1}} + \bar{u}_{t_{i-2}} + \bar{u}_{t_{i-3}}}{4}}{\bar{u}_{t_i}} \right)$$

if displacement error is bigger than the tolerance

 structure does not converge

elif displacement error is less than the tolerance

 structure do converge

 go to uncoupled fluid and structure solve stage

 next time step

time= uncoupled_time

Similarly, in the second approach, a relative error has been estimated. However, at the coupled solution, velocity is the property value that takes place in the embedded coupling strategy. Hence, the total average velocity has been taken into account instead of the displacement. The algorithm implementation for the identification of the one-way coupling time is presented below:

Table 4-3. Pseudo-code of the implementation in the algorithm for the one-way coupling time identification

One-way coupling simulation:

For each new time step n+1

 Compute One way coupling interaction solver

if velocity did not converge in previous time step

for all the nodes of the Lagrangian image

 get the value of the velocity in the previous three steps and the current step

 calculate norm of the velocity in the 4 steps taken into account

$$\text{velocity error} = \text{abs} \left(\frac{\bar{v}_{t_i} - \frac{\bar{v}_{t_i} + \bar{v}_{t_{i-1}} + \bar{v}_{t_{i-2}} + \bar{v}_{t_{i-3}}}{4}}{\bar{v}_{t_i}} \right)$$

if velocity error is bigger than the tolerance
 velocity does not converge
elif velocity error is less than the tolerance
 velocity do converge
 go to two-way coupling interaction stage
 next time step

time=OWC_time

4.1.2 Incremental pressure application

It is worth noting that high inlet velocities lead to high pressures on the boundary surfaces. The immediate application of these pressures at the beginning of the coupling process may lead to a divergent solution of the structure. In order to avoid this numerical error, an incremental application of pressure has been implemented. The pressure field obtained in the fluid domain is mapped onto the structure. However, the pressure is applied in an incremental manner over the general time steps following a sinusoidal function. Table 4-4 shows the implemented algorithm for the incremental pressure application:

Table 4-4. Pseudo-code of the implementation of the algorithm for the incremental pressure technique

Performing incremental pressure

Starting incremental pressure

Structure solver

Fluid solver

Find Lagrangian image into the Fluid domain

for all the nodes in the interface boundary

 Full positive pressure: Get the solution of the fluid pressure

 Multiply the pressure value by a low number in the sinusoidal equation

 Initial positive pressure: Set the reduced pressure value onto the structure

go to next step (Solving the incremental pressure)

Solving the incremental pressure

```

Structure solver
Fluid solver
Find Lagrangian image into the Fluid domain
for all the nodes in the interface boundary
    Get the pressure applied in the previous step (p_prev)
    Set the new positive pressure onto the structure surface by a sinusoidal equation
next time step
go to One way coupling interaction

```

Figure 4.3 depicts an example of the application of the incremental pressure technique. The pressure corresponds to an inlet velocity of 10m/s.

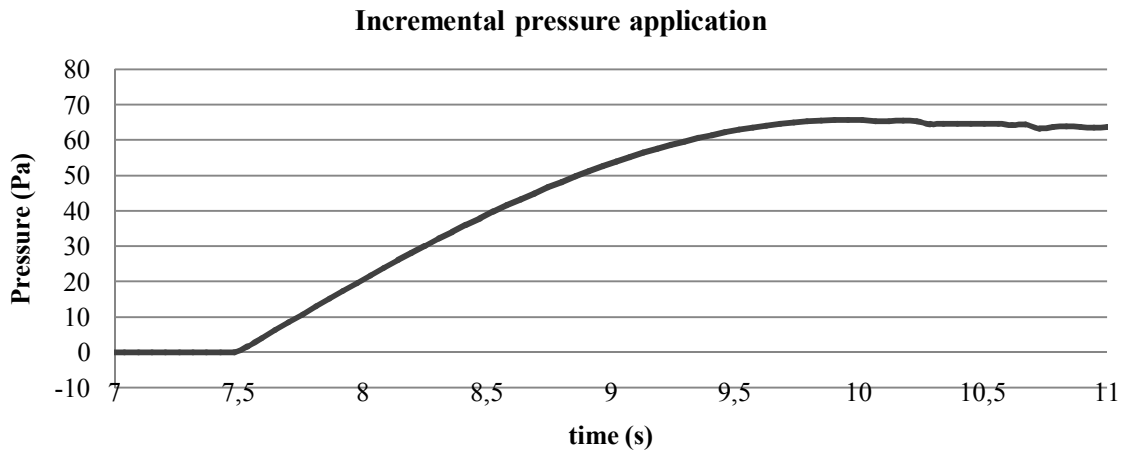


Figure 4.3. Application of the incremental pressure technique for an inlet velocity of 10m/s

4.2 Final comments

Two-way coupling is the most realistic way to represent the behaviour of the fluid-structure interaction problems, since the response of a domain involves the solution of the other domain, and reversely. Hence, for FSI problems involving large solid deformation, as the example of thin light-weight structures, two-way coupling solutions seem to be the most realistic simulation. Furthermore, it was discovered that for large air velocities, one-way coupling process leads to spurious or divergent solutions.

Strong two-way coupling solution needs preliminary stages in order to obtain a robust and efficient implementation. Automatic identifications of the time of preliminary stages have been successfully implemented.

As a consequence, the optimal time duration of preliminary stages (`uncoupled_time` and `OWC_time`) are determined.

An example of the different stages of the coupled simulation taking into account the above-explained methodology is shown in Figure 4.4.

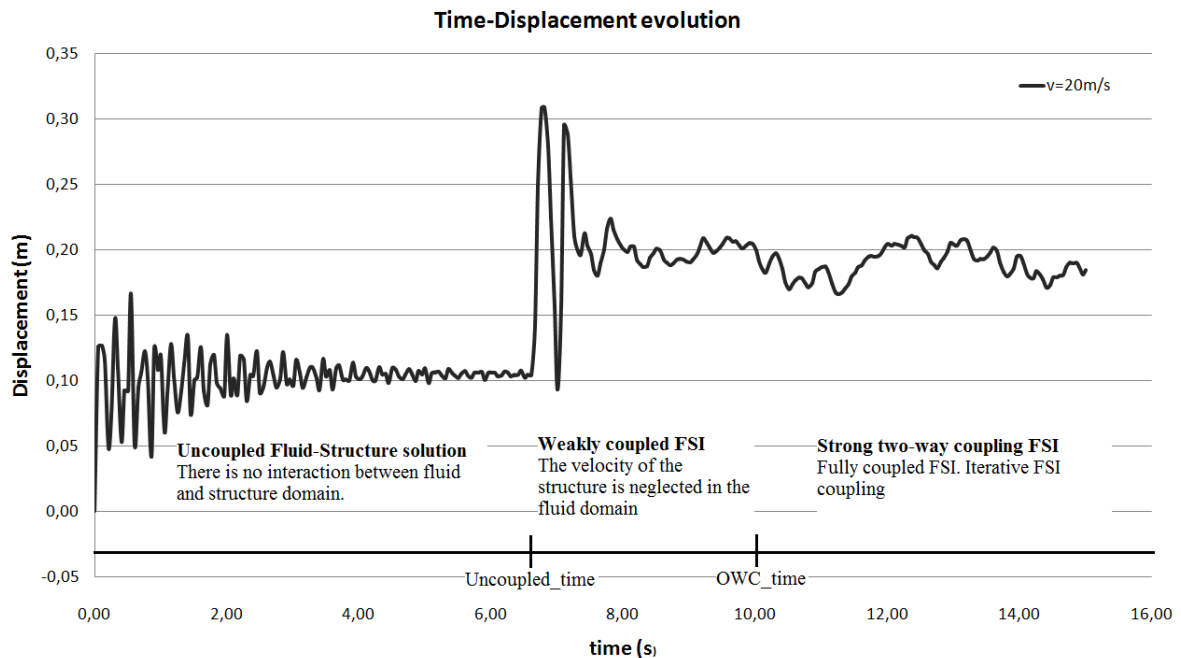


Figure 4.4. Overall graphic example of the different steps taking part in the algorithm solution

In Annex I identification time implementations algorithm are presented, as well as the full algorithm for the two-way partitioned fluid-structure coupling involving thin-wall light-weight structures.

Chapter 5:

Wind tunnel simulation

In this chapter, an application of the algorithm presented in the previous chapter will be applied to the simulation of a thin light-weight structure embedded in a wind tunnel. First, conventional methods for the analysis of this type of structure are simulated. The conventional methods consist of obtaining the air pressure distribution along the structure surface using a simplified method, such the norm EN 1991-1-4: 2005 and a purely CFD simulation with a rigid body. Once the pressure distribution is obtained, this is applied into a flexible solid and a purely CSD is performed.

The results obtained from the conventional methods will be compared with those obtained from the algorithm subject of the present work (strong two-way coupling method) in order to analyze the importance of this method when dealing with structures undergoing large displacements due to wind loads.

5.1 Model

The overall model consists of an inflatable aircraft hangar, a light-weight structure, placed into a virtual wind tunnel represented by a parallelepiped fluid domain. A constant velocity is prescribed at the inlet of the virtual wind tunnel. Structural model

A tutorial which explains the different steps to model the structural and fluid model has been created and included in Anex II.

5.1.1 Structural model

5.1.1.1 Geometry and material

The structure considered in this simulation is an inflatable structure with the geometry depicted in Figure 5.1. This structure simulates the standard module developed by BuildAir Company, entitled “H20 hangar”.

The dimensions for the H20 inflatable hangar are shown in Table 5-1:

Table 5-1. Dimensions of H20 inflatable hangar

Element	Dimension	Units
Clear-span width	20.00	m
Total width	25.48	m
Clear standard height	10.00	m
Standard length	6.34	m
Nominal diameter of a tube	2.74	m

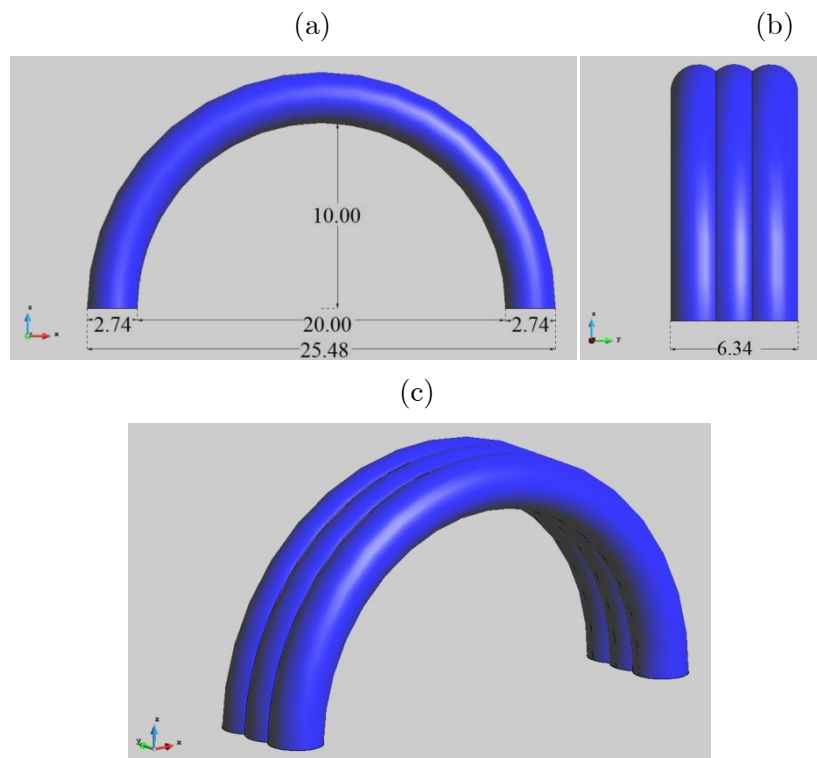


Figure 5.1. Geometry of the inflatable H20 hangar- (a) front elevation (b) lateral elevation (c) three-dimensional view

The whole structure is composed of an elastic textile material, PLASTEL 8820. Properties of the PLASTEL 8820 are defined in Table 5-2.

Table 5-2. PLASTEL 8820 properties

Property	Value	Units
Density (ρ)	1250	Kg/m ³
Young modulus (E)	0.31	GPa
Poisson ratio (ν)	0.3	-
Thickness (t)	0.6	mm

5.1.1.2 Load case

The analysis of the behaviour of the hangar exposed to wind loads is the objective of the simulation. Hence, only external pressure due to wind will be considered as a variable force in the simulation.

Thereby, the load cases of the model are:

Permanent loads:

- Self-weight of the membrane PLASTEL 8820 material.
- Constant internal pressure: In order to provide stiffness to the structure, inflatable structures are subjected to an internal pressure.

Variable load:

- External pressure due to wind: The external pressure is obtained from the strong two-way coupling presented in this thesis. Examples of 10, 20 and 35m/s of the inlet velocity will be analysed.

Table 5-3 shows the load case of the model, and Figure 5.2 shows a representation of the load case taken into account in the model simulation.

Table 5-3. Load case

Load	Value	Units
Internal pressure (P^{int})	2000	Pa
Self-weight ⁷ (SW)		N/m ²
External pressure ($P_{(v)}$)	$P(v)$	Pa

⁷ The self-weight of the structure is obtained directly from the properties of the material and the geometry.

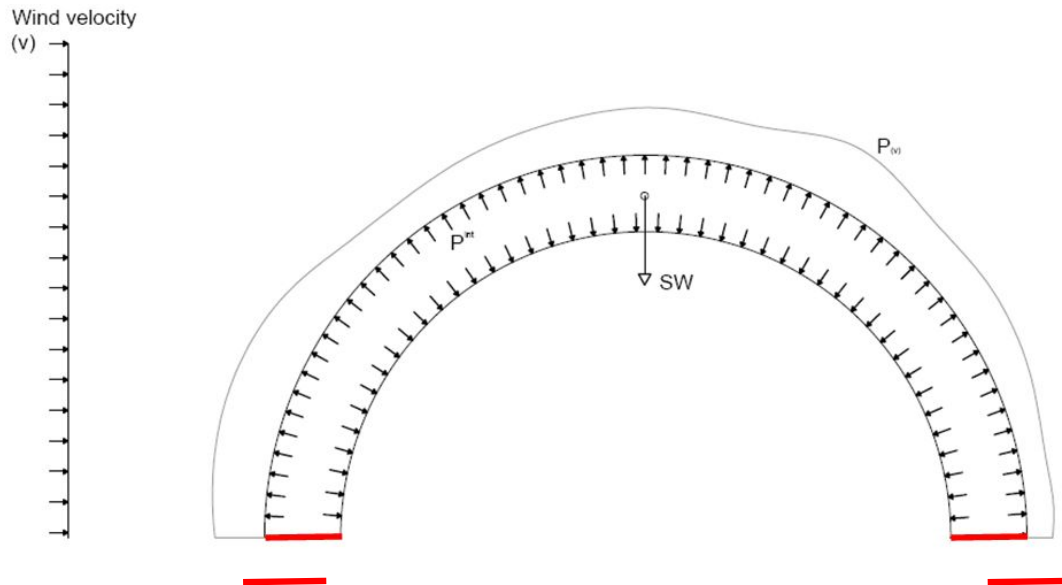


Figure 5.2. Representation of the load case

5.1.1.3 Boundary conditions

The structure is anchored on the ground; hence the displacements in all directions are fixed over the lines in the base of the structure, see red lines in Figure 5.2.

5.1.1.4 Structural mesh

In order to obtain reliable results in the structure, a convergence analysis is performed.

Table 5-4. Data of different meshes for convergence analysis

mean size	nodes	Maximum displacement (m)
1,5	701	0,105
1	1515	0,111
0,75	2599	0,112
0,5	5277	0,1125

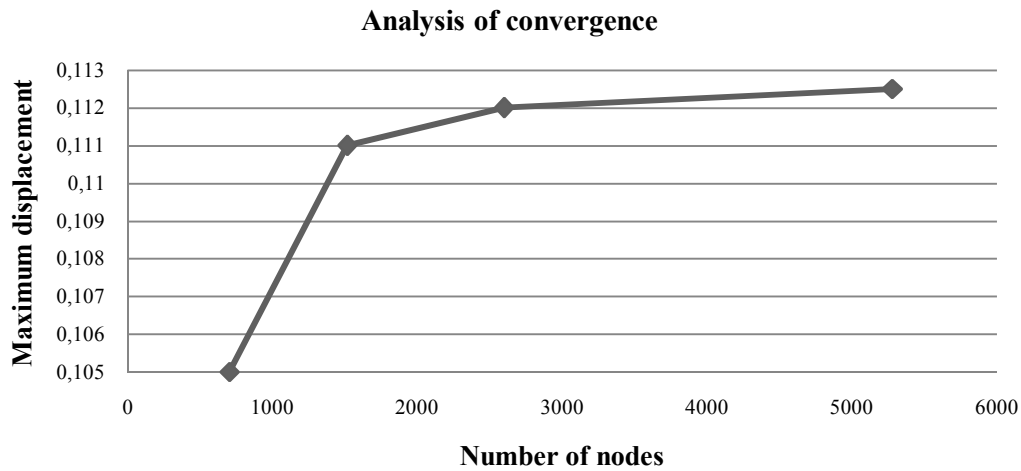


Figure 5.3. Convergence analysis for the structural mesh

A mean element size of 0.5 meters can be estimated to be a reasonable size for the analysis as it is depicted in Figure 5.3.

5.1.2 Fluid model

Fluid model is automatically generated by assigning the coordinates of the boundaries. Furthermore, the number of divisions for each direction and the distance and level of refinement in the area of interest must be also defined.

Fluid flow, in addition of the velocity, is function of the viscosity and density of the fluid. Properties of the fluid are presented in Table 5-5.

Table 5-5. Fluid properties

Property	Values	Units
Dynamic viscosity (μ)	$1.5 \cdot 10^{-5}$	Kg/(m·s)
Density (ρ)	1.21	Kg/m ³

5.1.2.1 Wind tunnel size

Flow could be affected if the size of the wind tunnel is too small. The walls of the wind tunnel constrict and artificially accelerate the flow around the model. It also prevents the formation and shedding of vortices downstream of the model.

For obtaining best results, the distance between the structure and the fluid mesh boundaries can be estimated with the relations shown in Figure 5.4.

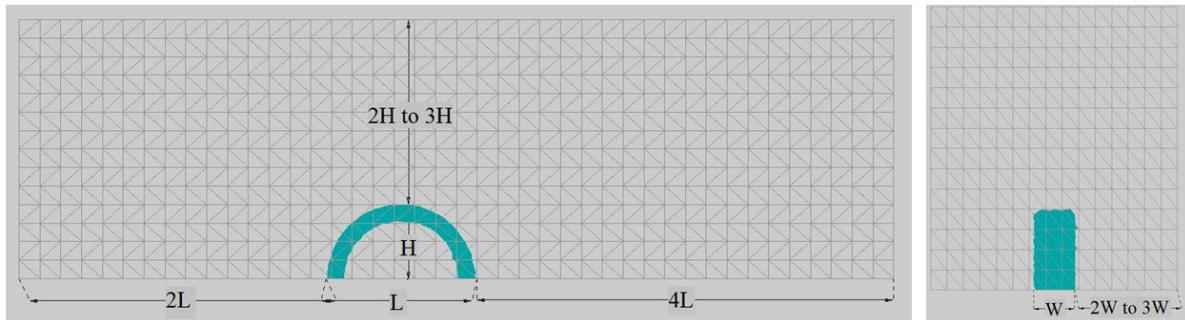


Figure 5.4. Dimension relations for a wind tunnel size

However, in order to optimize the computational cost, a study of the flow with respect to the principal direction of the velocity (longitudinal direction) has been carried out. A distance of $3L$ downstream of the structure has been studied.

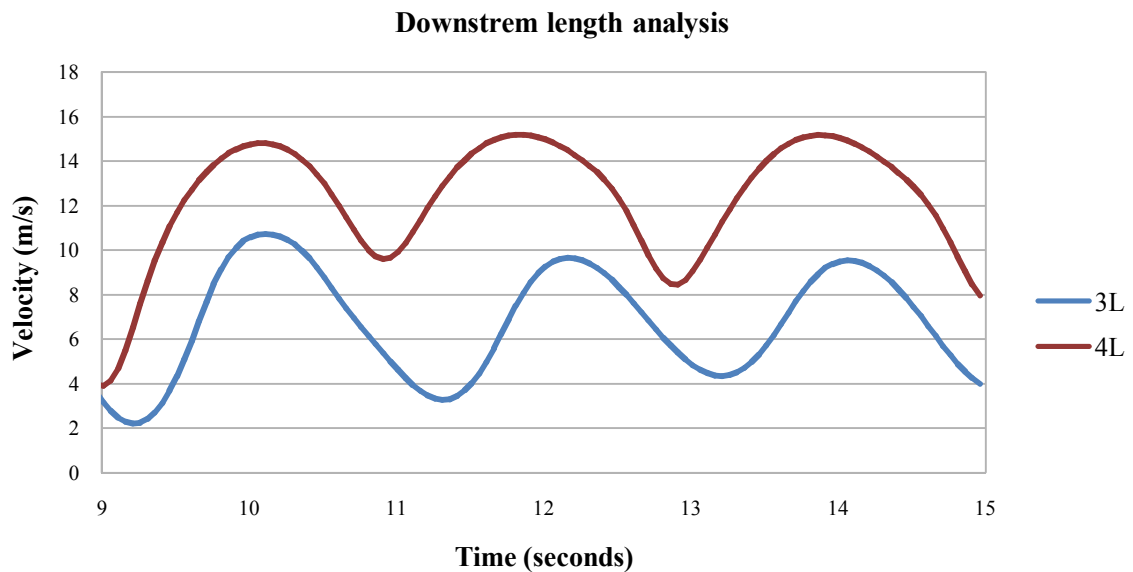


Figure 5.5. Flow analysis of the distance downstream of the structure

Table 5-6. Data resulting from the flow analysis

Downstream distance (m)	frequency f (Hz)	Maximum pressure (Pa)	Minimum pressure (Pa)
102 (4L)	0.52	263	-163
76.5 (3L)	0.5	263	-160

From Figure 5.5 and Table 5-6 we can justify that the distance of $3L$ downstream of the structure gives sufficient reasonable results, since the frequency shown in both cases are practically equal and the difference between the corresponding pressures are insignificant. Thereby, the wind tunnel size modelled for the analysis is as defined in Table 5-7:

Table 5-7. Wind tunnel dimensions

Reference Distance (m)	Total length (m)
$L= 25.48$	152
$H= 12.74$	39.50
$W= 6.34$	45

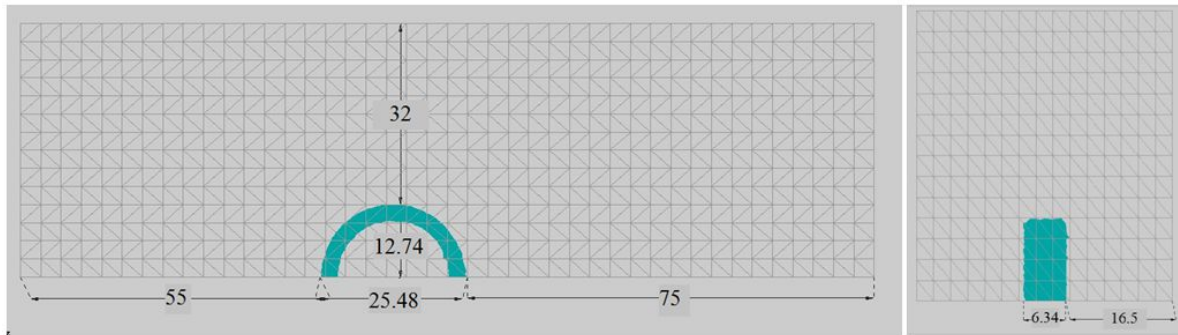


Figure 5.6. Wind tunnel dimensions

5.1.2.2 Wind tunnel mesh

The wind tunnel domain is discretized by tetrahedral elements. The subdivisions of the box must be small enough for not disturbing the results but big enough in order to reduce computational cost. Furthermore, the mesh is refined around the structure so as to ensure accurate results in the area of interest.

In accordance with the experience of the algorithm developers, best way to set the wind tunnel mesh is ensuring that the size elements in the refinement area must be similar to the size of the structure element. Following, a picture depicting the refinement fluid mesh around the structure is shown.

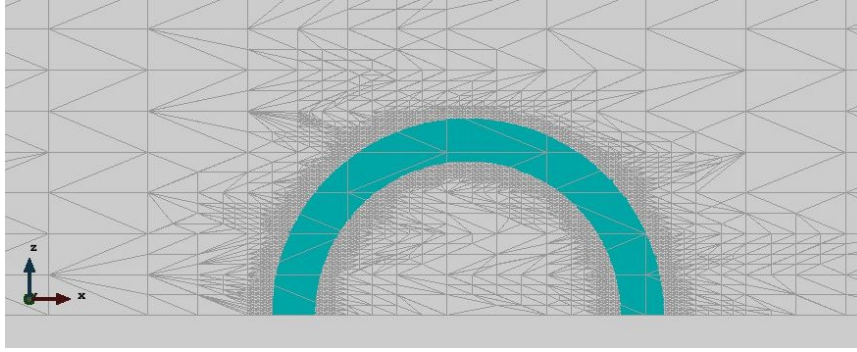


Figure 5.7. Refined distance around the Lagrangian image

Wind tunnel subdivisions and parameters of the refinement area are defined in Table 5-8. X direction is the longitudinal length in which the inlet velocity is applied, Y direction the box width and Z the height. The number of tetrahedral elements in X, Y and Z directions are defined by nX , nY and nZ , respectively. The refinement element size is defined by the size of the tetrahedral size element divided by 2^n , where n is the value of refinement level. The area of refinement is created in a refined distance R around the structure.

Table 5-8. Parametric properties of wind tunnel domain

	nX	45
Subdivisions	nY	15
	nZ	14
Parameters of refinement area	Refinement level, n	3
	Refinement distance (m), R	2

Figure 5.8 depicts the final size of the wind tunnel domain with a representation of the embedded structure.

Figure 1.1

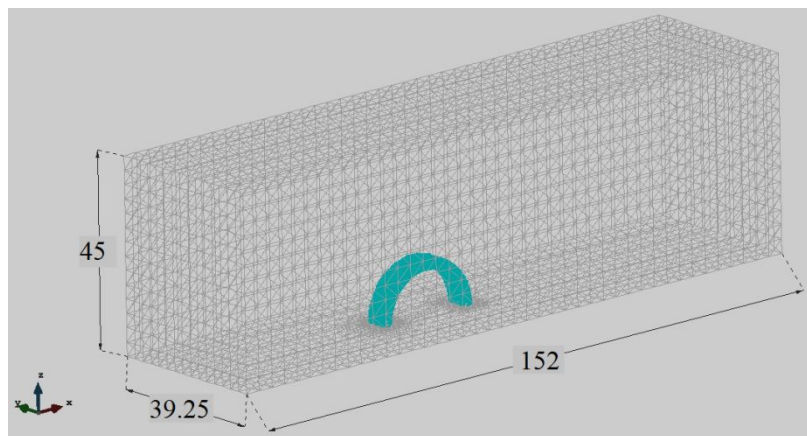


Figure 5.8. Wind tunnel mesh and size of the box

5.2 Wind action loads due to EN 1991-1-4: 2005 simplifications

The simulation consists in the application of a static air pressure onto the structure surface according to the norm EN 1991-1-4:2005 for the analysis of wind actions loads. The simplified air pressure distribution is applied onto the flexible structural model and a purely CSD will be performed, thus fluid model is not used for this simulation.

5.2.1 Variable actions due to wind

The norm specifies that the wind action is represented by a simplified set of pressures whose effects are equivalent to the external dynamics effects of the turbulent wind. The effect of the wind on the structure depends on the size, shape and dynamic properties of the structure.

The norm defines a design peak velocity depending on the wind climate, the terrain roughness and orography, and the reference height. However, these aspects have not been taken into account, since this is not the interests of the project. A design peak velocity of 35m/s has been considered for the simulation in order to compare later the results obtained with a strong two-way coupling simulation.

For circular cylindrical roof and domes the norm defines three zones for the distributions of the pressures acting over the structure depending on the intensity or direction of the pressure. Figure 5.9 shows a scheme of the geometrical parameter and pressure distributions for circular cylindrical roofs and domes. Geometrical parameters for the structure of interest are defined in Table 5-9.

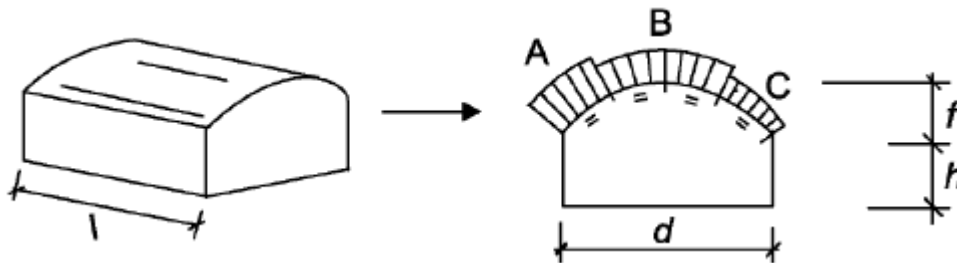


Figure 5.9. Geometric parameters and pressure distribution over cylindrical roof and domes

Table 5-9. Geometrical parameters

Geometric parameter	Length (m)
l	6.34
d	25.48
h	0
f	12.74

The equivalent static pressure (Q_d) is obtained using the Bernoulli equation modified by an exposure coefficient (C_e). This coefficient depends of the height of the structure (z) and the type of ground where the structure is placed. However, these parameters have not been taken into account in the coupling simulation, and the consideration of such parameters in this analysis would alter the results of interest. Hence, a unitary value of C_e is considered in this analysis.

Thereby, the equivalent static pressure (Q_d) according to EN 1991-1-4:2005, considering a velocity of 35m/s and a fluid density of 1.21 Kg/m³ is:

$$Q_d = \frac{1}{2} \rho v_d^2 \cdot C_e = 741.12 \text{ Pa}$$

This value leads to the pressure applied in any of the three areas represented in Figure 5.9 by using the coefficients which depends on the geometric parameters (f/d and h/d). These coefficients can be determined using the abacus represented in Figure 5.10.

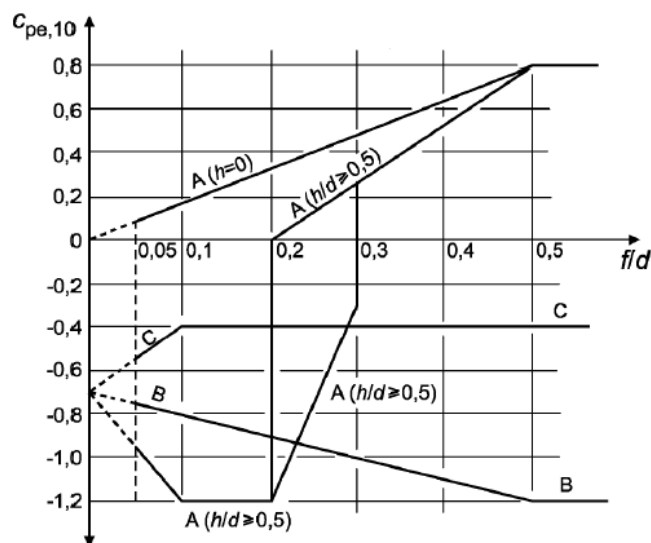
**Figure 5.10. Abacus for external pressure coefficient**

Table 5-10 summarizes the parameters obtained in Figure 5.10 to determine the three wind pressures over the inflatable structure in terms of equivalent static pressure. Positive values of pressure define compressions on the structures while negative values imply suction effects.

Magnitude	Value	
Relation f/d	0.5	
Relation h/d	0	
coefficient A/ Pressure A	0.80	593 Pa
coefficient B/ Pressure B	-1.20	-889 Pa
coefficient C/ Pressure C	-0.40	-297 Pa

Figure 5.11. shows a graphical representation of the air pressure distribution according to norm EN 1991-1-4:2005

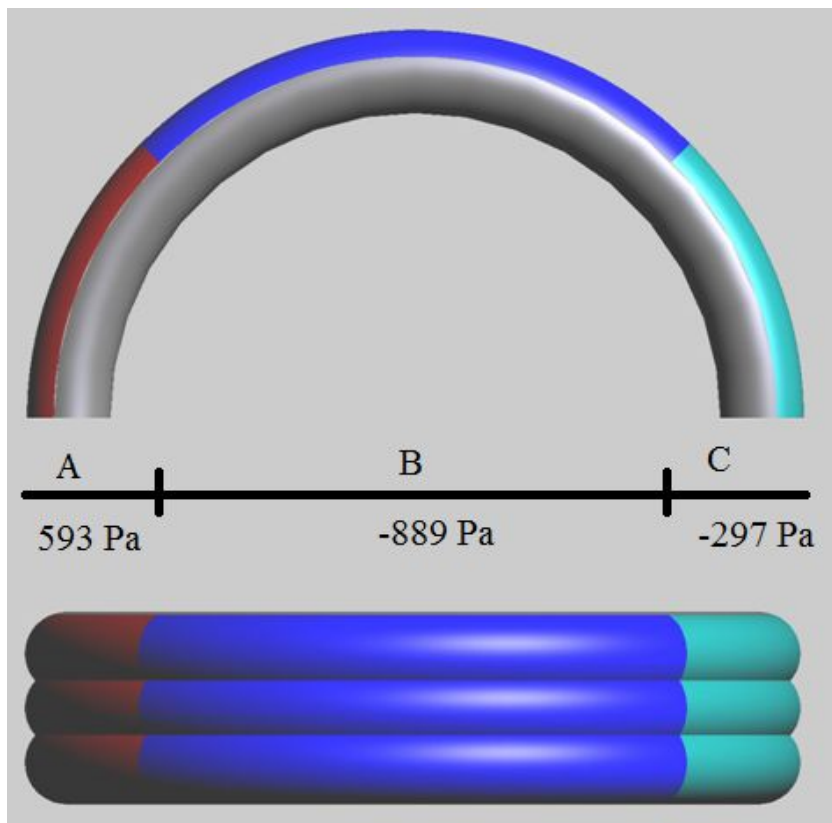


Figure 5.11. Air pressure values and areas of application.

5.2.2 Results

A CSD is carried out for the inflatable structure due to self-weight, internal pressure of 2000 Pa and the air pressure according to norm EN 1991-1-4:2005. In this simulation only the displacement solution will be discussed. It is worth noting that no displacement evolution is shown since, due to the constant distribution of applied forces, a steady solution is obtained. Figure 5.12 depicts the displacement solution for the distribution of pressure obtained in the calculations of the Eurocodes. Large displacements can be observed on the top of the structure. These displacements are caused by the large negative pressure applied on the top of the structure.

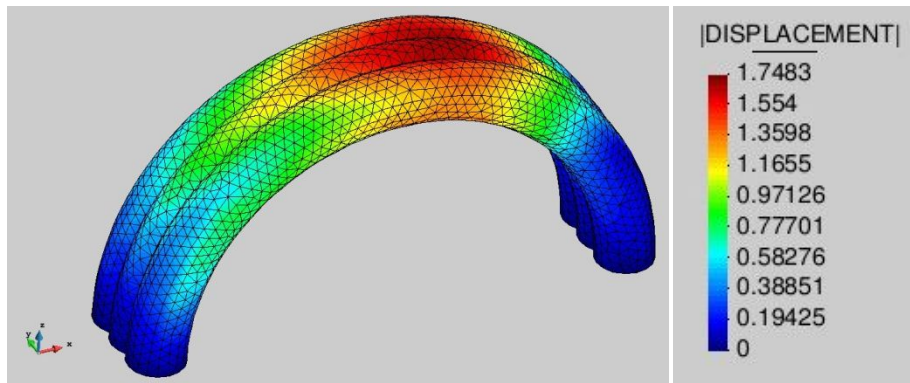


Figure 5.12. Displacements obtained in the simplified method according to Eurocode 1.

Table 5-11. Summary of values according to EN 1991-1-4:2005 ($v_d=35\text{m/s}$)

parameters		Values
Outlet	Max. Pressure	593 Pa
	Min. Pressure	-889 Pa
	Back. Pressure	-297 Pa
Inlet	Max. Displacement	174.8 cm

5.3 Simplified CFD

A computational fluid dynamics simulation is carried out with a rigid body solid inside the fluid domain. The simulation of a CFD allows us to obtain a pressure distribution over the rigid body solid. Figure 5.9 represents the pressure field obtained in a CFD simulation with an inlet velocity of 35m/s. The pressure distribution over the rigid body is applied onto a flexible structure as it is shown in Figure 5.14.

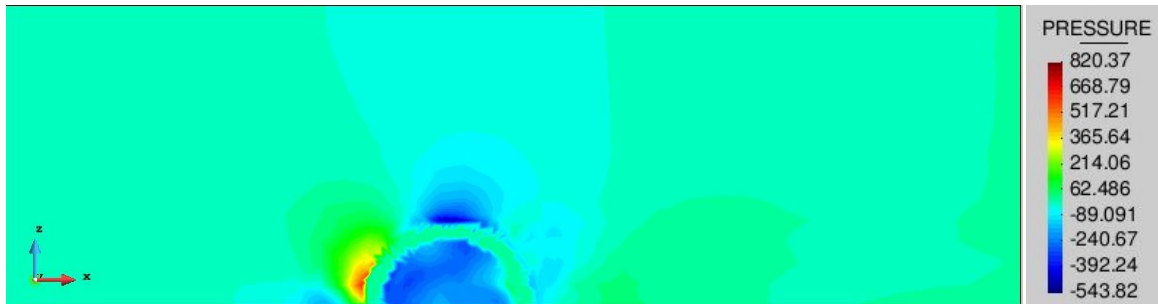


Figure 5.13. Pressure field obtained in a CFD simulation with an inlet velocity of 35m/s.

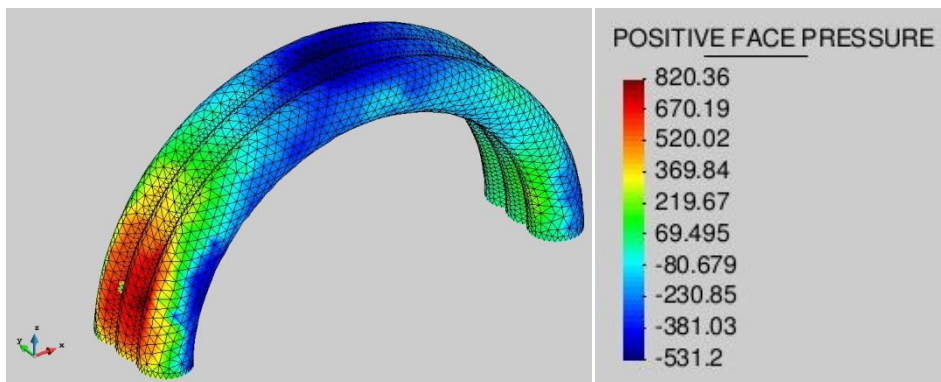


Figure 5.14. Pressure distribution obtained in the CFD simulation

5.3.1 Results

A computational structural dynamics is carried out considering the self-weight, internal pressure and the distribution of pressures obtained in the CFD simulation. Incremental pressure in the CSD is taken into account in order to provide stiffness to the structure. Figure 5.15 depicts the pressure in an arbitrary node of the maximum pressure area for a simulation of 10, 20 and 35 m/s of the inlet velocity.

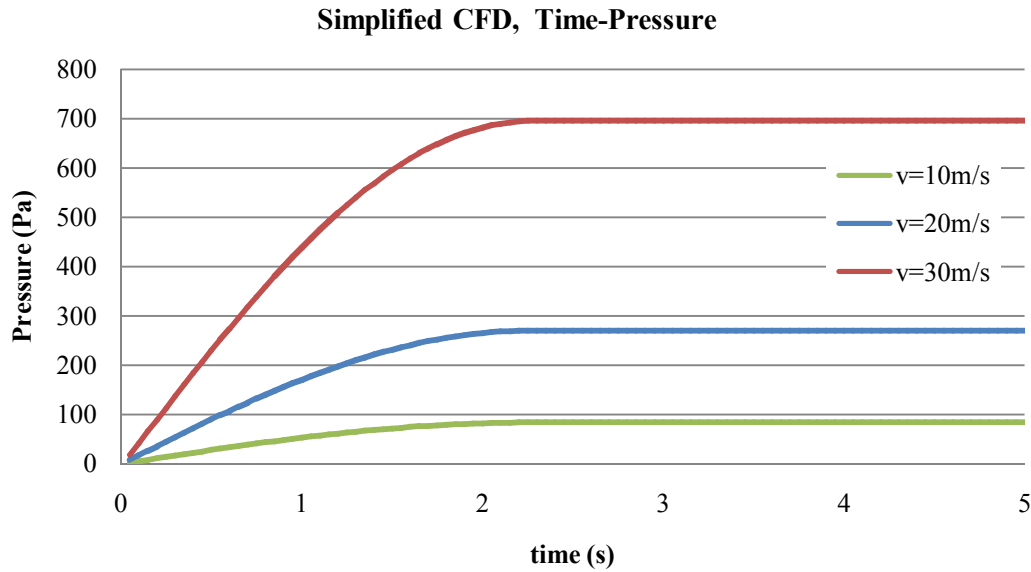


Figure 5.15. Time-pressure graph applied in a CSD for different inlet velocities.

An analytical solution for pressure values exerted by a fluid in movement can be estimated by the Bernoulli equation:

$$P = \frac{\rho v^2}{2}$$

It is worth noting that this expression is an approximate solution for the pressure in a static rigid body. Solutions of the analytical expression with the same fluid parameters and inlet velocities studied in this model are presented in Table 5-12.

Table 5-12. Analytical pressure solutions

Velocity (m/s)	Pressure (Pa)
10	60.5
20	242
35	741

One can observe that values of the pressure are similar to the values obtained with the analytical solution as it is represented in Table 5-12.

Displacements obtained in the CSD due to the air pressure are shown in Figure 5.16. Furthermore, Figure 5.17 represents an evolution on time of the displacements obtained in the CSD simulation due to the air pressure. Due to the constant pressure applied, steady solutions are obtained for the three velocities.

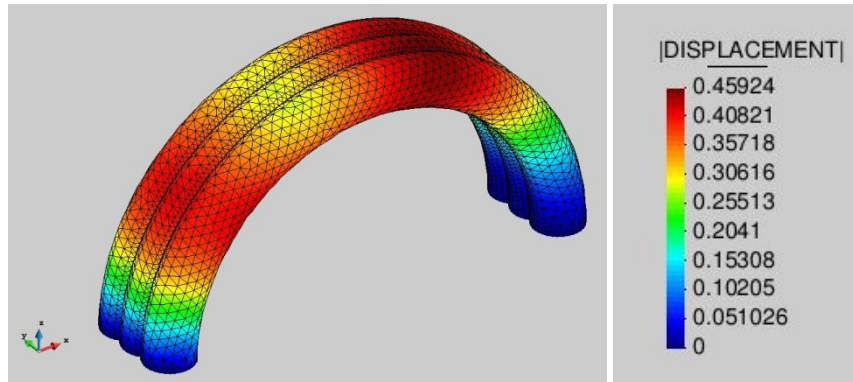


Figure 5.16. Displacements obtained in a CSD after application of air pressure distribution.

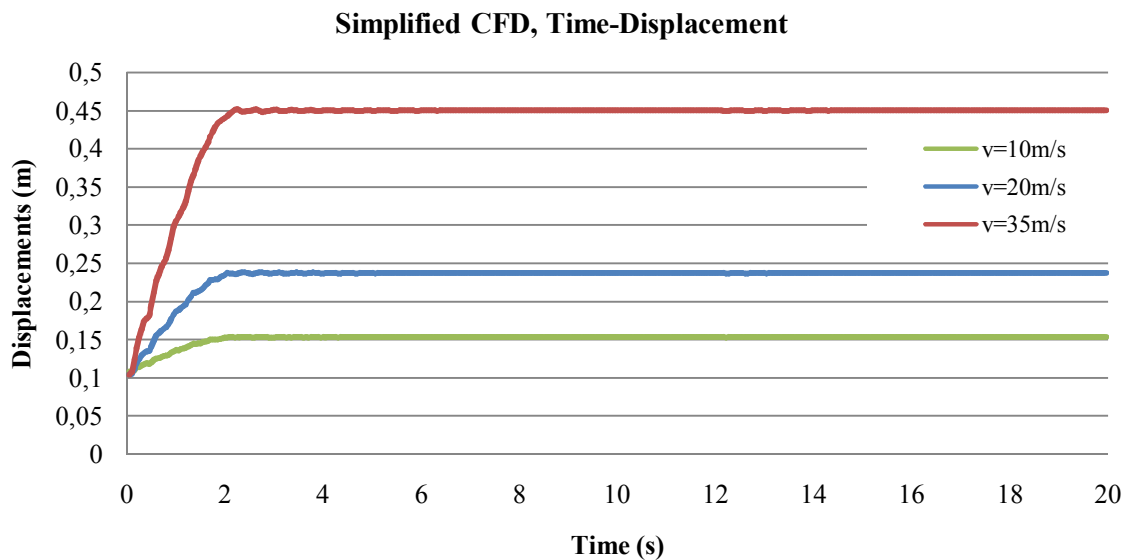


Figure 5.17. Displacement evolution due to a constant air pressure.

Following, a summary of the results obtained from a purely CSD simulation, with a previous CFD simulation with a rigid body in order to obtain the air pressure distribution, is presented:

Table 5-13. Summary of values according to a simplified CFD analysis

Inlet velocity (m/s)	Max. Pressure (Pa)	Max. Displacement (cm)
10	83	15.33
20	270	23.73
35	695	44.98

5.4 Strong two-way coupling simulation

The algorithm presented in the present work is applied in next simulation in order to study and analyze the fluid-structure interaction in a strong-two way coupling.

5.4.1 Results

Inlet velocities of 10, 20 and 35 m/s are applied in different simulation in order to analyze the motion of the structure when different Reynolds numbers are applied. The results obtained with the strong two-way coupling method are presented below:

5.4.1.1 Displacements

Following, the results of displacements for different inlet velocities are shown. Figure 5.18 (a) represents the displacement produced by the internal pressure and the self-weight prior to applying the fluid pressure. Figure 5.18 (b) (c) and (d) depict the displacements produced in the structure due to the pressure exerted by a wind velocity of 10, 20 and 35 m/s, respectively. It is possible to observe how the structure tends to deform to the sense of the wind direction, and also, how the displacements increase as the velocity increases. Furthermore, shape deformation changes owing to the increase of velocities, obtaining large displacements on the upstream side of the structure, see Figure 5.18 (d).

The deformation produced due to wind velocity of 20m/s is represented in Figure 5.19. The structure deforms towards the direction of the wind with a maximum displacement of around 22cm. Furthermore, a lift is produced on the top of the structure.

A graphic representation on time of the displacements for the different velocities is depicted in Figure 5.20. In first seconds of the analysis, the displacement are the same, due to there is no coupling interaction. Close to 9.5 seconds, the coupling takes place and large instantaneous displacement is observed. At around 11 seconds the structural displacement becomes stable due to the two-way coupling process.

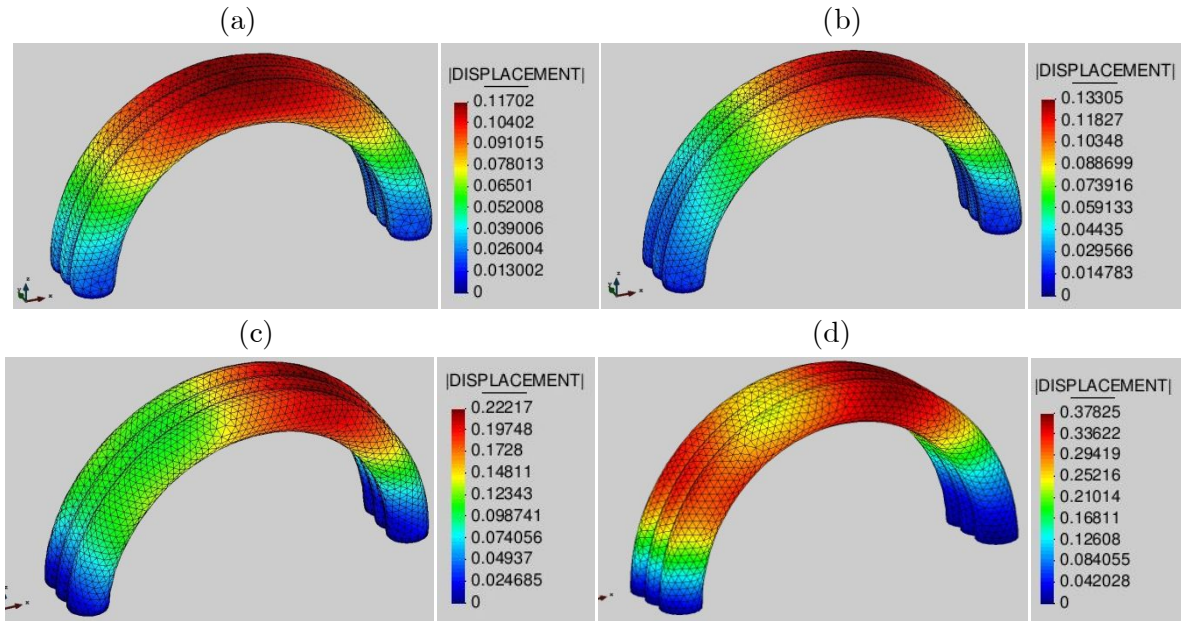


Figure 5.18. (a) Displacement on the static solution of the structure (b) Displacement produced by an inlet velocity of 10m/s (c) Displacements due to a velocity of 20 m/s (d) Displacements due to an inlet velocity of 35 m/s

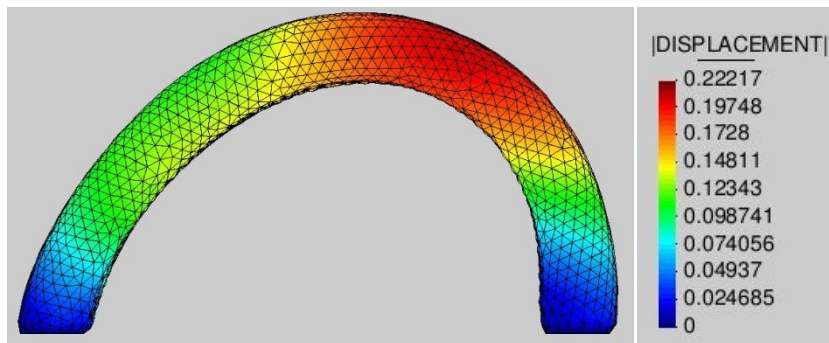


Figure 5.19. Deformed shape of the structure due to an inlet velocity of 20m/s

In order to analyse in detail the behaviour of the different velocities, a zoom on the two-way coupling process is done, see Figure 5.21. Low velocities (10m/s) tend to a steady solution, while high velocities (20 and 35 m/s) tend to an oscillatory solution. Furthermore, as the velocity increases the amplitude of the spectrum increases. The oscillatory behaviour is produced by the unsteady flow induced by high velocities around the structure. In other words, as Reynolds number increases unsteady flow around the structure occurs, producing an oscillatory motion of the structure.

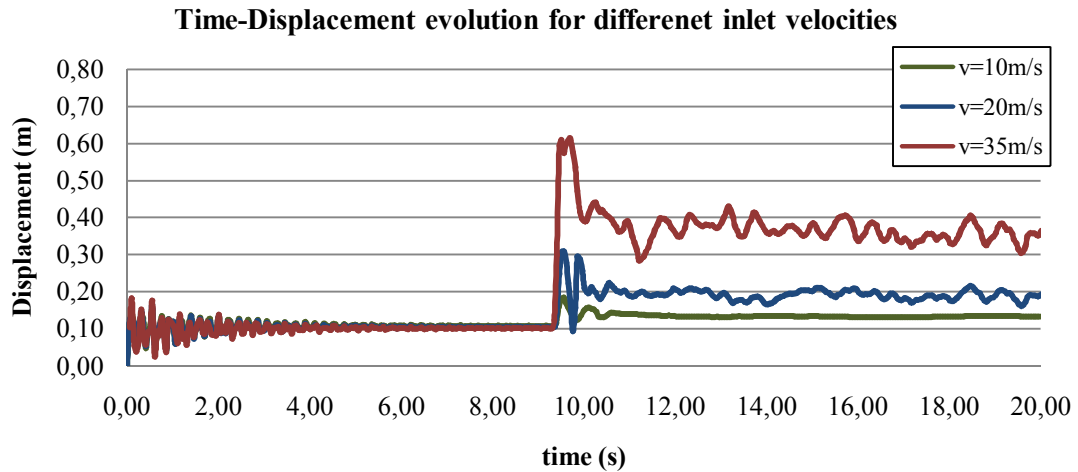


Figure 5.20. Graphic representation on time of the displacements produced by different inlet velocities

In order to analyse the displacements for the different velocities, a significant displacement is calculated for each inlet velocity. Due to the similarity behaviour between the observed displacements and the oceanic wave spectrum, the significant displacement has been obtained with the mean of the highest third of the peak displacements, see Walter Munk [26]. Significant displacements are represented in Figure 5.21 as dashed lines. Table 5-14 presents the values of significant displacements and Reynolds number for each velocity.

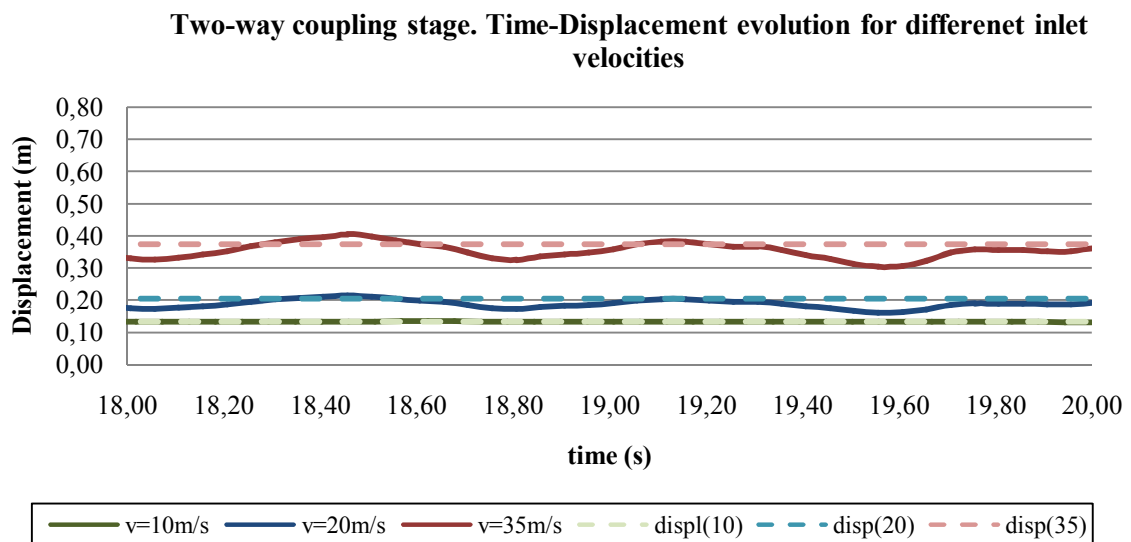


Figure 5.21. Zoom in the two-way coupling process of Figure 5.20

Table 5-14. Significant displacements and Reynolds number for different velocities

Inlet Velocity (m/s)	Sign. displacement (cm)	Re (10^6)	f (Hz)
10	13.45	100.8	Steady solution
20	20.66	201.7	1.4
35	37.48	352.9	1.1

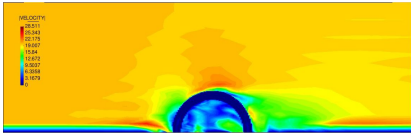
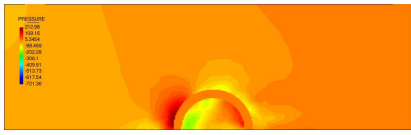
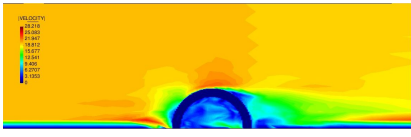
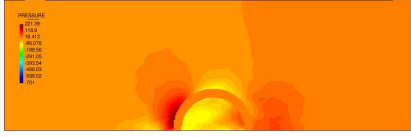
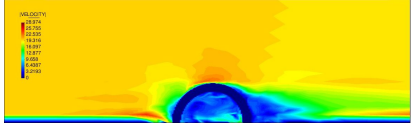
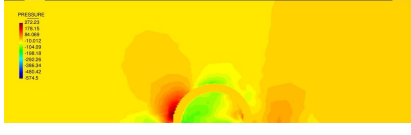
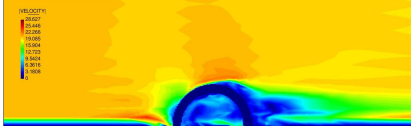
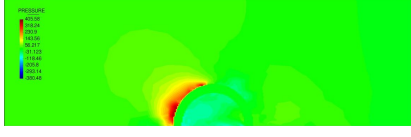
5.4.1.2 Positive face pressure

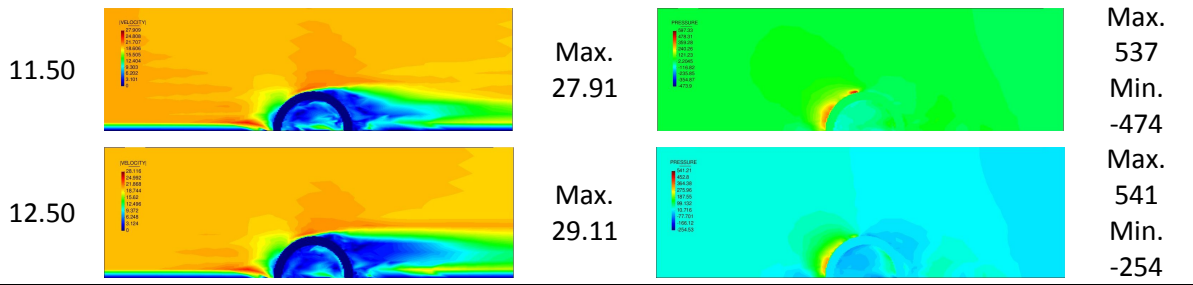
Following the results of pressure over the fluid and structure domains are presented. First, some step results over the fluid domain of one second time-step are presented in Table 5-15. Results correspond to an inlet velocity of 20m/s.

Times of 7.50 and 8.50 seconds represent the fluid solution on the uncoupled process. In these steps solution of the fluid are no yet correct. Large values in minimum pressure are obtained and fluid needs to stabilize.

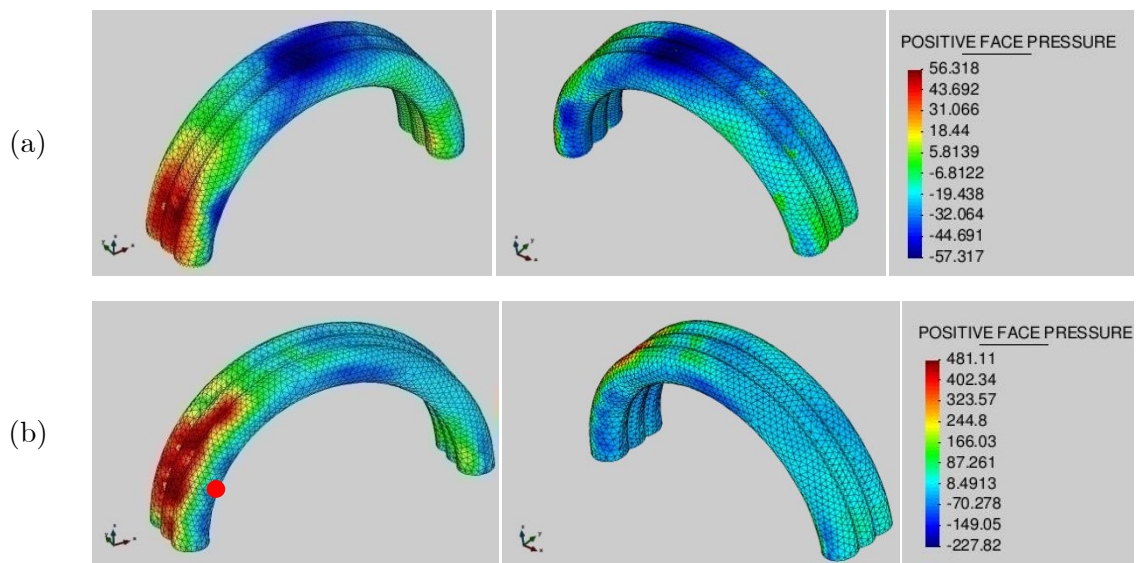
Times of 9.50 and 10.50 seconds represent the one-way coupling process. Times of 11.50 and 12.50 represent the fluid solution of the two-way coupling process. Pressure values are not predictive and have a “random” behaviour due to the unsteady flow. However a range of values can be established.

Table 5-15. Fluid results over time steps for an inlet velocity of 20m/s

Time (s)	Velocity	Results (m/s)	Pressure	Results (Pa)
7.50		Max. 28.51		Max. 213 Min. -721
8.50		Max. 28.22		Max. 221 Min. -701
9.50		Max. 29.97		Max. 272 Min. -574
10.50		Max. 28.63		Max. 405 Min. -380



Pressures obtained on the fluid solution are mapped onto the structure domain in each time step and following the strong two-way coupling method presented in Table 3-2. Figure 5.22 depicts air pressure distributions over the surface of the structure at time=19s for three inlet velocities. Figure 5.22 (a) represents the pressure with an inlet velocity of 10 m/s. Image in the left side shows the upstream side, while right image the downstream side. Maxim pressures are obtained on the front of the upstream side. Minimum values of pressure are obtained at the top of the structure; negative values of pressure represent suction effects of the fluid. Figure 5.22 (b) and (c) represent the values for velocities of 20 and 30 m/s. Also, maximum pressures take place on the front of the upstream side. However, although suction effect is also presented on the top of the structure, minimum values are obtained on sides of the upstream area – red dot market in Figure 5.22 (b) -. In Table 5-15 it is possible to observe vortices behind the upstream surface, fact that caused these values at the area of minimum pressures.



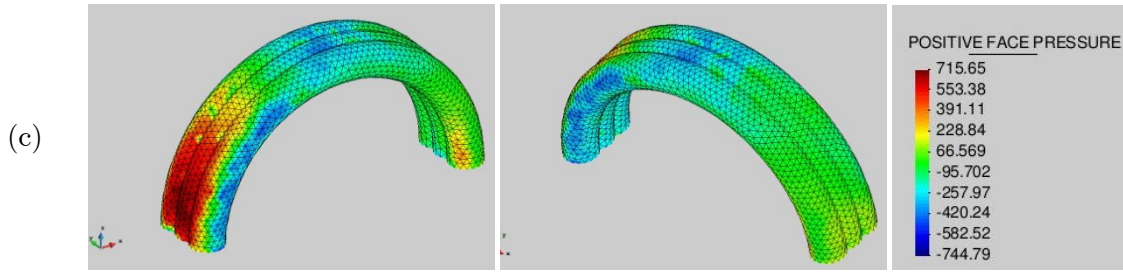


Figure 5.22. Pressure configuration over the structure at time=19s. (a) $v=10\text{m/s}$ (b) $v=20\text{ m/s}$ (c) $v=35\text{m/s}$

As expected, pressure increases as the velocity does. Furthermore, negative values of pressure are present on the top of the structure, fact that demonstrates the lift effect on the deformed shape. Also, the increase of pressure on the front side, for high velocities, explains the displacement occurred on that area. Maximum pressure takes relevance against the internal pressure, and the structure suffers large displacements in the front side of the upstream surface.

Values on time of the air pressure applied onto the structure are presented in Figure 5.23. Pressures due to low velocities consolidate the steady flow of the solution. Furthermore, values of the pressure are close to the values for the analytical solution presented in Table 5-12. For high velocities, in which fluid flow presents unsteady solution, pressure values present a spectrum with large amplitudes. A reason for high values on pressure arises due to the movement of the structure towards the initial position. The frequency of the structure is different to the frequency of the air flow. The structure moves against the air direction, due to the oscillatory motion of the structure, causing an additional pressure on the surface. On the other hand, when the structure tends to deform towards the direction of the wind, lower pressures are expected. For these cases, analytical pressure solutions are not accurate enough, presenting large difference in the solutions.

Figure 5.24 shows the results of the pressure at the strong-two way stage of the simulation. With the same criteria for obtaining the significant displacement, minimum and maximum significant pressures have been obtained. Dashed lines represent the minimum significant pressures and point lines the maximum ones. Table 5-16 presents the maximum and minimum significant values for pressure as well as the amplitude of the pressure spectrum.

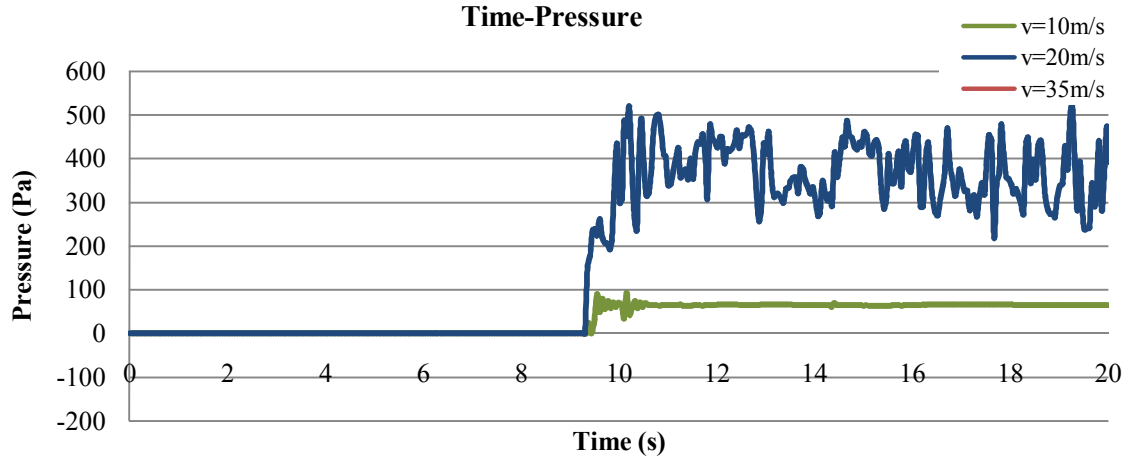


Figure 5.23. Evolution on time of the air pressure applied onto the structure surface

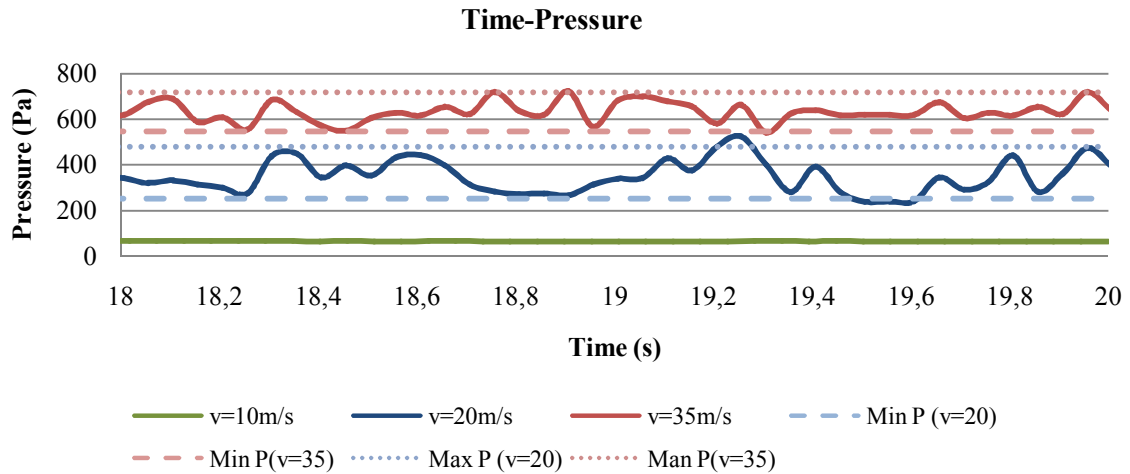


Figure 5.24. Pressure solution at the strong two-way coupling stage

Table 5-16. Significant pressures and amplitude of the pressure spectrum

Inlet Velocity (m/s)	Max. pressure (Pa)	Min. pressure (Pa)	Amplitude (Pa)
10	65	65	Steady solution
20	480	253	227
35	716	547	169

Unexpected solution are obtained, since amplitude obtained for an inlet velocity of 35m/s is smaller than the amplitude obtained in the simulation with an inlet velocity of 20m/s. However, in order to analyze this solution, a further analysis to study the frequency of the fluid flow and the natural frequency of the structure would be required.

5.4.1.3 Stresses

From the classical theory of arches, tensile forces, T can be estimated for a circular shape of radius R being subjected to a constant pressure q , see Figure 5.25 for a representation of the problem. The expression that provides the tensile force is:

$$T = q \cdot R$$

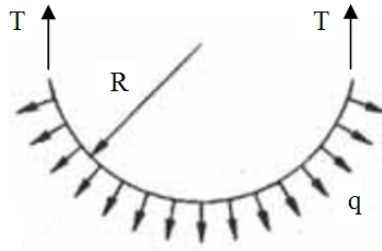


Figure 5.25. Tensile force in a circular element

This expression allows us to estimate the stresses produced in the structure studied in this project due to the applied internal pressure of 2000Pa. The nominal diameter of the tube is 2.74m. Hence, the expected stresses should be:

$$\sigma_1 = \frac{T}{e} = \frac{R \cdot q}{e} = \frac{1.37 \cdot 2000}{0.0006} = 4.6e + 06 \text{ Pa}$$

Principal maximum stresses solution due to self-weight and internal pressure is presented in Figure 5.26. Field stress along the surface presents a uniform distribution with a value in a range between $5e+06$ and $7e+06$ Pa, values of the same order of magnitude that the value obtained from the classical theory of arches.

Figure 5.27 depicts the distribution of the principal maximum stresses obtained at an arbitrary instant of the two-way coupling process for an inlet velocity of 35m/s. In this case, the field stress does not present a uniform distribution due to the applied air pressure. Surfaces where positive pressures are applied, present a decrease of stresses, since air pressures have opposite direction to the internal pressure. By contrast, stresses increase where suction effects appear.

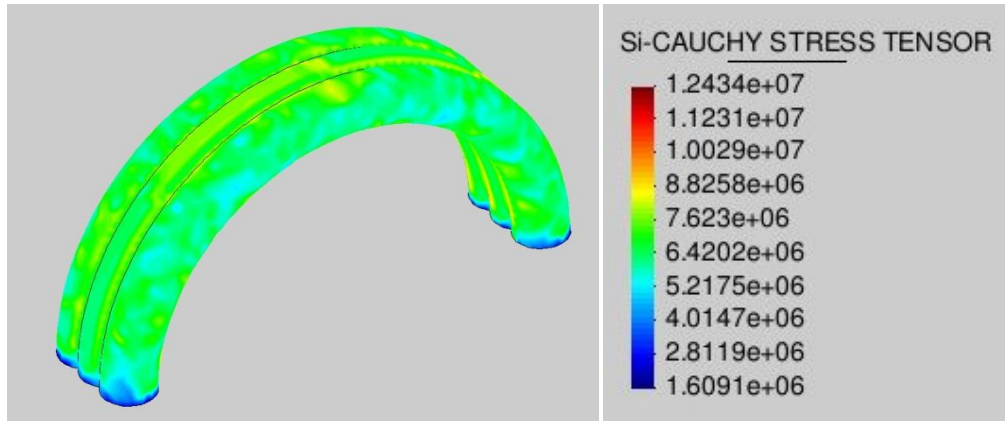


Figure 5.26. Principal maximum stress due to self-weight and internal pressure

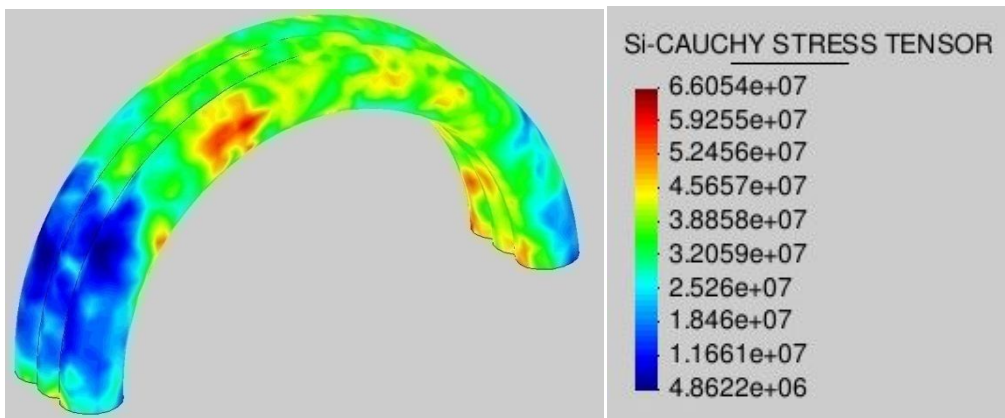


Figure 5.27. Principal maximum stresses due to self-weight, internal pressure and the air pressure

5.5 Summary and comparison of the results

In this section, a summary of the results obtained with the three methods will be presented. Furthermore, a comparison between simplified methods and the strong two-way formulation will be discussed.

5.5.1 Two-way coupling VS Simplified CFD

Table 5-17. Summary of the results for two-way coupling and Simplified CFD solutions

Magnitude	Inlet velocity (m/s)	Two-way coupling	Simplified CFD
	10	13.45	15.33
Displacements (cm)	20	20.66	23.73
	35	37.48	44.98

	10	56	83
Pressure (Pa)	20	481	270
	35	780	695

Low inlet velocities in a two-way coupling simulation present a steady solution. Hence similar results with a simplified CFD method are obtained. For high velocities the flow presents an unsteady solution and vortices appears close the structure surface. Due to the unsteady flow, large oscillations on the structure displacement occur with the consequently variation of pressure surfaces, that show large amplitudes in the oscillatory spectrum.

5.5.2 Two-way coupling VS EN 1991-1-4:2005

Table 5-18. Summary of the results for two-way coupling and EN 1991-1-4:2005 solutions

Magnitude	Two-way coupling	EN 1991-1-4:2005
Displacement (cm)	37.48	174.83

EN 1991-1-4:2005 defines the wind action load by a simplified set of pressures with the objective to represent the equivalent external dynamics effects of the turbulent wind. The obtained distribution of pressure over the structure surface according to EN 1991-1-4:2005 has a significant variation with this obtained from a computational fluid dynamics. Distribution of the pressure according to Eurocode has a significant conservative form, leading to large variation of the displacement solution between both simulations.

5.6 Engineering observations

In this section of the chapter, engineering observations related to industrial issues will be presented. Engineering companies engaged to the study of inflatable aircraft hangars have to deal with the restrictive values of the safety distance between the deformed structure and the aircrafts. These restrictive values come from the uncertainty of the conventional methods of analysis.

Different strategies with the objective of reducing the displacements and optimize the structure are presented. It is worth noting that no economic issues have been taken into account on the optimization solution due to this is not the purpose of the present work.

5.6.1 Stiffening straps

The idea is to provide stiffness to the structure by assembling stiffening straps around the structure. Two groups of straps are assembled, one group in the longitudinal direction and the other group in the transversal one. Figure 5.28 shows the structure modelled with the stiffening straps.

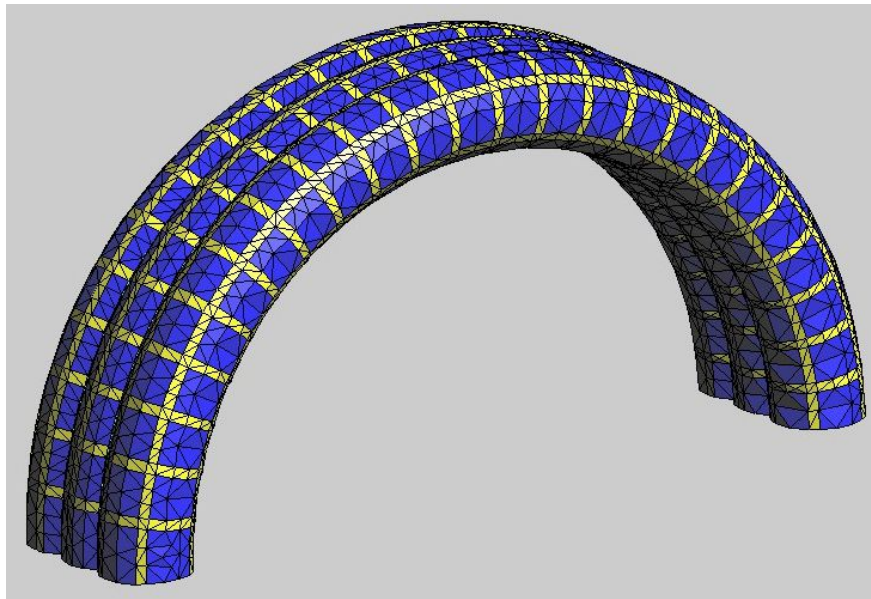


Figure 5.28. Stiffened structure with straps in longitudinal and transversal direction

Properties of the materials are shown in Table 5-19:

Table 5-19. PLASTEL 8820 and straps properties

Property	PLASTEL 8820	Straps	Units
Density (ρ)	1250	796	Kg/m ³
Young modulus (E)	0.31	0.5	GPa
Poisson ratio (ν)	0.3	0.3	-
Thickness (t)	0.6	0.9	mm
Width	-	300	mm

Following, displacements and principal stresses results are presented. Figure 5.29 represents the results obtained at the uncoupled stage, where structure is undergoing to the self-weight and the internal pressure, while Figure 5.30 represents the results at the strong two-way coupling stage. At this stage the structure is undergoing to self-weight, internal pressure and pressure exerted by the wind flowing around the structure. The applied inlet velocity for these solutions is of 35m/s.

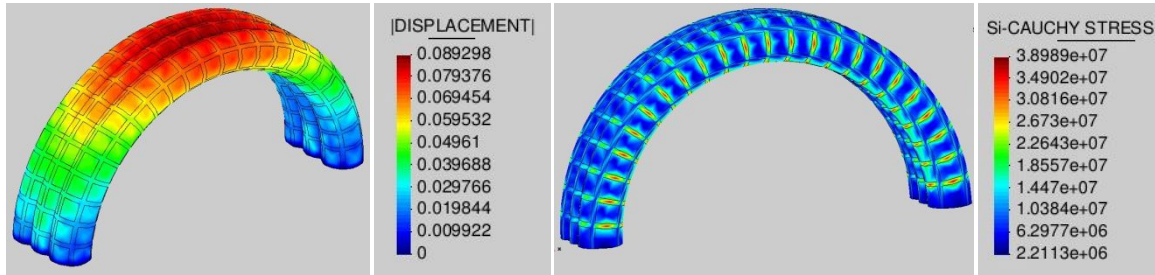


Figure 5.29. Displacements and Principal Stresses due to self-weight and internal pressure

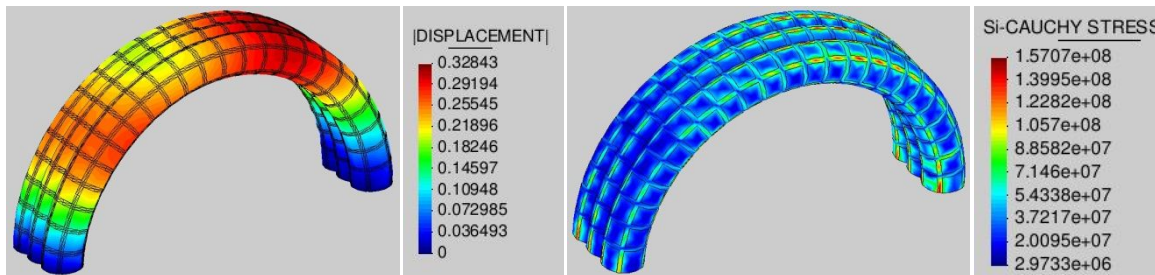


Figure 5.30. Displacements and Principal Stresses at time of the two-way coupling process

In order to compare the results, Figure 5.31 depicts the displacements evolution on time of the original and the stiffened structure that take place at the strong two-way coupling process. Also, in Table 5-20 the significant displacement of each model are summarized.

It is observed that the assembling of straps onto the structure provide stiffness to the structure, with the consequence reduction of displacements. For an inlet velocity of 35m/s and an inflatable structure of 20m of span undergoing to an internal pressure of 2000 Pa, around of 14% of displacement reduction is achieved.

Furthermore, straps take an important effect on the stresses. Due to the larger Young Modulus of the straps compared to the Plastel 8820 material, the straps bear an important

amount of stresses, lighten the stresses produced at the main structure due to the applied pressures. Observing the stresses results of Figure 5.29 and Figure 5.30, one can observe that transversal straps lighten the stresses produced by the inflating of the structure (internal pressure), while longitudinal straps reduce the stresses occurred at the main structure due to the displacements consequent of the wind pressure.

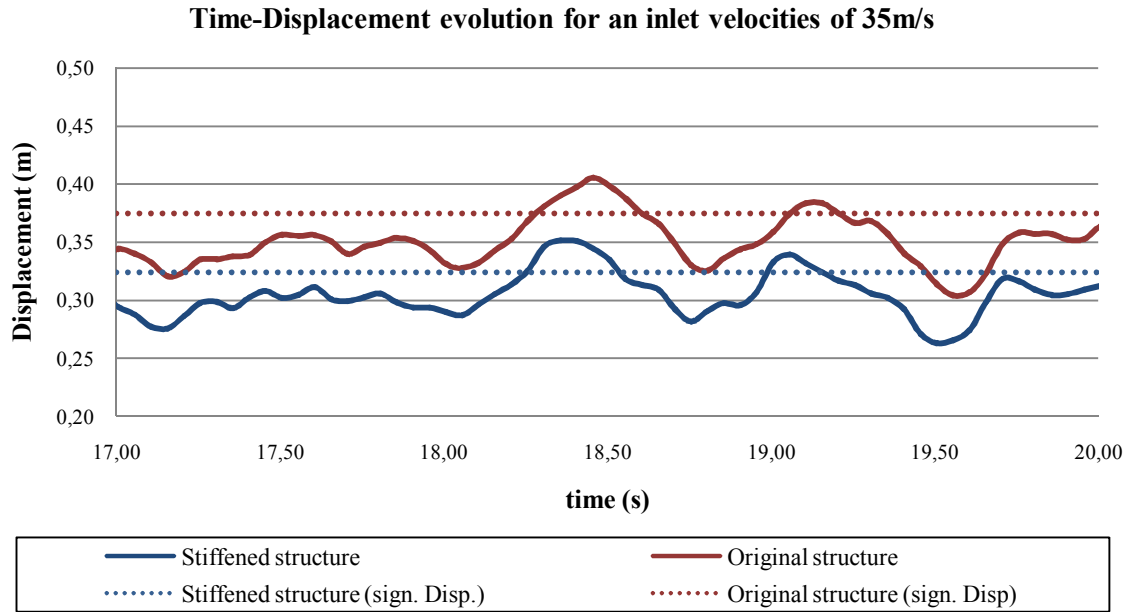


Figure 5.31. Stiffened and original structure time-displacement evolution at the two-way coupling stage

Table 5-20. Summary displacement for original and stiffened model

Structure model	Sign. Displacement	Units
Original structure	37.48	cm
Stiffened structure	32.42	cm

It is worth noting that presented results are indicative due to the rude mesh of the model. Membrane elements require a uniform Lagrangian mesh for a robust solution. Thus, the assembling of straps, with a surface much smaller than the area of the main structure, requires a very small mean element size, with the consequence of large number of elements as well as the reduction of the time step for calculations that imply a high computational cost.

5.6.2 Internal pressure

A different manner to provide stiffness to the structure is by the increasing the value of the internal pressure. Following, different solutions with internal pressures of 1000, 2000 and 3000 Pa are presented:

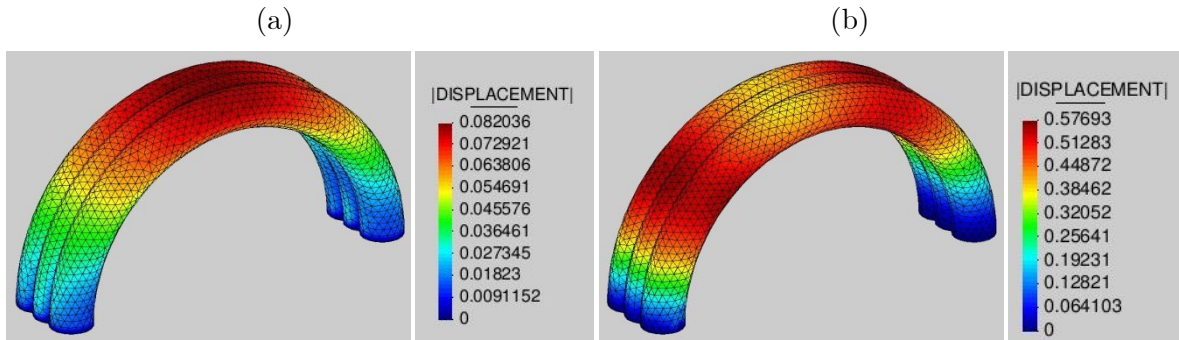


Figure 5.32. Displacements due to 1000Pa internal pressure (a) S-W and internal pressure (b) S-W, internal pressure and air pressure due to inlet velocity of 35m/s

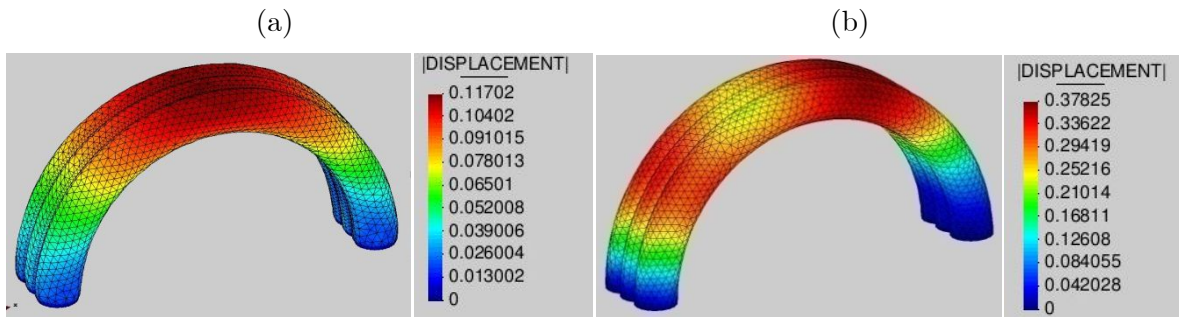


Figure 5.33. Displacements due to 2000Pa internal pressure (a) S-W and internal pressure (b) S-W, internal pressure and air pressure due to inlet velocity of 35m/s

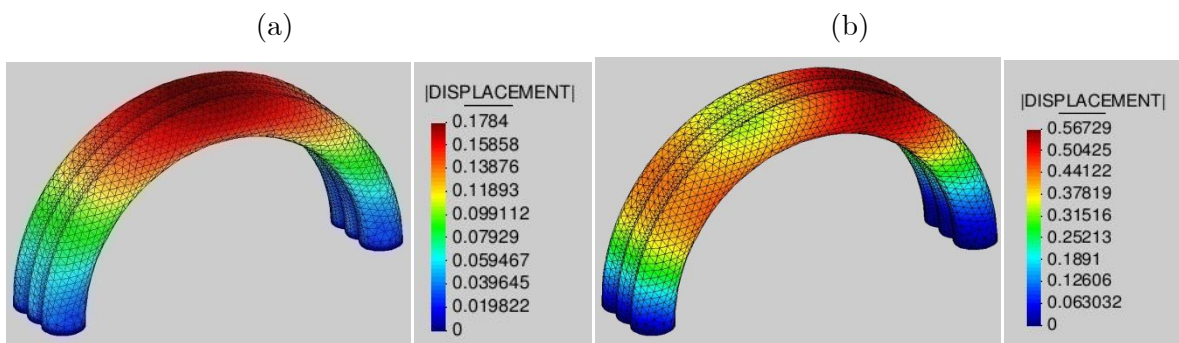


Figure 5.34 Displacements due to 3000Pa internal pressure (a) S-W and internal pressure (b) S-W, internal pressure and air pressure due to inlet velocity of 35m/s

One can observe that internal pressure has a great impact in the solution of the displacements occurred in an inflatable structure. Internal pressure provides stiffness to the structure. However, the displacements of the structure are not linear with the applied internal pressure. A low internal pressure (1000Pa) does not provide enough stiffness to the

structure and large displacements take place when wind loads act onto the structure. Also, for high pressures (3000Pa) large displacements appear. Internal pressure, at the top of the structure, acts in the same direction than the suction effect exerted by the wind load, thus the internal pressure at this area has an unfavourable component. It is worth noting that PLASTEL 8820 material is an elastic material and large initial displacements due to the high internal pressure can be noticed.

Nevertheless, internal pressure of 3000 strengthens the structure against the positive pressure at the front side of the upstream flow direction. Decrease of the relative displacement between initial displacements and final displacements can be observed.

Table 5-21. Displacement comparison due to different internal pressure (cm)

Internal pressure	S-W & internal pressure	S-W, internal pressure & Wind load
1000 (Pa)	8.2	57.7
2000 (Pa)	11.7	37.8
3000 (Pa)	17.8	56.7

Summary and Conclusions

The presented strong two-way coupling algorithm for fluid-structure interaction has been applied to simulate a real thin light-weight inflatable structure. The objective of the thesis has been the verification of the solution strategy and the application of the algorithm to a real case. First attempt of simulating light-weight structures in a virtual wind tunnel using a strongly coupled algorithm has been carried out in this thesis.

For obtaining a robust and efficient implementation of the solution strategy, several preliminary stages for the application of the two-way coupling must be defined. Immediate application of the two-way coupling leads to a divergent solution of the problem. Suitable algorithmic improvements have been implemented in Chapter 4. These include the uncoupled and weakly coupled stages, and the determination of their optimal duration. Also, an incremental air pressure application algorithm at the first steps of the coupling has been proposed and implemented.

The core of this work has been the application of a two-way coupling simulation of a thin light-weight structure exposed to wind pressures. Furthermore, conventional simplified methods have been used in order to compare the obtained results.

The structure subject of these simulations was the inflatable aircraft hangar “H20” of the Buildair Company, which has a span of 20m. Average structural displacements of 13, 20 and 37 cm for wind inlet velocities of 10, 20 and 35m/s respectively were observed. The application of the ALE method for such displacements would have led to strong mesh distortion and consequently to a divergent solution.

Low values of the inlet velocity lead to an almost steady solution, and similar results compared with the conventional simplified CFD model were obtained. Hence, two-way coupling in these cases is not obligatory. High inlet velocities lead to unsteady flows characterized by strong vortices. The unsteady flow generates oscillatory movements in the structure. Nevertheless, for the cases analyzed, the discrepancy between the displacements

observed for both methods, two-way coupling and the conventional simplified CFD, was considerably minor. Possibly, in order to observe considerable differences, finer mesh resolutions must be used. However, this would require excessive computational time, not feasible in the framework of this master thesis.

Maximum pressures of 481 and 780 Pa with amplitudes of 227 and 169 Pa were obtained for inlet velocities of 20 and 35m/s, respectively.

The oscillations in the motion and the pressure spectrum, in turn, affect the flow, such behaviour cannot be accounted for in a simplified weakly coupled models. Both the amplitude and the frequency of the forced oscillation have impacted upon the structural stability, and thus should be considered and compared with the eigen-frequency of the structure to identify dangerous resonance problems.

Solutions for reducing the displacements in the structure have been analyzed. Although internal pressure shows an unfavourable behaviour against maximum displacements at the top of the structure, it decreases the displacements produced at the lateral wall due to positive air pressure.

Nevertheless, the disposal of stiffening straps onto the structure has shown an excellent performance against displacements and stresses. Reductions of 14% in the solution with a wind inlet velocity of 35m/s were achieved. Also, lightening on the stresses of the main material of the structure was observed, since the straps absorb the stresses undergone by the exerted pressures and the consequent deformation. This reduction of stresses may increase the PLASTEL 88200 end-of-life.

Future works

Interesting results have been obtained at the first attempt of applying a strong two-way coupling to simulate a thin light-weight structure immersed in a virtual wind tunnel. Differences in the results and in the motion of the structure compared to the conventional methods used nowadays in the simulation of this kind of structure have been obtained. However, further studies must be carried out in order to observe considerable differences, and strengthen the use of a strong two-way coupling simulation in thin light-weight structures involving large displacements due to exerted wind pressures.

High wind velocities surrounding inflatable structures produce oscillatory movements to the structure. However, detailed analysis on the eigen frequency of the structure was not performed. The deep analysis of the interaction between the air frequency and the eigen frequency of the structure is a new and open line of research. The study of this topic would provide essential information to understand the motion of the structure due to wind pressures.

The addition of a cable element in the structural model would allow the modelling of straps with this new element, allowing the creation of uniform meshes in the structural model. Thereby, potential errors due to the membrane self-contact would be avoided.

List of Authors

- [1] T.E Tezduyar, "Computation of moving boundaries and interfaces and stabilization parameters," *International Journal for Numerical Methods in Fluids*, no. 43, pp. 555-575, 2003a.
- [2] T.E. Tezduyar, "Stabilized finite element formulations and interface-tracking and interface-capturing techniques for incompressible flows," *World Scientific*, vol. Numerical Simulations of Incompressible Flows, pp. 221–239.
- [3] C., van Brummelen, E.H., Hulshoff, S.J., and de Borst, R. Michler, "The relevance of conservation for stability and accuracy of numerical methods for fluid–structure interaction," *Computer Methods in Applied Mechanics and Engineering*, no. 192, pp. 4195-4215, 2003.
- [4] C., van Brummelen, E.H., Hulshoff, S.J., and de Borst, R. Michler, "A monolithic approach to fluid–structure interaction," *Computers & Fluids*, no. 33, pp. 836-848, 2004.
- [5] E.H. and de Borst, R. van Brummelen, "On the nonnormality of subiteration for a fluid-structure interaction problem," *SIAM Journal on Scientific Computing*, no. 27, pp. 599-621, 2005.
- [6] SR Idelsohn, F Del Pin, N Calvo E Oñate, "Fluid-structure interaction using the particle finite element method," *Computer Methods in Applied Mechanics and Engineering*, vol. 195, no. 17, pp. 2100-2123, 2006.
- [7] Mauro Porta, Riccardo Rossi, Thilo Schoenfeld Pavel ryzhakov, "On the FSI in combustion chambers," in *Thematic Conference on COupled Problems*, Santa Eulalia, Ibiza, Spain, 2007.
- [8] S.R., Marti, J., Limache, A., and Onate, E. Idelsohn, "Unified Lagrangian formulation

- for elastic solids and incompressible fluids fluids: Application to fluid–structure interaction problems via the PFEM," *Computer Methods in Applied Mechanics and Engineering*, no. 197, pp. 1762–1776, 2008a.
- [9] S.R., Marti, J., Souto-Iglesias, A., and Onate, E. Idelsohn, "Interaction between an elastic structure and free-surface flows: experimental versus numerical comparisons using," *Computational Mechanics*, no. 43, pp. 125-132, 2008b.
- [10] K., Brummer, T., Tezduyar, T.E., and Chen, P.R. Takizawa, "A comparative study based on patient-specific fluid–structure interaction modeling of cerebral aneurysms," *Journal of Applied Mechanics*, no. 79, p. 010908, 2012b.
- [11] Tao Tang, "Moving Mesh Methods for Computational Fluid Dynamics," *Contemporary Mathematics*, 1991.
- [12] Andrew A. Johnson, "Dynamic-Mesh CFD: Its application to flapping-wing micro-ai vehicles," in *25th Army Science Conference*, Minneapolis, Minnesota.
- [13] M. Ortiz R. Radovitzky, "Lagrangian finite element analysis of newtonian fluid flows," *International Journal for Numerical Methods in Engineering*, no. 43, pp. 607-619, 1998.
- [14] O. Ghattas I. Malcevici, "Dynamic-mesh finite element method for lagrangian computational fluid dynamics," *Finite Elements in Analysis and Design*, no. 38, pp. 965-982, 2002.
- [15] R. Glowinski, T.W. Pan, A.J. Kearsley, and J. Periaux, "Numerical simulation and optimal shape for viscous flow by a fictitious domain method," *International Journal for Numerical Methods in Fluids*, no. 20, pp. 695-711, 2005.
- [16] J. Mohd-Yosuf, *Combined immersed boundary/B-spline methods for simulation on complex geometries*, Center for turbulence research Annual Research Birefs, Ed., 1997.
- [17] J.H. Ferziger Y.H. Tseng, "A ghost-cell immersed boundary method for flow in complex geometry," *Journal of Computational Physics*, no. 192, pp. 593-623, 2003.
- [18] Wolfgang A. Wall Axel Gerstenberger, "An eXtended Finite Element Method/Lagrange

- multiplier based approach for fluid-structure interaction," *Computer methods in applied mechanics and engineering*, vol. 197, pp. 1699-1714, 2008.
- [19] van Krevald M., Overmars M., and Schwarzkopf O. de Berg M., "Computational Geometry Algorithms and applications," *Springer-Verlag*, 1997.
- [20] Yong J. H., Sun J. G., Gu H. J., and Paul J. C. Yang S., "A cell-based algorithm for evaluating directional distances in GIS," *International Journal of Geographical Information Science*, no. 24(4), pp. 577-590, 2010.
- [21] Baumgartner D. and Wolf J., "Interface treatment and solution procedures in fsi simulations using an ale or embedded strategy," *Master's thesis, Technical University of Munich, TUM*, 2013.
- [22] Lazzari M., Saetta A.V. Vitalini R.V., "Non-linear dynamic analysis of cable suspended structures subjected to wind actions," *Journal of Computer and Structures*, no. 79, pp. 233-251, 2001.
- [23] Riccardo Rossi, "Light-weight structures. Numerical Analysis and Coupling issues," Università di Bologna, PhD dissertation January, 2006.
- [24] Eugenio Oñate, Pere-Andreu Ubach Robert L. Taylor, "Textil Composites and Inflatable Structures," in *Textil Composites and Inflatable Structures.*: Springer, 2005, pp. 47-68.
- [25] P.B. Ryzhakov and A. Jarauta, "An embedded approach for immiscible multi-fluid problems," *Internal Journal for Numerical Methods in Fluids*, no. 00, pp. 1-33, 2015.
- [26] Waler Munk. (2014, July) https://en.wikipedia.org/wiki/Significant_wave_height.
- [27] R.L. Taylor y P. Nithiarasu O.C. Zienkiewicz, *El Método de los Elementos Finitos: Dinámica de fluidos*, Sexta edición ed., M. Cervera, E. Oñate G. Bugeda, Ed. Barcelona, España: CIMNE, 2005.
- [28] J.N. Reddy and D.K. Gartling, *The Finite Element Methods in Heat Transfer and Fluid Dynamics*, Second Edition ed. Florida, USA: CRC Press, 2000.

- [29] F.R.S. G.K. Batchelor, *An introduction to Fluid Dynamics*. Cambridge, United Kingdom: Cambridge University Press, 2000.